Hybrid Materials of Block Copolymers and Magnetic Nanoparticles

by

Zhihan Zhou

A thesis submitted to the Chemistry Department
in conformity with the requirements for the degree of
Doctor of Philosophy

Queen's University
Kingston, Ontario, Canada
September, 2010

Abstract

In this PhD thesis, the preparation of several types of hybrid materials of block copolymer and magnetic nanoparticles is described. The diversified morphologies of nanoaggregates formed by dispersing poly(glyceryl methacrylate)-*block*-poly(2-cinnamoyloxyethyl methacrylate)-*block*-poly(*tert*-butyl acrylate) tri-block copolymers in block selective solvents will be reported first. The volume occupied by the core block in these nanoaggregates can be swollen by solvent, and the core block can be sculpted. The cores can act potentially as the template to grow magnetic nanoparticles. Thus, a potential method for preparing hybrid magnetic materials of block copolymers and magnetic nanoparticles with different morphologies is developed.

A one-pot method to synthesize cobalt nanoparticles covered by a polymer shell is then reported. This is achieved by thermally decomposing dicobalt octacarbonyl in the presence of polymeric multi-dentate ligand poly(ethylene glycol)-*block*-poly(acrylic acid). Using a similar method, cobalt nanoparticles covered by poly(2-cinnamoyloxyethyl methacryate)-*block*-poly(acrylic acid) ligand are synthesized. The cobalt nanoparticles fuse into chains for their magnetic dipole-dipole interaction. The chains are then coated with poly(*tert*-butyl acrylate)-*block*-poly(2-cinnamoyloxyethyl methacrylate). The coated Co chains are further locked by photo-crosslinking the poly(2-cinnamoyloxyethyl methacrylate) segments. The as-prepared cobalt nano wires have interesting magnetic response and may be used to build complicated magnetic nano devices.

Another hybrid magnetic material is prepared via an oil-in-water emulsion method. The oil phase of the emulsion sphere consists of *r*-Fe_2O_3 magnetic nanoparticles covered with the poly(2-cinnamoyloxyethyl methacryate)-*block*-poly(acrylic acid) ligand and a poly(2-cinnamoyloxyethyl methacryate) homopolymer. It was dispersed in water using a mixture of poly(2-cinnamoyloxyethyl methacrylate)-*block*-poly(succinoylglyceryl methacrylate) and poly(2-cinnamoyloxyethyl methacrylate)-*block*-poly(glyceryl methacrylate) as the surfactants. The evaporation of the organic solvent left behind solid particles in water. The polymer chains on the surface of the obtained spheres allow the immobilization of biomolecules. Factors affecting the emulsion process are studied systematically. The emulsion spheres are characterized using TEM, AFM, TGA and etc. The emulsion sphere have potential application is immunoassay. The protein binding capacity of the spheres is determined.

Acknowledgment

First and foremost, I would like to sincerely thank Dr. Guojun Liu for offering me the opportunity to study in his lab for a PhD degree. This allowed me to transform my dream into reality. During the past few years, his inspiration and guidance were the important support for me to overcome the difficulties in the study. I sincerely wish I have become a good chemist as he expected.

Many thanks are given to the people in Dr. Liu's group. I cannot finish my study without their kind help and warm encouragement. Dr. Dehui Han and Dr. Liangzhi Hong provided me with high quality block copolymers. Dr. Xiaohu Yan, Dr. Jiwen Hu, and Dr. Kyoungmoon Koh helped to learn how to study the morphology of the nano structures. Dr. Nemesio, Dr. Ronghua Zheng, and Dr. Jiguang Zhang helped me to learn how to synthesize polymers. Dr. Gabriel Njikang, Dr. Hongjing Dou and Dr. Yu Fu gave me many important suggestions and encouragement when I encountered difficulties in research. I also express my appreciation to the students, Heng Hu, Nan Wang, John Dupont, Scott Curda, Qiliang Peng, Xiaoyu Li and Yang Gao, for their help. In the end by not the less, I thanks for Dr. Ian Wyman for proof reading this thesis.

I appreciate Ms. Jiandong Wang for doing the AFM study of my samples, Mr. Alan Grant for doing the XRD study of the cobalt and iron oxide nanoparticles, and Dr. Paul Dube for analyzing the magnetization curves of the cobalt nanoparticles and magnetic emulsion spheres.

The work in this thesis was supported financially through NSERC, XEROX, and the Chemistry Department of Queen's University.

Last, but certainly not least, I am sincerely appreciate for the love and support from my wife, Ying Jiang. I don't think I could have gone through this challenging time without you.

Statement of Originality

I hereby certify that all of the work described within this thesis is the original work of the author. Any published (or unpublished) ideas and/or techniques from the work of others are fully acknowledged in accordance with the standard referencing practices.

Table of Contents

List of Figures

List of Tables

List of Abbreviations

AFM	atomic force microscopy
ATRP	atom transfer radial polymerization
BCA	bicinchoninic acid
BSA	bovine serum albumin
$CDCl_3$	deuterated chloroform
MA	2-cinnamoyloxyethyl methacrylate
CH_2Cl_2	dichloromethane
$CHCl_3$	chloroform
CLD	crosslinking density
CMC	critical micellization concentration
$Co_2(CO)_8$	dicobalt octacarbonyl
COOH	carboxylic acid group
cryo-TEM	cryogenic transmission electron microscopy
DCB	1,2-dichlorobenzene
DLS	dynamic light scattering
DMF	*N*,*N*-dimethylforamide
DN	decahydronaphthalene
dn*/*dc	refractive index increment
EDCI	1-ethyl-3-(3-dimethylaminopropyl)carbodiimide
EDTA	ethylenediaminetetraacetic acid
emu	electromagnetic unit
$Fe(CO)_5$	iron pentacarbonyl
Fe_3O_4	magnetite
FID	free induction decay
FT-IR	Fourier transform infrared
γ–Fe_2O_3	maghemite
GPC	gel permeation chromatography
HCl	hydrochloric acid
hcp	hexagonal close-packed

^{1}H NMR	proton nuclear magnetic resonance
IR	infrared
kV	kilovolt
LS	light scattering
MeOH	methanol
M_n	number average molecular weight
M_w	weight average molecular weight
NHS	N-hydroxysuccinimide
NMP	nitroxide mediated polymerization
NMR	nuclear magnetic resonance
NPs	nano particles
O/W	oil-in-water emulsion
Oe	oersted
OsO_4	osmium tetraoxide
P(HEMA-TMS)	poly(trimethylsiloxyethyl methacrylate)
P2VP	poly(2-vinylpyridine)
P3HT	poly(3-hexylthiophenes)
P4VP	poly(4-vinylpyridine)
PAA	poly(acrylic acid)
PBS	Phosphate buffered saline
PCEMA	poly(2-cinnamoyloxyethyl methacrylate)
PDI or M_w/M_n	polydispersity index
PDMAEMA	poly(dimethylaminoethyl methacrylate)
PEG	poly(ethylene glycol)
PEO	poly(ethylene oxide)
PGMA	poly(glyceryl methacrylate)
PHEMA	poly(hydroxylethyl methacrylate)
PHS	poly(12-hydroxystearic acid)
PI	polyisoprene
PMDETA	N,N,N',N',N''-pentamethyldiethylenetriamine
PMMA	poly(methyl methacrylate)
PNIPAM	Poly(*N*-isopropylacrylamide)

PS	polystyrene
PSGMA	poly(succinoylglyceryl methacrylate)
PSMA	poly(solketal methacrylate)
P*t*BA	poly(*tert*-butyl acrylate)
RAFT	reversible addition-fragmentation chain transfer polymerization
RI	refractive index
RLU	relative light units
RuO_4	ruthenium tetraoxide
SEC	size exclusive chromatography
STD	standard deviation
***t*BA**	*tert*-butyl acrylate
TEM	transmission electron microscopy
TFA	trifluoroacetic acid
T_g	glass transition temperature
TGA	thermal gravimetry analysis
THF	tetrahydrofuran
TOPO	trioctylphosphine oxide
UV-vis	ultra-violet visible spectrum
W/O	water-in-oil emulsion
XRD	X-ray diffraction

Chapter 1

Introduction

This thesis is consisted of the research on hybrid materials of block copolymer and magnetic nanoparticles. The research includes the study and modification of poly(glyceryl methacrylate)-*block*-poly(2-cinnamoyloxyethyl methacrylate)-*block*-poly(*tert*-butyl acrylate) (PGMA-*b*-PCEMA-*b*-P*t*BA) triblock copolymer nano-aggregates in block selective solvent; the preparation of magnetic nanocrystals in the presence of poly(ethylene glycol)-*b*-poly(acrylic acid) (PEG-*b*-PAA) or poly(2-cinnamoyloxyethyl methacryate)-*block*-poly(acrylic acid) (PCEMA-*b*-PAA) polymer surfactants; the structure locking of the assembly of magnetic cobalt nanoparticles in the presence of poly(*tert*-butyl acrylate)-block-poly(2-cinnamoyloxyethyl methacrylate) (P*t*BA-*b*-PCEMA); and the preparation of emulsion spheres containing magnetic nanoparticles and chains-segregated surfaces using poly(2-cinnamoyloxyethyl methacrylate)-*block*-poly(succinoylglyceryl methacrylate) (PCEMA-*b*-PSGMA) and poly(2-cinnamoyloxyethyl methacrylate)-*block*-poly(glyceryl methacrylate) (PCEMA-*b*-PGMA) as surfactants. The hybrid materials developed in this thesis retaining ordered structure and magnetic response; therefore they have potential applications such as building ordered magnetic tunable devices and being used in clinical diagnostics. The structures of the polymers that were used in this thesis are shown in Figure 1.1.

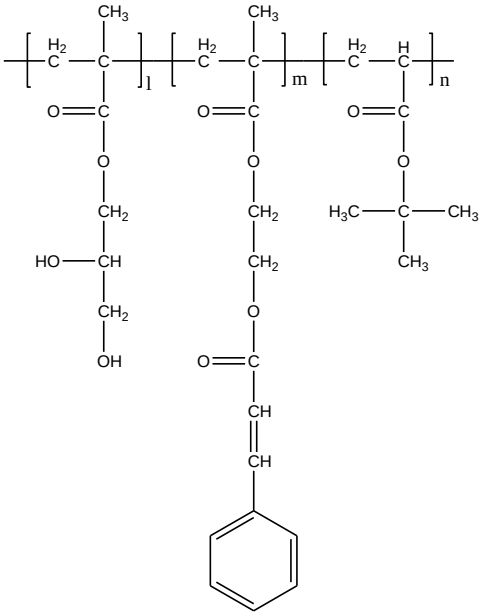

poly(glyceryl methacrylate)-*block*-poly(2-cinnamoyloxyethyl methacrylate)-*block*-poly(*tert*-butyl acrylate)
(PGMA-*b*-PCEMA-*b*-P*t*BA)

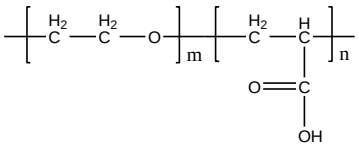

poly(ethylene glycol)-*b*-poly(acrylic acid)
(PEG-*b*-PAA)

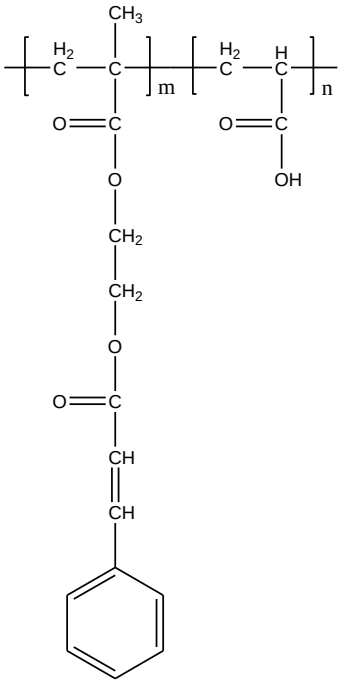

poly(2-cinnamoyloxyethyl methacryate)-*block*-poly(acrylic acid)
(PCEMA-*b*-PAA)

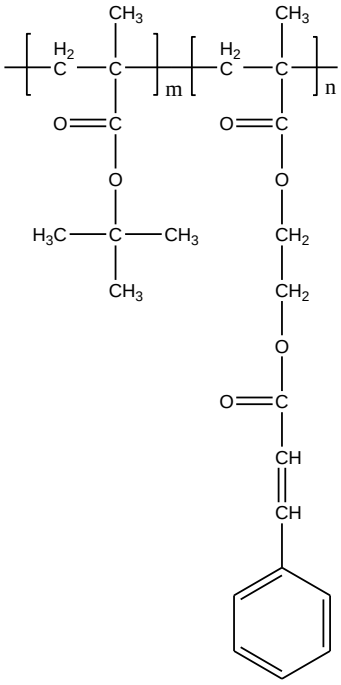

poly(*tert*-butyl acrylate)-block-poly(2-cinnamoyloxyethyl methacrylate)
(P*t*BA-*b*-PCEMA)

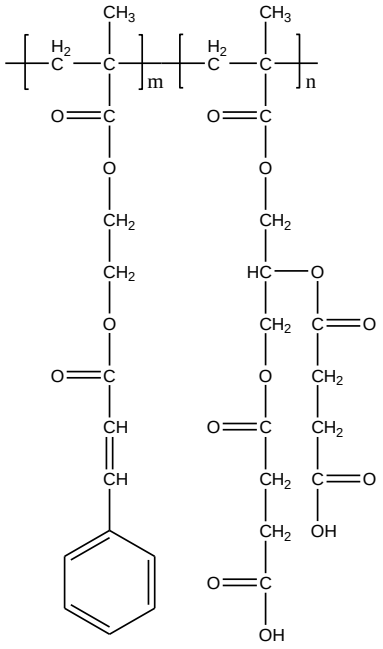

poly(2-cinnamoyloxyethyl methacrylate)-*block*-poly(succinoylglyceryl methacrylate) (PCEMA-*b*-PSGMA)

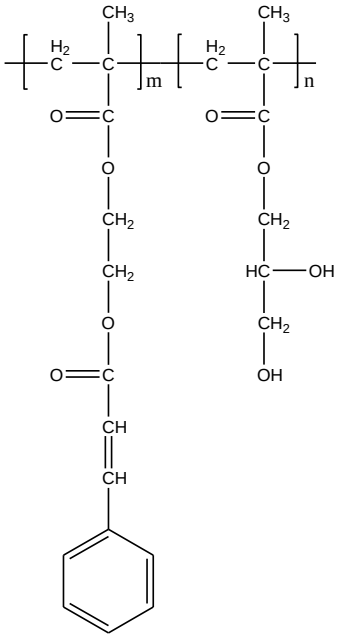

poly(2-cinnamoyloxyethyl methacrylate)-*block*-poly(glyceryl methacrylate) (PCEMA-*b*-PGMA)

Figure 1.1. Structures of block copolymers that were used in this thesis.

Block copolymers refer to a class of polymers which are formed by covalently connecting at least two polymer segments or blocks containing homogeneous repeating units.[1] Block copolymers can be classified as diblock, triblock, tetrablock, pentablock and multi-block according to the number of blocks. They can also be classified according to the way that the blocks are connected to each other such as linear, branched for example. The systematic understanding of the nature and application of block copolymers has been made possible in the past few decades due to the development of controlled polymerization techniques, such as anionic polymerization and controlled free radical polymerization.

The most interesting property of block copolymers is the micro-phase segregation behaviour that occurs between the blocks. As a consequence, block copolymers can self-assemble into versatile nanometer scaled morphologies, either in the solid state, or in block selective solvents. Furthermore, self-assembled block copolymers can be used as building blocks for more complicated structures by chemically connecting or physically assembling them into hierarchical assemblies. These self-assembled patterns of block copolymers can also be modified or sculptured to introduce other physical and chemical properties. Self-assembled block copolymers are used in a variety of applications including drug delivery,[2] lithography,[3] nanofabrication[4] and other applications.

Block copolymers are uniquely suited as surfactants for the preparation of colloidal particles. Nanometer-sized inorganic crystals can be stabilized by block copolymer surfactants. While one block segment preferentially adsorbs onto the surface of the crystal, another block interacts with the solvent. Similarly, block copolymer surfactants can stabilize droplets in either water-in-oil or oil-in-water emulsions. Using block copolymers with versatile functional groups could introduce further physical and chemical properties of nanocrystals and emulsion droplets.

This section will review block copolymer self-assembly, the hybrid materials formed by block copolymers and nanometer scale inorganic crystals, and the use of block copolymers as surfactants used when preparing emulsions. At the end the section, the research focus of this thesis will be addressed.

1.1 Block copolymer self-assembly

1.1.1 Self-assembly of block copolymers in the bulk state

The segregation between polymer chains is explained by considering the free energy of mixing. The mixing free energy of two different molecules is given by:

$$\Delta G_{mix} = \Delta H_{mix} - T\Delta S_{mix} \tag{1.1}$$

and

$$\Delta S_{mix} = -k_B \left(N_1 \ln x_1 + N_2 \ln x_2 \right) \tag{1.2}$$

where k_B is the Boltzmann constant, N is the number of the corresponding molecules, and x is the mole fraction of the corresponding molecules. By combining equations (1.1) and (1.2), ΔG_{mix} becomes:

$$\Delta G_{mix} = \Delta H_{mix} + k_B T \left(N_1 \ln x_1 + N_2 \ln x_2 \right) \tag{1.3}$$

However, since a polymer is made of covalently connected repeating units, the mixing free energy of two polymer chains becomes:

$$\Delta G_{mix} = \Delta H_{mix} + k_B T \left(\frac{N_1}{n_1} \ln \varphi_1 + \frac{N_2}{n_2} \ln \varphi_2 \right) \tag{1.4}$$

where n is the number of repeating units, and φ is the volume fraction. Therefore, the entropy for mixing two dissimilar polymers is much less than the mixing entropy of small molecules. For example, in the bulk state, a larger contribution to the mixing free energy

of dissimilar polymer chains comes from the enthalpy, which is usually positive; unless the chains have specific interactions such as ion pairing or H-bonding. Under such conditions, the dissimilar polymer chains tend to become segregated from each other. For block copolymers in the bulk state, microphase separation is driven by thermodynamic incompatibility, while the macrophase separation is prevented by the covalent bonds holding the different blocks together.[5] Generally, the morphology of diblock copolymers in the bulk state is governed by the number of repeating units, the volume fraction of the different blocks, and the Flory-Huggins parameter, χ, which describes the enthalpy of contacting polymer chains. Bates *et al.* discussed the possible morphologies of linear AB di-block copolymers in the bulk state, where A and B represent incompatible blocks.[5] Based on self-consistent theory, four equilibrium phases were predicted in the phase diagram (Figure 1.2). For a fixed χ_N value, the morphological transition of an AB di-block copolymer is governed by the volume fraction (f) of the blocks. As the volume fraction of block A (f_A) increases, the morphology varies from spheres, cylinders, gyroids, and lamellae. A phase diagram of a diblock copolymer, polyisoprene-*b*-polystyrene or PI-*b*-PS, was plotted by Khandpur *et al.*[6] The diagram resembles the theoretical plot. Numerical calculations could be applied to predict the possible morphologies of multi-block copolymers,[7] however, this is beyond the scope of the discussion in this section.

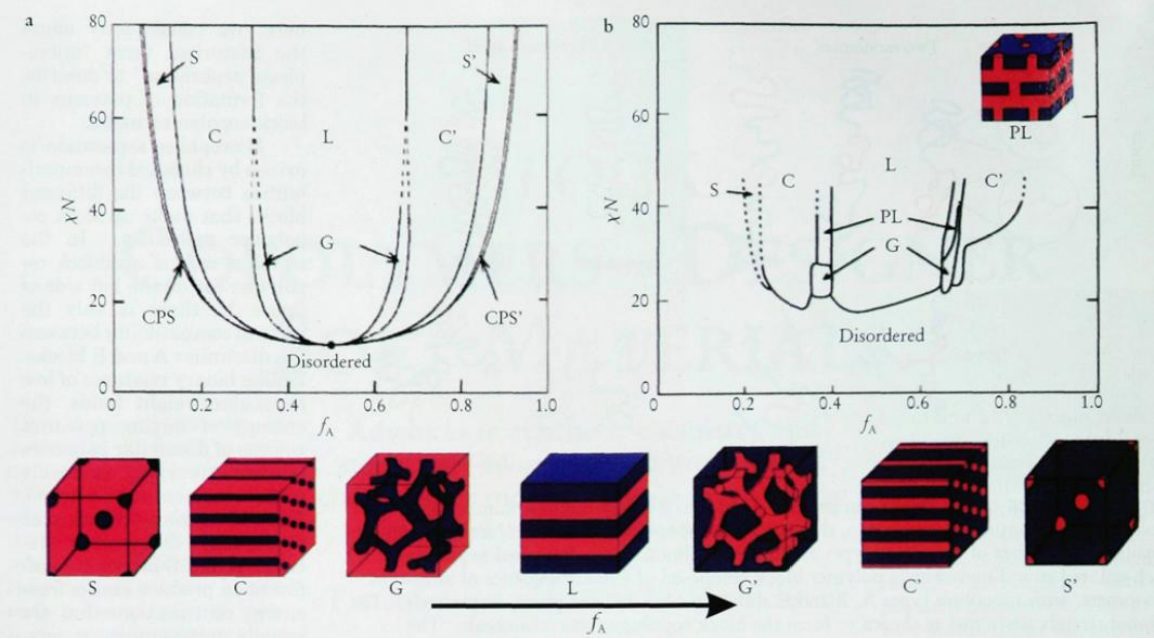

Figure 1.2. Phase diagram of the self-assembly of an AB diblock copolymer.[6] (a) Equilibrium morphologies predicted by self-consistent mean field theory: spherical (S), cylindrical (C), gyroid (G), and lamellar (L); (b) experimental result obtained with PS-*b*-PI.

1.1.2 Block copolymer self-assembly in block selective solvents

For a block copolymer, a block selective solvent is defined as a solvent which dissolves at least one block (hereafter called a "good" solvent) and which causes the other blocks to precipitate (hereafter called a "poor" solvent). Suppose that a linear AB diblock copolymer, in which the block length of the A block is much greater than that of the B block, is placed in a block selective solvent, which is a good solvent for block A and a poor solvent for the B block. In order to decrease the total free energy of the system, the A blocks tend to stretch into the solvent and the B blocks tend to segregate against the solvent in order to minimize the energetically unfavored interaction between the B blocks and the solvent. The B blocks therefore form a core phase while the A blocks form a

corona or shell, resulting in the formation of spherical polymer aggregates. If this morphology is known to be thermodynamically stable, they are called spherical micelles. If the stability origin is unknown, they are called micelle-like aggregates.

Generally, block copolymers may self-assemble into micelles or aggregates in block selective solvents if the concentration of the copolymer is higher than a critical value, known as the critical micellization concentration or CMC.[8] In practice, block copolymer self-assemblies are usually prepared following two protocols. In the first technique, the block copolymer is dissolved in a solvent which is good for all of the blocks. Then, a block selective solvent is added gradually with vigorous stirring until micellization occurs.[9] In the second technique, the block copolymer is dispersed directly in a block selective solvent.[9] During the preparation of the block copolymer micelles or micelle-like aggregates using the above mentioned techniques, the mobility of the polymer chains might be frozen at a certain solvent composition, resulting in products that are not necessarily thermodynamically stable. The existence of kinetic products contributes to the abundance of morphologies observed in self-assemblies.

The morphological transition of diblock copolymer self-assemblies in aqueous dispersions associated with the variation in thevolume fraction of a block was first reported by Eisenberg and coworkers.[10] By increasing the volume fraction of polystyrene or PS in a polystyrene-*b*-poly(acrylic acid) or PS-*b*-PAA diblock copolymer, the morphologies of the micelles changed from spheres to cylinders to vesicles and to large-

compound spheres (Figure 1.3). This morphological transition is similar to that of the diblock copolymer in the bulk state. In order to better understand the morphological transition and the driving force behind block copolymer self-assemblies, the free energy of the whole system is considered. For example, for a spherical micelle formed from PS-*b*-PAA, if the PAA block length becomes shorter, while the length of the PS block remains the same, the surface area required to accommodate each PAA chain decreases. This leads the core of the PS core to increase in size. A consequence of this is the stretching of the PS blocks. The entropy therefore decreases. If this entropic penalty is overcome by the benefit of the surface free energy (a reduction in the specific surface area of the spherical micelles), the morphology of the micelle remains spherical. However, if the entropic penalty cannot be balanced by a decrease in surface free energy, the morphology of the micelle changes to that of a cylinder. Figure 1.4 is a morphology diagram associated with free energy change.[11] A similar morphological transition of AB block copolymers in the aqueous phase resulting from hydrophilic block volume fraction variation is also observed for triblock copolymers. By increasing the volume fraction of the core forming block, Lei *et al.* reported a morphological transition of poly(styrene)-*b*-poly(2-vinylpyridine)-*b*-poly(ethylene oxide) or PS-*b*-P2VP-*b*-PEO from spheres to rods in a DMF/benzene solvent mixture.[12]

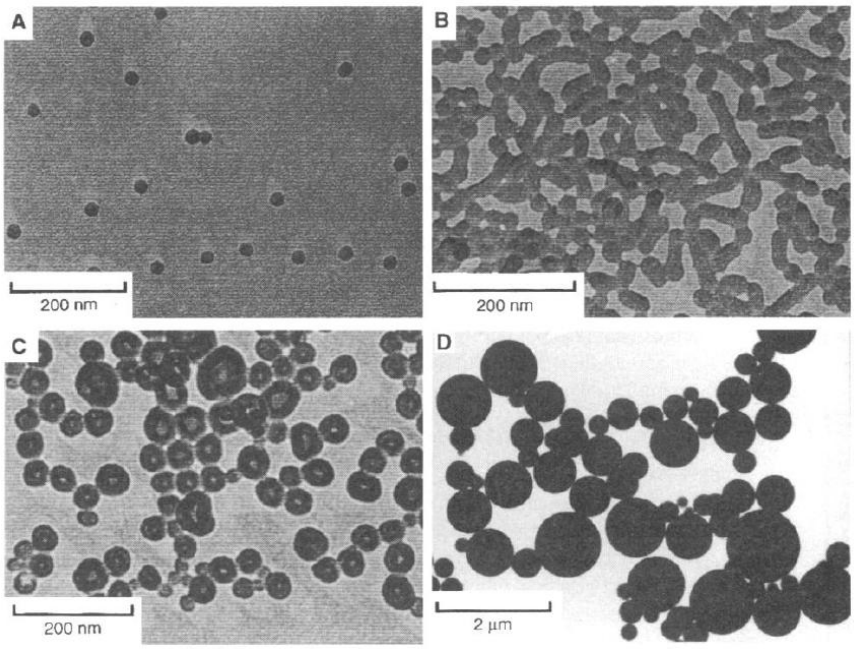

Figure 1.3. Crew-cut nano aggregates formed by PS-*b*-PAA diblock copolymers in water. (a) PS_{200}-*b*-PAA_{20}, (b) PS_{200}-*b*-PAA_{15}, (c) PS_{200}-*b*-PAA_{8}, and (d) PS_{200}-*b*-PAA_{4}.[10]

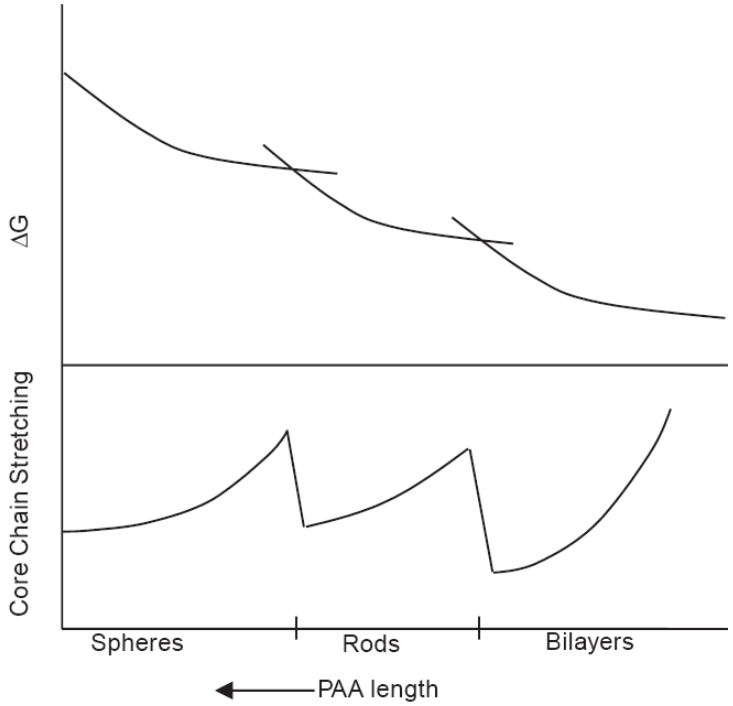

Figure 1.4. Diagram of the free energy change associated with changes in the composition of the PS-*b*-PAA diblock copolymer used in Figure 1.3.[11] (Cylindrical micelles can be called rods, while vesicles are bilayers.)

In addition to volume fraction, solvent composition is also an important parameter that can affect the morphology of block copolymer self-assemblies. An example of the effect of solvent composition on the morphology of diblock copolymer self-assembly is reported by Zhang *et al*.[13] By changing the volume ratio between water and acetone, the self-assembly of polystyrene-*b*-poly(acrylic acid-co-methyl acrylate) undergoes a morphology transition from core-shell spheres, to porous spheres, and finally to core-shell cauliflower-like aggregates.

Other parameters that can affect the morphology of block copolymers include pH and ionic strength. Eisenberg and coworkers,[11] for example, were able to tune the morphology of PS-*b*-PAA copolymers in water from spheres, to rods, to vesicles, and finally to large-compound-vesicles, by adding different amounts of acid (i.e. HCl). The ionic strength affects polymer aggregates by screening the effect of electrostatic repulsion, so that a morphology transition from spheres to vesicles is observed.

1.1.3 Other complicated self-assemblies of block copolymers

To achieve a preferred microdomain orientation or to induce a highly ordered macrodomain, the self-assembly of a block copolymer can be assisted by other external parameters such as changing the mechanical shear,[14] the solvent flow,[15] or applying an electric field[16] or a 2-D or 3-D confinement.[17] The resulting assemblies are called

directed assemblies. In some other examples, the self-assemblies of block copolymers can be sculptured to expose functional groups.[18] These functional groups allow for coupling reactions between different self-assemblies.

Sculpturing of the self-assemblies has proven useful for converting block copolymers into templates to incorporate inorganic crystals. The addition of inorganic crystals into block copolymer assemblies introduces other interesting properties, such as unique optical properties[19] or magnetic properties.[20] Since block copolymer self-assemblies are in the nanometer to micrometer scale, any incorporated inorganic crystals must be in the nanometer scale, or they should be nanoparticles. For example, Liu and coworkers reported the hydrolysis of P*t*BA chains, located in the confined space of an emulsion core, into PAA chains.[21] The exposed PAA units were used to grow a Pd catalyst nanoparticle. Another example of sculpturing P*t*BA chains of block copolymer self-assemblies is through the modification of core/shell cylinders formed by PS-*b*-PCEMA-*b*-P*t*BA block copolymer in bulk.[22] The PCEMA shell cylinders were then crosslinked. The crosslinked cylindrical domains were then levitated from the solid state via the solubilisation of the PS chains by THF to yield isolated nanofibers. After the P*t*BA chains in the core of the cylinders were hydrolyzed into PAA, Fe_2O_3 nanoparticles were grown in the cylinders with the assistance of the PAA chains.

1.2 Synthesis of magnetic nanoparticles covered by polymer ligands

At the end of the last section, the incorporation of inorganic crystals within the self-assembly of block copolymers was mentioned. One type of inorganic nanocrystals, which are of great interest, is magnetic nanocrystals. The incorporation of magnetic nanoparticles into block copolymer self-assemblies would allow the resulting structures to respond to magnetic fields. In this way, the block copolymer self-assembly can be used to build magnetically stimulated devices. Nanoparticles covered with polymer ligands are required to provide compatibility between the nanoparticles and block copolymers.

1.2.1 Formation theories of nanometer scaled inorganic crystals

Magnetic inorganic materials include metals (such as cobalt, nickel, and iron), metal oxides (such as cobalt oxide and iron oxide), and metal alloys (such as FePt, CoPt). The theory of the formation of nanometer scaled magnetic particles follows the general theories of the formation of inorganic nanocrystals. The first study of the formation mechanism of inorganic crystals was reported by LaMer in the 1950s.[23] Generally, nanocrystals are formed by active atomic or molecular species (also called monomers), which are produced by chemically treating their precursors. The formation of nanocrystals involves two steps: nucleation and growth. Nucleation occurs normally in the presence of a surfactant when the concentration of the monomer is supersaturated in a

solvent. As the nucleation proceeds, the nuclei start to grow by incorporating the dispersed monomers in the solvent and the concentration of the monomer in the solvent decreases. As the concentration of the monomer decreases, even though the monomer concentration is still above the saturated level, no more new nuclei will form. However, the growth of the existing nuclei continues until the concentration of the monomer reaches the saturation level. This concentration related mechanism is shown in Figure 1.5. The process of nanoparticle formation is shown in Figure 1.6. In order to produce nanoparticles with narrow mono size distribution, the nucleation step should be sufficiently separated from the growth step. [24] Moreover, the growth of the nuclei should all start at the same time, so that the growth rate and growth time of each nuclei are the same. In practice, a fast nucleation and a slower growth process is favored.

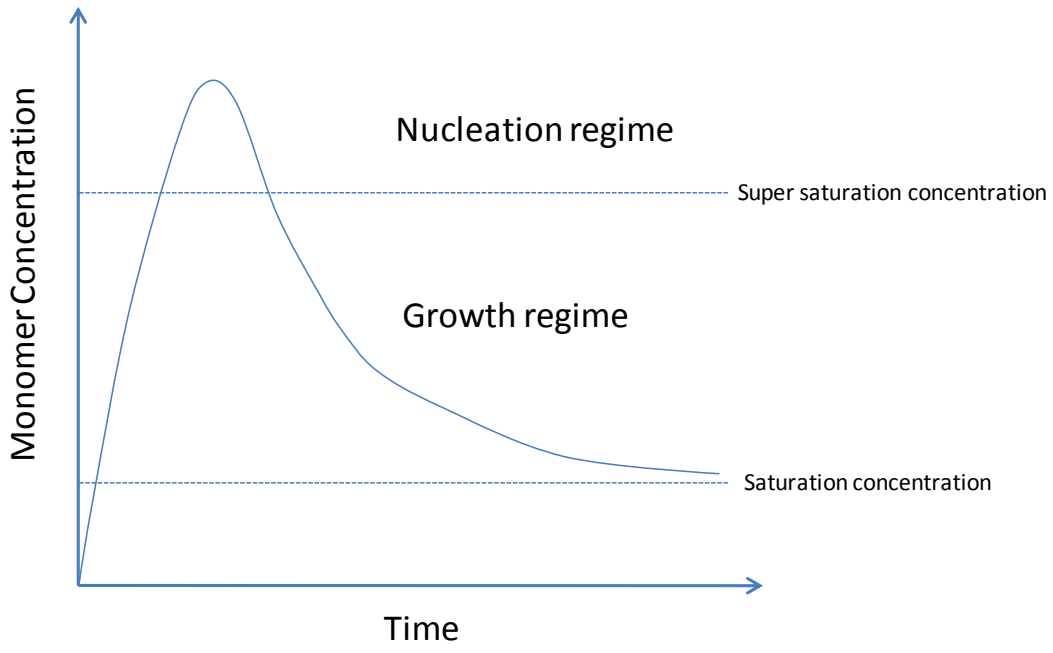

Figure 1.5. The nucleation and growth of nanoparticles as the monomer concentration changes following the LaMer mechanism.

The formation of a nanocrystal normally requires a thermal annealing process, where the atoms which form the crystals are able to rearrange during the growth process. It has been reported that the melting temperature of the crystals in the nanometer scale would be much lower than that of the bulk state.[25] Therefore, the growth of nanoparticles is possible at temperatures of 200 °C to 400 °C.

Kinetically, the growth rate of nuclei is related to the size of the nuclei and the monomer concentration.[26] As illustrated in Figure 1.6, below a critical diameter the nanocrystals shrink (left directing arrows), rather than grow; while above this critical point, the crystals grow (right directing arrows). There is also a peak diameter. Particles with such a diameter grow at the maximum rate. This peak diameter is also related to the monomer concentration. If the monomer concentration is low, the critical point will correspond with a larger diameter value. If this critical diameter is large enough to fall within the distribution of the diameter of the existing nanoparticles, some nanoparticles with diameters smaller than the critical diameter will shrink, leading to a broader size distribution. However, if the monomer concentration is sufficiently high during the growth process and the critical point is much less than the nanoparticle's diameter distribution, all of the nanoparticles will grow. As the size of the nanoparticles increase, the growth rate becomes slower. Over a period of time, particles that were initially smaller 'catch up' in size to those particles that were initially larger in diameters. The end result is a narrow size distribution. As shown in Figure 1.6, the diameters of the particles having the peak growth rate are smaller when the concentration of the monomer

is higher. The regime to the right of the peak growth rate diameter is called the size focusing regime.[27]

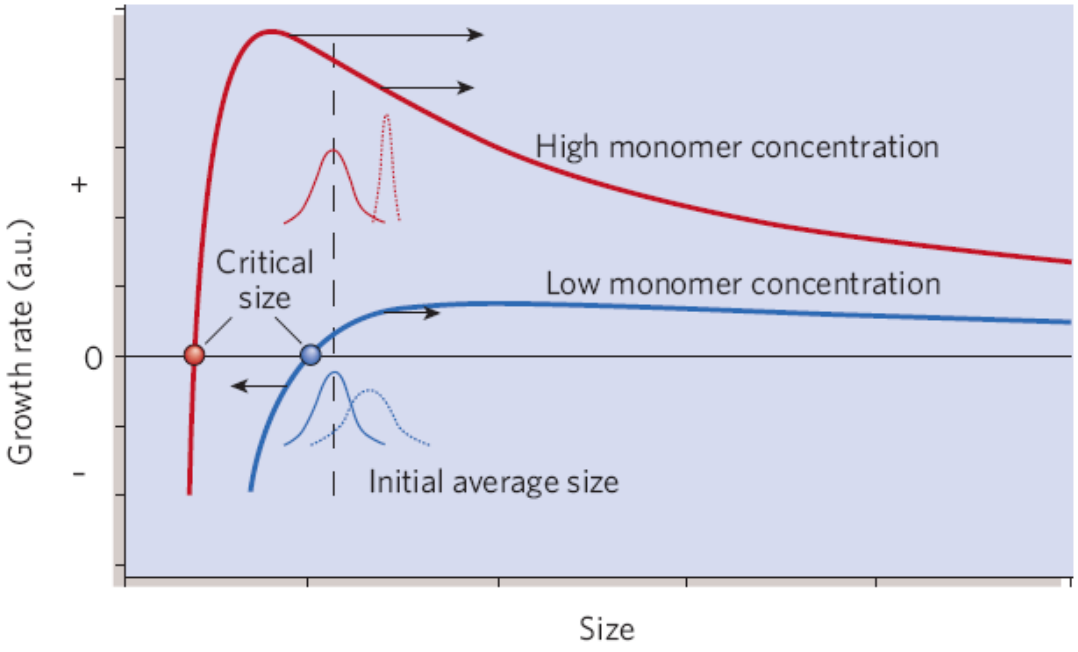

Figure 1.6. The kinetic diagram of the growth of nanoparticles associated with the size of the nanoparticles.[27]

The use of surfactants is important during the formation of nanoparticles. They cover the surface of the nanoparticles, and reduce the surface tension between the particles and the solvent. During the nucleation step, sometimes surfactants also form complexes with the monomer. Most importantly, the adhesion of a surfactant onto the surface of a nanocrystal dramatically affects the growth of the nanoparticles (Figure 1.7).[28] A desirable surfactant should bind to a particle reversibly and be able to undergo attachment and detachment during the growth of the nanoparticles. When a surfactant detaches, the

nanoparticles become accessible to monomers in solution. While attached, surfactants prevent the aggregation of the nanoparticles. Furthermore, surfactants can be used to adjust the shape of the nanocrystals by attaching to a specific surface preferentially, thereby slowing the growth rate at that point.[29] The synthesis of narrow size distributed inorganic nanocrystals was first studied with CdSe quantum dots, where a narrow size distribution is critical for their functionality.[30] Surfactants containing carboxylic groups (oleic acid), amine groups and phosphorous (TOPO)[24] were developed. Using these surfactants, narrow size distributed CdSe crystals were produced. As demonstrated by Puntes *et al.*, these surfactants could be used to prepare cobalt nanoparticles with controlled sizes and shapes.[24,31]

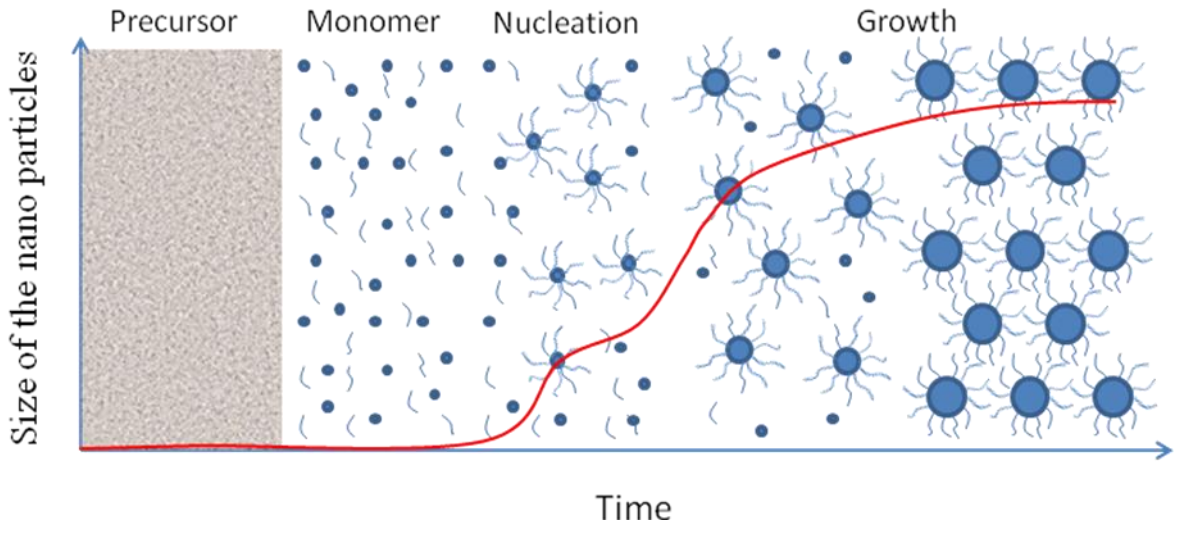

Figure 1.7. The process of the formation of nanoparticles in the presence of a surfactant.

1.2.2 Synthesis of monodispese cobalt and iron oxide magnetic nanoparticles

The synthesis of magnetic nanoparticles other than cobalt and iron oxide was reviewed in detail by Jeong *et al.*[32] Cobalt nanoparticles display strong magnetic properties, bearing a high saturation magnetization in the bulk state. The high magnetization of cobalt particles allow them to assemble into dipolar structures.[33] The size, shape and crystalline control of cobalt nanoparticles were extensively studied, borrowing the strategies learned from the synthesis of CdSe quantum dots.[31] The saturation magnetization of bulk iron oxide nanoparticles is lower than that of cobalt nanoparticles. However, since they are composed of metal oxide, the resulting nanoparticles are often more stable against oxidation.[32]

Generally, two methods are followed when synthesizing cobalt nanoparticles. In the first method, the cobalt nanoparticles are formed by reducing a cobalt salt in the presence of a surfactant.[34] For example, cobalt chloride (the precursor) is reduced to the ε-phase Co or ε-Co, by the addition of LiBEt3H when the salt is heated to 200 °C in a solvent. If the precursor is heated to a higher temperature (such as 300 °C) hexagonal close packed (hcp) Co nanoparticles are obtained. Hcp cobalt nanocrystals were also prepared by reducing cobalt acetate with 1,2-dodecanediol in the presence of oleic acid, or TOP, at 250 °C.[35] Although hcp Co is the most stable form of cobalt in the bulk state, ε-Co is the most common crystal state found in nanoparticles. Cobalt particles prepared by the reduction recipe always exhibit a multiple-twinned crystal structure, in which the crystal lattices are

alternatively oriented.[24] Furthermore, these crystals can be possibly contaminated by the reducing reagents.

The other method used to prepare cobalt nanoparticles involves the hot-injection of dicobalt octacarbonyl, or $Co_2(CO)_8$, in the presence of a surfactant.[31,35] This hot injection recipe was developed from the synthesis of CdSe crystals. Cobalt monomers are generated after the $Co_2(CO)_8$ precursor is injected rapidly into a solvent that was preheated above its decomposition temperature (such as 180 °C). Puntes *et al.* prepared monodisperse ε-Co particles *via* this thermal decomposition recipe using oleic acid, lauric acid, or TOP as a surfactant.[24,31] The size of the cobalt particles could be tuned by changing the monomer to surfactant ratio and the annealing temperature. Rapidly injecting $Co_2(CO)_8$ into a hot solvent was believed to induce homogeneous nucleation.[36] The decomposition of $Co_2(CO)_8$ into cobalt monomers occured immediately as the precursor was injected into the hot solvent, leading to a super saturation concentration of the monomer. The formation of nuclei should happen rapidly upon the formation of monomers. When using the two surfactants oleic acid and TOPO, rod shape cobalt crystals were prepared.[24]

There are several types of magnetic iron oxide nanoparticles that are of great interest. Fe_3O_4 nanoparticles are stable in air. Fe_3O_4 has a saturation magnetization of 92 emu/g and is used in the preparation of magnetic devices.[37] Another type of magnetic iron oxide which is stable in air is maghemite (γ-Fe_2O_3), which has a saturation magnetization of 74

emu/g.[38] Maghemite is very stable in air. The crystalline structure of maghemite is a defect spinel structure while magnetite is an inverse spinel structure.[32] The XRD patterns of these two types of nanoparticles are very similar. Due to the line broadening and the crystal shape effect, the XRD pattern is sometimes insufficient to distinguish between these two types of nanoparticles. Wustite is a type of paramagnetic material composed of Fe and FeO. Normally, it is represented as Fe_xO, where x ranges from 0.84 to 0.95.[39] The saturation magnetization of wustite is much lower than that of magnetite and maghemite. Wustite nanoparticles can be oxidized into maghemite or magnetite by introducing an oxidization reagent. Wustite nanoparticles are less desirable due to their low magnetization.

The preparation of magnetite or Fe_3O_4 is widely reported in the literature. Generally, the preparation involves one of two methods. The first method is to precipitate Fe^{3+} and Fe^{2+} with a ratio of 2.0:1.0 by the addition of bases, such as NaOH or NH_4OH, in the presence of a surfactant.[40] The Fe_3O_4 nanoparticles obtained from this precipitation recipe normally display a broad size distribution, and an additional size selective step is required to prepare monodisperse particles. Moreover, the size of the nanoparticles is not well controlled. Hyeon *et al.* reported a one-pot synthesis to prepare monodisperse Fe_3O_4 nanoparticles *via* the thermal decomposition of $Fe(Oleate)_3$ complexes (Figure 1.8).[41] For this method, a constantly increasing temperature is required. The nucleation began when the temperature of the reaction mixture was above 200 °C, where the first oleate ligand dissociated from the Fe(III) ion. However, the sudden growth of the nuclei was only possible when the temperature of the reaction mixture was above 280 °C, when the other

two oleate ligands were removed. The Fe_3O_4 nanoparticles were formed after being annealed near 300 °C. The nanoparticles obtained from this method are uniform in size. However, the magnetization of the particles (30 - 40 emu/g) was lower than that of the bulk state of magnetite.[42,43] Similarly, by thermally decomposing $Fe(acac)_3$ in the presence of a surfactant, Jana *et al.* reported the preparation of Fe_3O_4 nanoparticles.[44] In the presence of oleic acid, thermally decomposing this precursor generates Fe_3O_4 nano cubes, due to the fast growing of the <111> face.

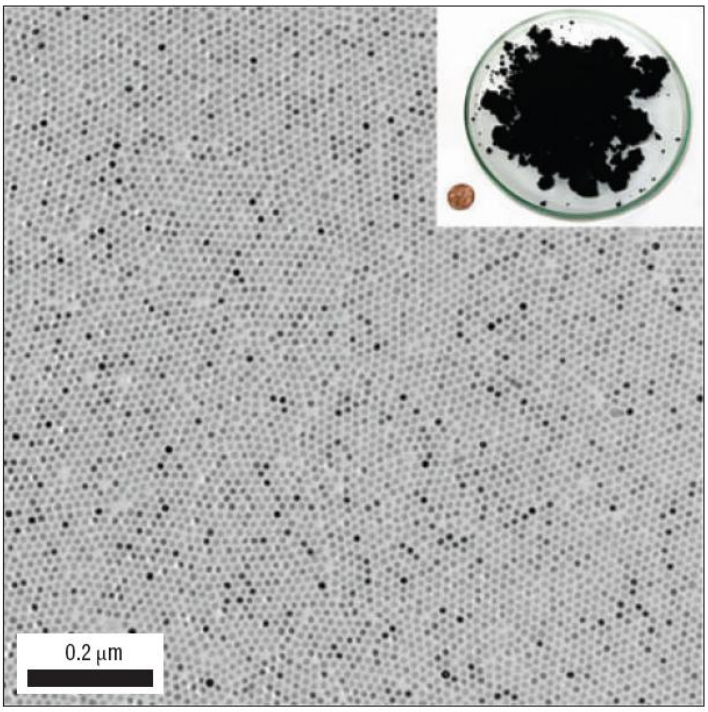

Figure 1.8. TEM image of monodisperse Fe_3O_4 nanoparticles formed by thermally decomposing $Fe(Oleate)_3$ complexes.

Maghemite is normally synthesized by a two step method. In the first step, Fe nanoparticles are formed by thermally decomposing iron pentacarbonyl, or $Fe(CO)_5$, in the presence of a surfactant. These Fe nanoparticles are then oxidized into γ-Fe_2O_3 in the

presence of oxidization reagents, such as trimethyl amine oxide or air.[45] Surfactants such as oleic acid, stearic acid or dodecylamine have been used.[46,47]

1.2.3 Synthesis of cobalt and iron oxide nanoparticles covered by polymeric surfactants

Compared to small molecule surfactants, polymeric surfactants are more effective at preventing the aggregation of magnetic particles. Polymeric surfactants also allow the particles to obtain higher degrees of functionality by incorporating numerous functional groups onto the polymer backbone. Moreover, since polymer chains are not compatible with either small molecule surfactants or other polymer chains, the selective covering of magnetic particles with desired polymer chains allows these magnetic particles to form hybrid materials with block copolymer assemblies. This section will discuss the coating of cobalt and iron oxide nanoparticles with polymeric surfactants.

For magnetic particles covered by small molecules, a direct method to replace the small molecules with polymer surfactants is by a ligand exchange process. As shown in Figure 1.9, the ligand exchange process involves a competing reaction where a second ligand that binds strongly onto the nanoparticle surface is used to replace the weakly bound ligand.[48] In order to improve the ligand exchange efficiency, the second ligand should have a high concentration. After the exchange process, free ligands are removed by precipitation, dialysis or other methods. One example of this ligand exchange procedure was reported by Xie and coworkers.[49] Fe_3O_4 nanoparticles stabilized by oleic acid and

oleylamine were mixed with poly(ethylene oxide) (PEO) with a terminal modified by dopamine. The small molecule surfactants were replaced by the PEO surfactant. Ligand exchange is a versatile recipe which allows a wide range of functionalized polymers to be introduced onto the nanoparticles' surfaces. However, the major drawback of this method is the amount of polymer required.

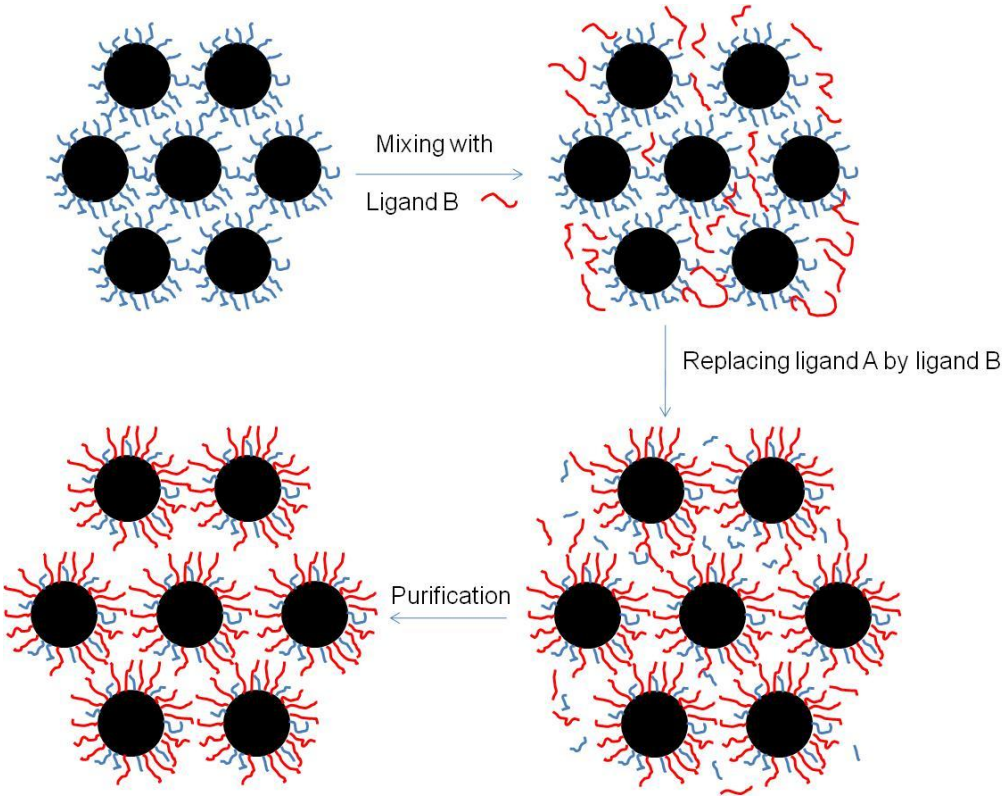

Figure 1.9. Ligand exchange of ligand A (blue) with ligand B (red).

Another method to introduce polymer ligands onto nanoparticles that are covered by small molecules is to use the functional groups of the small molecules to initiate polymerization. The development of controlled living radical polymerization allows the growth of polymer chains from the nanoparticle surface. The functional groups which

can initiate polymerization are introduced onto the surface of the nanoparticles, either by a coupling reaction, or the ligand exchange process. Polymerization can occur *via* atom transfer radical polymerization (ATRP),[50] nitroxide mediated polymerization (NMP),[51] or reversible addition-fragmentation chain transfer polymerization (RAFT).[52] These procedures primarily involve free radical polymerization. An alternative method is to graft polymer chains onto the surface of the Fe_2O_3 nanoparticles by a coupling reaction. However, the only successful result reported of this method involved the grafting of a PEO based polymer.[53]

A facile preparation of magnetic nanoparticles covered with polymer ligands is to prepare the nanoparticles in the presence of the polymeric surfactant directly. For example, the reduction of cobalt salt could be done in the presence of poly(acrylic acid)-*b*-polystyrene (PAA-*b*-PS). After a fractionation process, the obtained nanoparticles were found to have a narrow size distribution.[54] Pyun *et al.* reported the thermal decomposition of the precursor $Co_2(CO)_8$ in the presence of an end-functionalized PS surfactant.[55,56] Monodisperse cobalt particles were obtained without a size selective step. The polymeric surfactant used contained a neutral block and a functionalized terminal which could be a multidentate polymer block such as PAA or a single dentate group such as an amine, a carboxyl group or a phosphorus containing group. The preparation of Fe_3O_4 nanoparticles in the presence of several different polymer surfactants has been reported using a precipitation recipe. Homopolymer surfactants used in the preparation of Fe_3O_4 include poly(vinyl alcohol) (PVA),[57] poly(acrylic acid) (PAA),[58] and poly(methyl methacrylate) (PMMA).[59] Block copolymer surfactants used include PEO-*b*-PMMA [60]

and poly(ethylene oxide)-*b*-poly(glutamic acid).[61] This thesis will examine and discuss the preparation of cobalt nanoparticles *via* the thermal decomposition of $Co_2(CO)_8$ using PEO-*b*-PAA and PCEMA-*b*-PAA polymeric surfactants, respectively.

1.3 Hybrid materials from block copolymer and magnetic materials or nanoparticles

Magnetic nanoparticles covered by block copolymer surfactants are the simplest examples of a hybrid material formed by nanoparticles and block copolymers. More complicated hybrid structures can be obtained by combining the techniques of block copolymer self-assembly and nanoparticle preparation. Block copolymer self-assemblies incorporated with magnetic particles will retain the versatile morphologies of the self-assemblies and the magnetic properties of the nanoparticles. These magnetic materials have potential applications in building hierarchical magnetic devices that can be controlled by magnetic stimulation.

In this section, techniques for preparing magnetic nanopparticle-block copolymer hybrids will be discussed. Theoretically and practically, there are many examples of the hybrid materials formed by block copolymer and general inorganic nanoparticles, which are not necessarily magnetic.[62-66] In the absence of a magnetic field, the technique used for the hybridization of inorganic nanoparticles (which can be either magnetic or not) with polymers should be readily applied if magnetic particles are used. Therefore people can borrow the hybrid techniques developed with block copolymers and inorganic

nanoparticles, and apply them to prepare devices incorporating magnetic nanoparticles. One method is to build a template from polymers and subsequently load the magnetic particles into the template. The second method is to co-assemble the nanoparticles with block copolymers. The orientation of the nanoparticles will be affected by the composition of the block copolymer, while the morphology of the block copolymer will also be affected by the nature of the nanoparticles.[67] Another method is to mix the monomers of a polymer and the nanoparticles together *via* an emulsion process. The structure of the hybrid material will then be solidified by polymerizing the monomers *via* an emulsion polymerization.

1.3.1 Forming polymer/nanocrystal hybrids from polymer templates

The polymer templates used in this application should contain accessible functional groups, which can be used to stabilize the nanocrystals. Furthermore, it is desirable for the structure of the templates to be stable during the nanocrystal incorporation step. One approach is to prepare the nanoparticles and the template separately. The surface or cavity of the template can be treated to give it active sites, such as charges, which can absorb the nanoparticles. Alternatively, it is possible to grow the nanoparticles on an existing template. In this case, the nanoparticles would be formed at the locations of the functional groups on the template. For such a setup, the template would act as a macro-surfactant and stabilize the nanoparticles. The template for this type of nanoparticle growth could be a micelle in a block selective solvent, or a block copolymer assembly in the bulk state.

The binding of pre-made nanoparticles on the pre-made template provides good control of the size and shape of the nanoparticles as well as the polymer template characteristics. For example, polystyrene beads were prepared by emulsion polymerization. Magnetic Fe_3O_4 nanoparticles were then coated onto the beads by either electrical attraction, or by coupling with a binder.[68] The monodisperse beads that were obtained could be used for clinical diagnostic applications. Recently, Wang *et al.* used polystyrene-*b*-poly(4-vinylpyridine) (PS-*b*-P4VP) to form micelles as the template to absorb CdSe quantum dots on the surface.[69] The hydrophobic core of the micelle also encapsulated a conductive polymer, poly(3-hexylthiophenes) (P3HT). Electronic energy transfer was possible between the quantum dots and the conductive polymer. Generally, the nanoparticles were adsorbed onto the surface of the template. It was difficult to load the nanoparticles into the core of the template.

The formation of magnetic particles inside the template is a widely used technique to introduce nanoparticles into the core of the template. An innovative method is to use a template containing pores, in which the nanoparticles may form. For example, Antonietti *et al.* first reported the formation of gold nanoparticles in a microgel.[70] Breulamann *et al.* reported the formation of Fe_3O_4 nanoparticles in a polymer gel matrix.[71] Meanwhile, Andrade *et al.* reported the formation of Fe_3O_4 nanoparticles in a mesoporous polystyrene-divinylbenzene template, in which the pores were sulfonated.[72] Micelles have also been reported as templates, where the exposed functional groups are present

either in the core or on the surface. For example, Underhill *et al.* reported the preparation of magnetic spheres using crosslinked spherical micelles as a templates.[73] The micelles were obtained by dispersing polyisopropene-*b*-poly(2-cinnamoyloxylethyl methacrylate)-*b*-poly(*tert*-butyl acrylate) (PI-*b*-PCEMA-*b*-P*t*BA) in hexane. After the PCEMA block was crosslinked, and the P*t*BA block was converted into a poly(acrylic acid) (PAA) block. The micelles were stirred with $FeCl_2$ to introduce Fe^{2+} into the core of the micelle. Fe_2O_3 nanoaparticles were grown in the PAA core by oxidizing Fe^{2+} in the presence of H_2O_2. Similarly, Yan *et al.* reported the formation of magnetic nanoparticles in cylindrical micelles formed by dispersing poly(glyceryl methacrylate)-*b*-poly[(2-cinnamoyloxylethyl methacrylate)-*ran*-(hydroxylethyl methacrylate)]-*b*-poly(*tert*-butyl acrylate) (PGMA-*b*-P(CEMA-HEMA)-*b*-P*t*BA).[74] After the P*t*BA block was converted into PAA, Pd^{2+} ions were introduce by mixing the micelles with $PdCl_2$. Pd nanoparticles were formed in the PAA core by reacting $PdCl_2$ with $NaBH_4$. This was followed by the formation of Ni nanoparticles in the core, using the Pd nanoparticles as a catalysts. Liu *et al.* also reported the preparation of magnetic cylinders by forming Fe_3O_4 nanoparticles inside the cylinders, which were formed with PS-*b*-PCEMA-*b*-P*t*BA in the bulk state.[21] Cobalt nanoparticles can be formed in the micelle template using either reduction or thermal decomposition procedures. For example, Platonova *et al.* used PS-*b*-P4VP micelles as templates to grow Co nanoparticles using both the reduction and thermal decomposition methods.[75]

Alternatively, the template used to form nanoparticles can be a block copolymer self-assembly in the bulk state. In a bulk state, the film of a block copolymer is formed with a

micro-phase segregation between the blocks. The precursors of the nanoparticles can then be loaded into the domains which contain appropriate functional groups. The nanoparticles are then formed by reacting the precursors.[76-78] Another method involves forming a film from a mixture of block copolymers and nanoparticle precursors.[79,80]

1.3.2 Co-assembly of block copolymers with nanoparticles

The co-assembly of block copolymers and nanoparticles lead to highly ordered mesostructures. For example, Warren *et al.* [81] reported the preparation of a mesoporous Pt nanoparticle assembly by first mixing the Pt nanoparticle with polyisoprene-*b*-poly(dimethylaminoethyl methacrylate) (PI-*b*-PDMAEMA) diblock copolymers in solvent and then casting the mixture to form a film. After an annealing process, an ordered structure was formed with isolated spherical PI domains dispersed in a matrix, which contained a mixture of nanoparticle and PDMAEMA chains. The pores were generated after the PI chains were sculptured. In the co-assembly process, the microphase segregation of the block copolymer chains directs the distribution of the nanoparticles, and thereby introduces a tailored property into the composite. Another example of an assembly formed by mixing nanoparticles with a block copolymer involves the mixture of Au and SiO_2 nanoparticles with polystyrene-*b*-poly(ethylene-alt-propylene) (PS-*b*-PEP). This particular blend formed a lamellar structure, in which Au particles had migrated to the interface between the PS and PEP phases, and SiO_2 particles were dispersed in the PEP domain.[82]

The presence of nanoparticles can also tune the morphology of the block copolymer. Although little experimental evidence has been reported, some groups have studied such systems theoretically.[83-86] It is believed that the stretching of the polymer chains surrounding the nanoparticles results in a loss of entropy. Meanwhile, the interaction between the ligand covering the nanoparticle and the block copolymer chains affects the enthalpy. Therefore, the distribution of the nanoparticles in the block copolymer matrix could, theoretically, be tuned by adjusting the ligand and the size of the nanoparticles.

1.3.3 Magnetic nanoparticles hybrid with block copolymers by emulsion process

A spherical hybrid material composed of block copolymer and magnetic particles could be prepared by an emulsion process. One method is to form the hybrid structure after polymerizing the monomers, which have been premixed with nanoparticles by an emulsion process. An alternative procedure is to emulsify the mixture of the polymers and the nanoparticles together.

The method for preparing a hybrid structure *via* polymerization is well developed. In brief, the desired monomer and target magnetic nanoparticles are premixed with a surfactant. The monomer is then polymerized, normally using the emulsion polymerization process to form beads. The obtained magnetic beads are dispersed in the continuous phase due to the surfactant that was stabilizing the emulsion droplet. The amount of nanoparticles formed can be precisely tuned using this mixing process. For

example, Deng *et al.* reported the preparation of magnetic emulsions by mixing Fe_3O_4 nanoparticles with *N*-isopropylacrylamide (NIPAM) monomers, and subsequently polymerizing the monomer into poly(*N*-isopropylacrylamide) (PNIPAM).[87] Holzapfel *et al.* prepared magnetic beads by mixing Fe_3O_4 nanoparticles with styrene and polymerizing the styrene *via* a miniemulsion process.[88] Pich *et al.* prepared magnetic beads with a Fe_3O_4 core by polymerizing styrene and acetoacetoxyethyl methacrylate in the presence of the magnetic nanoparticles. These nanoparticles were encapsulated by the polymer bead during the emulsion process.[78]

Another approach used to prepare magnetic particle hybrid spheres *via* emulsion is to emulsify the nanoparticles with pre-synthesized polymer directly. For example, Liu *et al.* used block copolymer surfactants to stabilize an oil phase containing magnetic particles.[89] In this water-in-oil emulsion process, a water dispersion of iron oxide particles was added into an oil phase (toluene) containing P*t*BA-*b*-PHEMA block copolymers. The aqueous phase was stabilized by the anchored PHEMA block, while the P*t*BA chains provided dispersibility for the emulsion droplet. After the PHMEA chains were chemically crosslinked, the P*t*BA chains were hydrolyzed into PAA, so that the spheres in the emulsion became water dispersible. Such magnetic spheres could be used in diagnostic applications.

1.3.4 Applications of magnetic beads in immunoassays

Immunoassays refer to the identification and quantification of a substance of interest in a biological fluid such as blood serum or urine, typically by reacting antibodies to their corresponding antigens.[90] Today, immunoassays play an important role in the analysis of many clinical laboratory analytes such as proteins, hormones, drugs and nucleic acids.[91] Automated heterogeneous immunoassays were developed to provide rapid results, which are critical to guide early intervention in certain clinical situations. In addition, automation can minimize variation, which is inherent in manual techniques. It also decreases labor costs and improves laboratory throughput.[92] A few automated heterogeneous immunoassays, such as the ACCESS assay and the ACS:180 assay, were developed by using paramagnetic or superparamagnetic particles.

ACS:180 assays allow for a rapid, simple and effective immunoassay for a broad range of biospecies. A typical ACS:180 assay begins by binding the target biomolecules onto the superparamagnetic particles or magnetic beads in a reaction cuvette.[93] Prior to the analysis of an antibody in a biological sample, such as blood serum or urine, the antigen for the antibody is immobilized on the magnetic particles. During the analysis step, two different approaches are frequently used, the competitive approach and the sandwich-type approach. In a typical competitive approach, the antibody sample to be analyzed and a pre-labelled chemiluminescence-based antibody are both added to the dispersion of the magnetic particles. The two types of antibodies compete for the antigen binding sites. In a typical sandwich-type approach (Figure 1.10), the antibody binds with the antigen on the magnetic particles first. The bound antibody then binds with a pre-labelled chemiluminescent-based anti-antibody. In both approaches the superparamagnetic

particles are pulled to one side of the reaction cuvette by introducing a magnetic field; and the remaining assay mixture is removed. After the supernatant has been discarded, a chemiluminescent reaction of the chemiluminescence-based segments on the superparamagnetic particles is triggered. Light emission signals are collected as relative light units (RLU). For each analyte and assay approach, a calibration curve, or dose-response curve, relating concentration to RLU is necessary. The concentration of antibody is then determined by referring to this calibration curve.

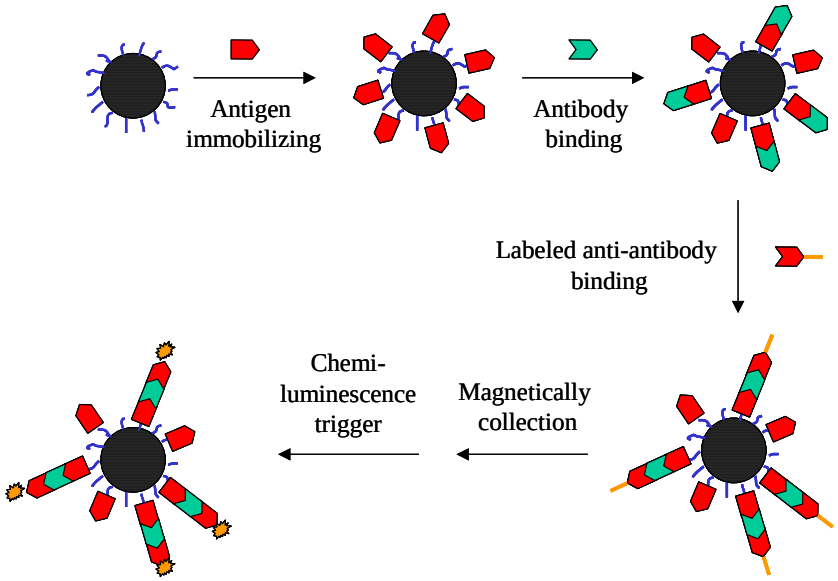

Figure 1.10. Sandwich type immunoassay using magnetic beads to pre-concentrate the analyte.

In an ACS:180 immunoassay, magnetic beads are the essential apparatus and they serve to enrich and purify analyte found in the biological sample and enable an accurate assay. These magnetic particles are tagged by immobilizing different antigens, antibodies or other analytes onto their surfaces. Thus the assay is able to analyze different antigens and

other target biomolecules by changing the initially immobilized molecules on the surfaces of the magnetic beads.

1.4 Emulsion

1.4.1 Some theories describing emulsion

Emulsions are colloidal systems composed of droplets of a liquid (dispersed phase) which are dispersed into another immiscible liquid (continuous phase). If the continuous phase is water, while the dispersed phase is an immiscible oil, such an emulsion system is called an oil-in-water (O/W) emulsion. If the emulsion consists of an immiscible oil continuous phase, while the dispersed phase is water, this is called a water-in-oil (W/O) emulsion. Normally, the emulsion consists of spherical droplets stabilized by a surfactant. The surfactant should be an amphiphilic molecule, which has a hydrophobic end and a hydrophilic end. During the oil-in-water emulsion process, the surfactant becomes anchored onto the surface of the oil droplet by contacting its hydrophobic end with the droplet while extending its hydrophilic end into the water phase. Therefore, a surfactant layer is formed at the oil-water interface, so that the surface free energy is decreased. The surfactant can be a small molecule or a polymer. Emulsions are formed by agitating the liquid mixture by either shearing or ultrasonication. One important application of the emulsion process is emulsion polymerization, in which monomer droplets are stabilized by surfactants and polymerized in the presence of an initiator.

The creation of an emulsion involves two main stages.[94] For example, for a shear induced oil-in-water process, originally the oil phase that is mixed with the water phase is separated into 'mother droplets'. At the first stage, these mother droplets are elongated into threads, and then broken into smaller daughter droplets in the presence of a shearing force that is sufficient to overcome the surface tension of the mother droplet. Figure 1.11 shows optical microscopy images of this process.[94] The duration of this stage is normally less than one second. In the second stage, the daughter droplets are further deformed into smaller droplets, normally in a matter of minutes. The deformation and breaking of the mother droplets only happens when the shear stress overcomes half of the Laplace pressure, which is defined as the ratio between the surface tension and the radius of the mother droplet. The ratio between the shear stress and the Laplace value is called the capillary number. There is a critical capillary number for a specific emulsion system. If the capillary number of the droplets is greater than the critical capillary number, the droplets will be broken, otherwise the droplets will not be broken any further.

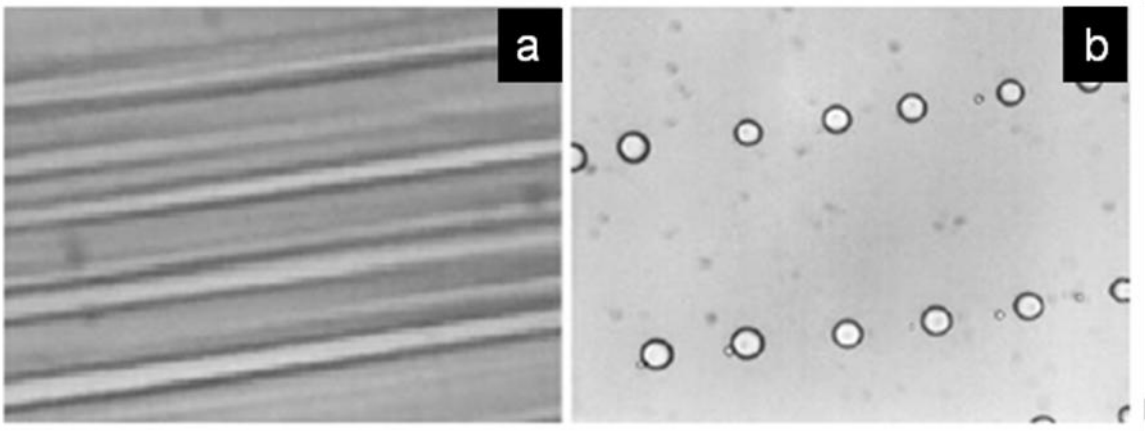

Figure 1.11 The deformation of the mother droplets into daughter droplets under shearing.[94]

The existence of the critical capillary number indicates that the size of the final emulsion droplets is affected by the shear stress and the surface tension of the oil-water interface.[94] The shear stress is the product of shear rate and the viscosity of the continuous phase. The following equation can be derived:

$$C_a = \eta\gamma R/\sigma \qquad (1.5)$$

According to this equation, the size of the spheres in the emulsion increases proportionally with decreasing viscosity of the continuous phase and the shear rate. The surface tension is determined by the nature of the surfactant and liquids involved. An increase of the surface tension results in an increase in size of the emulsion droplets. Besides the parameters mentioned above, the size of the emulsion spheres is also related to the viscosity ratio between the dispersed phase and the continuous phase. However, in most cases, this viscosity ratio majorly affects the size distribution of the emulsion's spheres. Schmitt *et al.* reported that emulsion spheres with a narrowly size distribution can only be produced when the viscosity ratio is in the range of 0.01 to 2.[94] A well controlled emulsion can be created with a device called a couette mixer, which can generate a lamellar flow so that the shear stress is uniform. Using this device, uniform magnetic emulsion spheres were prepared by Montagne and coworkers.[95]

The core of the emulsion droplets can be composed of polymers or nanoparticles in order to introduce novel properties to the emulsion droplets. For example, Liu *et al.* used a polymeric surfactant to produce emulsion droplets which contain a phase segregated block copolymer.[96] Another example is to use a block copolymer as a surfactant to stabilize an oil phase containing magnetic particles, as discussed in Section 1.3.3.

Furthermore, the dispersed phase of an emulsion could be incorporated with other materials which are soluble or dispersible in that phase. For example, in order to adjust the viscosity ratio between the dispersed phase and the continuous phase, neutral polymers were dissolved in the continuous phase so that its viscosity increased. Consequently, the size distribution of the obtained emulsion spheres became narrower.[94]

1.4.2 Emulsions stabilized with block copolymers

Amphiphilic block copolymers consist of a hydrophilic block and a hydrophobic block. This structure allows these polymers to be used as surfactants in an emulsion process. For example, an AB diblock copolymer, in which A has an affinity with the solvent surrounding the droplet and B has an affinity to the surface of the droplet, becomes anchored on the surface of an emulsion droplet by contacting the B block with the droplet and stretching the A block into the solvent. The conformation of the stretched out A block is called tail. The scheme of anchoring AB block copolymers onto droplets is shown in Figure 1.12. The B block interacts with the droplet in trains which are the segment contacting the surface directly. There are also loop segments which are in-between the trains pointing towards the solvent (as shown in Figure 1.12).

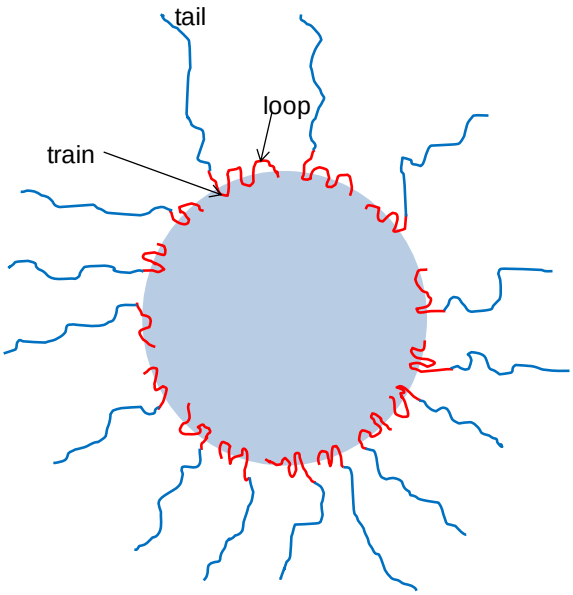

Figure 1.12 Conformations of block copolymer surfactants anchored on the surface of an emulsion droplet.

When the polymer chains are adsorbed onto the surface of a droplet, the system loses conformation entropy. This must be compensated for by the adsorption energy provided by the interaction between the B block and the surface. The adsorption energy of each repeating unit of the B block (χ^s) is small, but the total adsorption energy provided by the B block ($N\chi^s$), where N is the number of repeating units of B that is interacting with the surface) is large due to the large number of the repeating units. Scheutijens and Fleer theoretically studied the adsorption of the polymer chains on a droplet's surface using a step weighted random walk approach.[97,98] Based on the theory developed by Scheutijens and Fleer, for a fixed value of χ^s of 1 kT, the amount of polymer chains absorbed per unit area of the surface coverage (Γ) increased with the total number of repeating units of B (N), which may or may not interact with the interface. When N is greater than 20, high

affinities are obtained, and when n is greater than 100, irreversible absorption occurs. Surface coverage (Γ) increases as the concentration of the block copolymer surfactant increases. At low polymer concentrations, polymers with longer chains are more readily anchored onto droplet surface than shorter polymers. However, if the concentration of the polymer chains in the solvent is very high, the adsorption of the longer polymer chains is affected by the decrease of the conformation entropy. The solvent also affects the adsorption of the polymer chains. If the solvent is a poor solvent for the B block, the amount of adsorbed B blocks is much higher than when the solvent is a theta solvent.

Polymer chains anchored onto the surface of an emulsion droplet provide a steric stabilization effect between the droplets which prevents flocculation and coalescence. In this scenario, the surface of a droplet could be treated as a layer of overlapping polymer brushes. To minimize the segment-segment interactions, the chains will stretch out perpendicular to the surface of the droplet, an action associated with a decrease in the conformational entropy.[99] The length of a stretched chain is much greater than the end-to-end distance of the polymer in the random coil conformation. To evaluate the steric effect of the polymer chains, suppose two droplets bearing AB block copolymer surfactants approach one another (Figure 1.13). The stretching A blocks on the two droplets have two potential interactions. The polymer chains could overlap or mix, acting as brushes, or the polymer chains may undergo compression into a solid layer. Generally, the mixing of surfactant chains on adjacent droplets increases the osmotic pressure of the overlapping regime. This is an energetically unfavoured conformation when the mixing chains are polymer chains rather than small molecule surfactants. The compression

between the polymer chains on adjacent droplets may restrict the possible conformations of the polymer chains, which would lead to a decrease in entropy. Thus, when using polymeric surfactants, a high energy barrier prevents the flocculation and coalescence of the droplets.[100]

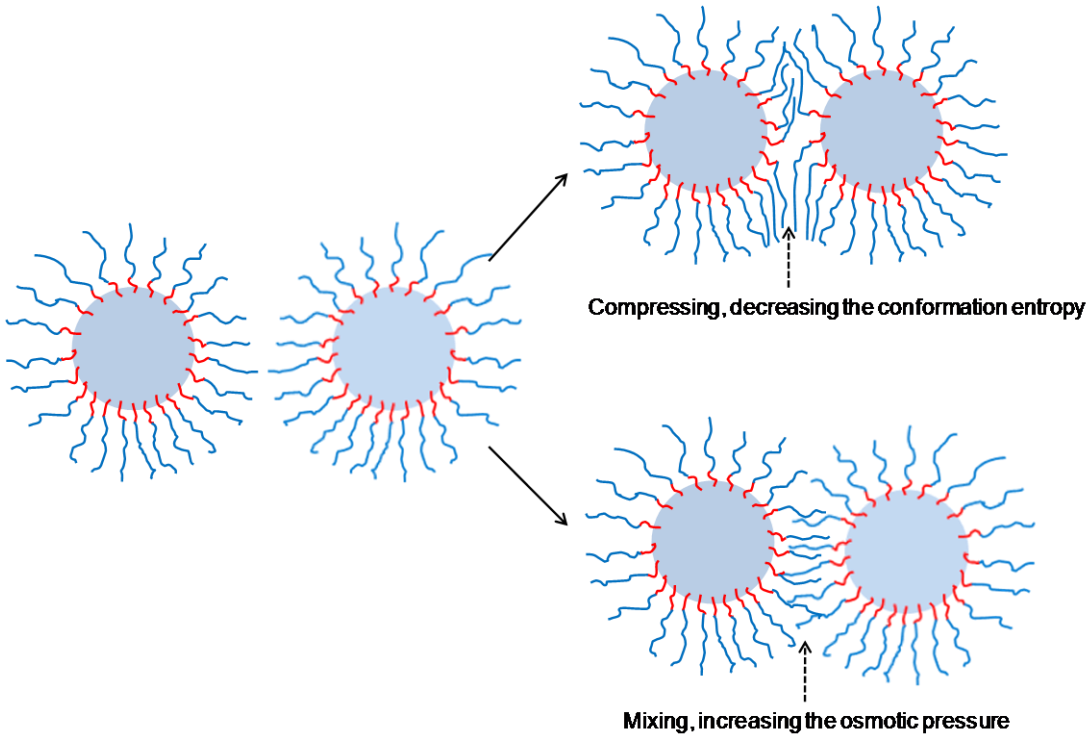

Figure 1.13 The steric effect of diblock polymer surfactants stabilizing emulsion droplets.

There are many examples of emulsion processes that use block copolymers as surfactants to stabilize the droplets. For example, poly(1,2-hydroxystearic acid)-*b*-poly(ethylene oxide)-*b*-poly(1,2-hydroxystearic acid) or PHS-*b*-PEO-*b*-PHS can be used to stabilize either O/W or W/O emulsions.[101] In the water-in-oil emulsion process, the PEO chains act as the anchor chains while the PHS chains act as the anchor chains in oil-in-water emulsion. In another example, narrow size distributed emulsion droplets were stabilized with poly(vinyl acetate)-*b*-poly(vinylic acid) or PVAAc.[100] With all other experimental

conditions kept the same, the sizes of the emulsion droplets formed using this polymeric surfactant were compared with those of emulsion droplets formed using small molecule surfactants. No fundamental changes were observed, except for the average size of the emulsion droplets. This happened because the interfacial tension between the droplet and the continuous phase is greater when polymeric surfactants were used than when the small molecule surfactants were used. As expected, the size of the droplets that were stabilized by polymeric surfactants had larger diameters than with those stabilized with small molecule surfactants.

1.5 Summary of the research projects

The remainder of this thesis consists of the following chapters.

Chapter 2 will review some of the characterization techniques used in this thesis.

Chapter 3 describes the study of the morphology of PGMA-*b*-PCEMA-*b*-P*t*BA nano aggregates. Discussion will focus on the morphological variation associated with the ratios between the different blocks. The cylindrical aggregates were modified by swelling the core phase in a mixed solvent system so that a channel shaped cavity was generated in the cylinder. The ability to control the width of the channel by controlling exposure time to the swelling agent is also presented.

In Chapter 4, the synthesis of narrow size distributed cobalt nanoparticle via a thermal decomposition process in the presence of block copolymer surfactants is presented. This

method provides a facile way to incorporate block copolymers onto the surface of inorganic crystals. Afterwards, another block copolymer will be anchored onto the polymer covered cobalt nanoparticle to build a permanently locked cobalt nano wire. The useful magnetic properties of the cobalt nano wire are also described.

Chapter 5 describes the preparation of magnetic emulsion spheres via an oil-in-water emulsion process using two block copolymers as surfactants. The obtained emulsion spheres have two types of segregated surface chains due to their incompatibility with each other. The chain segregation is adjustable by changing the ionic concentration in the water phase. A systematic study reveals that the shear rate and the viscosity ratio between the oil and water phases affects the size and size distribution of the resulting spheres in a way comparable to that of an emulsion stabilized by small molecule surfactants. The obtained spheres could be used for binding with antigens for the selective capture of antibodies.

In the appendix, the one-pot synthesis of cobalt nanoparticles in the presence of a polymeric ligand was developed as a preliminary study for Chapter 4. The block copolymer PEG-*b*-PAA was used as the ligand in this experiment. The results demonstrated that the size of the cobalt particles can be controlled by varying the ratio between the polymer surfactant and the precursor of the cobalt crystals.

Chapter 6 will summarize the thesis and give some future research comments.

References

1. Riess, G.; Hurtrez, G.; Bahadur, P. *Block copolymers, 2nd ed. Encyclopedia of polymer science and engineering*, New York: Wiley; 1985.

2. Vriezema, D. M.; Aragones, M. C.; Elemans, J.; Cornelissen, J.; Rowan, A. E.; Nolte, R. J. M. *Chem. Rev.* **2005**, *105*, 1445.

3. Li, Z.; Zhao, W.; Liu, Y.; Rafailovich, M. H.; Sokolov, J.; Khougaz, K.; Eisenberg, A.; Lennox, R. B.; Krausch, G. *J. Am. Chem. Soc.* **1996**, *118*, 10892.

4. Massey, J. A.; Winnik, M. A.; Manners, I.; Chan, V. Z. H.; Ostermann, J. M.; Enchelmaier, R.; Spatz, J. P.; Möller, M. *J. Am. Chem. Soc.* **2001**, *123*, 3147.

5. Bates, F. S.; Fredrickson, G. H. *Phys. Today* **1999**, *52(2)*, 32.

6. Khandpur, A. K.; Forster, S.; Bates, F. S.; Hamley, I. W.; Ryan, A. J.; Bras, W.; Almdal, K.; Mortensen, K. *Macromolecules* **1995**, *28*, 8796.

7. Zheng, W.; Wang, Z. *Macromolecules* **1996**, *28*, 7215.

8. Riess, G. *Prog. Polym. Sci.* **2003**, *28*, 1107.

9. Monk, P.; Tuzar, Z *Solvents and self-organization of polymer. NATO ASI series, series E: applied sciences vol. 327.* Dordrecht: Kluwer Academic Publisher 1996.

10. Zhang, L.; Eisenberg, A. *Science* **1995**, *268*, 1728.

11. Cameron, N. S.; Corbierre, M. K.; Eisenberg, A. *Can. J. Chem.* **1999**, *77*, 1311.

12. Lei, L.; Gohy, J.; Willet, N.; Zhang, J.; Varshney, S.; Jérôme, R. *Macromolecules* **2004**, *37*, 1089.

13. Zhang, W.; Shi, L.; An, Y.; Gao, L.; Wu, K.; Ma, R.; Zhang, B. *Macromolecular Chem. Phys.* **2004**, *205*, 2017.

14. Luo, K.; Yang, Y. *Polymer* **2004**, *45*, 6745.

15. Kim, H.-C.; Russell T. P. *J. Polym. Sci. B: Polym. Phys.* **2001**, *39*, 663.

16. Morkved, T. L.; Lu, M.; Urbas, A. M.; Ehrichs, E. E.; Jaeger, H. M.; Mansky, P.; Russell, T. P. *Science*, **1996**, *273*, 931.

17. Xiang, H.; Shin, K.; Kim, T.; Moon, S. I.; McCarthy, T. J.; Russell, T. P. *Macromolecules* **2004**, *37*, 5660.

18. Liu, G.; Yan, X.; Li, Z.; Zhou, J.; Duncan, S. *J. Am. Chem. Soc.* **2003**, *125*, 14039.

19. Comparelli, R.; Zezza, F.; Striccoli, M.; Curri, M. L.; Tommasi, R.; Agostiano, A. *Mater. Sci. Eng. C* **2003**, *23*, 1083.

20. Pyun, J. *Polymer Reviews* **2007**, *47*, 231.

21. Lu, Z.; Liu, G.; Philips, H.; Hill, J. M.; Chang, J.; Kydd, R. A. *Nano Lett.* **2001**, *1*, 683.

22. Yan, X; Liu, G.; Liu, F.; Tang, B. Z.; Pang, H.; Pakhomov, A. B.; Wong, C. Y. *Angew. Che. Imt. Ed.* **2001**, *40*, 3593.

23. LaMer, V. K.; Dinegar, R. H. *J. Am. Chem. Soc.* **1950**, ***72***, 4847.

24. Puntes, V. F.; Krishnan, K. M.; Alivisatos, A. P. *Science* **2001**, *291*, 2115.

25. Buffat, P.; Borel, J. P. *Phys. Rev. A* **1976**, *13*, 2287.

26. Riess, H. *J. Chem. Phys.* **1951**, *19*, 482.

27. Yin, Y.; Alivisatos, A. P. *Nature* **2005**, *427*, 664.

28. Murray, C. B.; Norris, D. J.; Bawendi, M. G. *J. Am. Chem. Soc.* **1993**, *115***,** 8706.

29. Xia, Y.; Xiong, Y.; Lim, B.; Skrabalak, S. E. *Angew. Chem. Int. Ed.* **2008**, *47*, 2.

30. Peng, X.; Mann, L.; Wickham, J.; Kadvanish, A.; Alivisatos, A. P. *Nature*, **2000**, *404*, 59.

31. Puntes, V. F.; Krishnan, K. M.; Alivisatos, A. P. *Appl. Phys. Lett.* **2001**, *78*, 2187.

32. Jeong, U.; Teng, X.; Wang, Y.; Yang, H.; Xia, Y. *Adv. Mater.* **2007**, *19*, 33.

33. Klokkenburg, M.; Vonk, C.; Claesson, E. M.; Meeldijk, J. D.; Erne, B. H.; Philipes, A. P. *J. Am. Chem. Soc.* **2004**, *126*, 16706.

34. Sun, S. H.; Murray, C. B. *J. Appl. Phys.* **1999**, *85*, 4325.

35. Puntes, V. F.; Zanchet, D.; Erdonmez, C. K.; Alivisatos, A. P. *J. Am. Chem. Soc.* **2002**, *124*, 12874.

36. Casula, M. F.; Jun, Y. W.; Zaziski, D. J.; Chan, E. M.; Corrias, A.; Alivisatos, A. P. *J. Am. Chem. Soc.* **2006**, *128*, 1675.

37. Wang, J.; Sun, J.; Sun, Q.; Chen, Q.; *Mater. Res. Bul.* **2003**, *38*, 1113.

38. Yogo, T.; Nakamura, T.; Sakamoto, W.; Hirano, S. *J. Mater. Res.* **1999**, *14*, 2855.

39. Bodnarchuk, M. I.; Kovalenko, M. V.; Groiss, H.; Resel, R.; Reissner, M.; Hesser, G.; Lechner, R. T.; Steiner, W.; Schaffler, F.; Heiss, W. *Small* **2009**, *5*, 2247.

40. Harris, L. A.; Goff, J. D.; Carmichael, A. Y.; Riffle, J. S.; Harburn, J. J.; St. Pierre, T. G.; Saunders, M. *Chem. Mater.* **2003**, *15*, 1367.

41. Park. J.; An, K.; Hwang, Y.; Park, J.; Noh, H.; Kim, J.; Park, J.; Hwang, N.; Hyeon, T. *Nat. Mater.* **2004**, *3*, 891.

42. Kovalenko, M. V.; Bodnarchuk, M. I.; Lechner, R. T.; Hesser, G.; Schaffler, F.; Heiss, W. *J. Am. Chem. Soc.* **2007**, *129*, 6352.

43. Kim, D.; Lee, N.; Park, M.; Kim, B. H.; An, K.; Hyeon, T. *J. Am. Chem. Soc.* **2009**, *131*, 454.

44. Jana, N. R.; Chen, Y.; Peng, X. *Chem. Mater.* **2004**, *16*, 3931.

45. Hyeon, T.; Lee, S. S.; Park, J.; Chung, Y.; Na, H. B. *J. Am. Chem. Soc.* **2001**, *123*, 12798.

46. Teng, X.; Yang, H. *J. Mater. Chem.* **2004**, *14*, 774.

47. Yu, D.; Sun, X.; Zou, J.; Wang, Z.; Wang, F.; Tang, K. *J. Phys. Chem. B* **2006**, *110*, 21667.

48. Wang, X.; Dykstra, T. E.; Salvador, M. R.; Manners, I.; Scholes, G. D.; Winnik, M. A. *J. Am. Chem. Soc.* **2004**, *126*, 7784.

49. Xie, J.; Xu, C.; Kohler, N.; Hou, Y.; Sun, S. *Adv. Mater.* **2007**, *19*, 3163.

50. Wang, Y.; Teng, X.; Wang, J. S.; Yang, H. *Nano Lett.* **2003**, *3*, 789.

51. Matsuno, R.; Yamamoto, K.; Otsuka, H.; Takahara, A. *Chem. Mater.* **2003**, *15*, 3.

52. Wang, W. C.; Neoh, K. G.; Kang, E. T. *Macromol. Rapid Commun.* **2006**, *27*, 1665.

53. Zhang, Y.; Kohler, N.; Zhang, M. *Biomaterials* **2002**, *23*, 1553.

54. Liu. G.; Yan, X.; Lu, Z.; Curda, S. A.; Lal, J. *Chem. Mater.* **2005**, *17*, 4985.

55. Korth, B. D.; Keng, P.; Shim, I.; Bowles, S. E.; Tang, C.; Kowalewski, T.; Nebesny, K. W.; Pyun, J. *J. Am. Chem. Soc.* **2006**, *128*, 6562.

56. Keng, P. Y.; Shim, I.; Korth, B. D.; Douglas, J. F.; Pyun, J. *ACS Nano* **2007**, *1*, 279.

57. Lee, J.; Isobe, T.; Senna, M. *J. Colloid Interface Sci.* **1996**, *177*, 490.

58. Thakur, M.; De, K.; Giri, S.; Si, S.; Kotal, A.; Mandal, T. K. *J. Phys.: Condense Matter* **2006**, *18*, 9093.

59. Abu-Much, R.; Meridor, U.; Frydman, A.; Gedanken, A. *J. Phys. Chem. B* **2006**, *110*, 8194.

60. Wormuth, K. *J. Colloid Interface Sci.* **2001**, *241*, 366.

61. Thuenemann, A. F.; Schuett, D.; Kaufner, L.; Pison, U.; Moehwald, H. *Langmuir* **2006**, *22*, 2351.

62. Yager, K. G.; Berry, B. C.; Page, K.; Patton, D.; Karim, A.; Amis, E. J. *Soft Matter* **2009**, *5*, 622.

63. Fabio, D. A.; Reis, A. *Macromolecules* **2008**, *41*, 8932.

64. Satoshi Akasaka, S.; Hiroki Mori, H.; Taketsugu Osaka, T.; Vincent H. Mareau, V. H.; Hasegawa, H. *Macromolecules* **2009**, *42*, 1194.

65. Xu, C.; Ohno, K.; Ladmiral, V.; Milkie, D. E.; Kikkawa, J. M.; Composto, R. J. *Macromolecules*, **2009**, *42*, 1219.

66. Haryyono, A.; Binder, W. H. *Small*, **2006**, *2*, 600

67. Balazs, A. C.; Emrick, T.; Russell, T. P. *Science* **2006**, *314*, 1107.

68. Sutor, J. J. U.S. Patent 5,648,124, 1997.

69. Wang, M.; Kumar, S.; Lee, A.; Felorzabihi, N.; Shen, L.; Zhao, F.; Froimowicz, P.; Scholes, G. D.; Winnik, M. A. *J. Am. Chem. Soc.* **2008**, *130*, 9481.

70. Antonietti, M.; Grohn, F.; Hartmann, J.; Bronstein, L. *Angew. Chem. Int. Ed.* **1997**, *36*, 2080.

71. Breulamann, M.; Davis, S. A.; Mann, S.; Hentze, H.-P.; Antonietti, M. *Adv. Mater.* **2000**, *12*, 502.

72. Andrade, S. S.; Rabelo, D.; Garg, V. K.; Oliverira, A. C.; Morais, P. C. *J. Magn. Magn. Mater.* **2005**, *289*, 25.

73. Underhill, R. S.; Liu, G. *Chem. Mater.* **2000**, *12*, 2082.

74. Yan, X.; Liu, G.; Haeussler, M., Tang, B. Z. *Chem. Mater.* **2005**, *17*, 6053.

75. Platonova, O. A.; Bronstein, L.; Solodovnikov, S. P.; Yanovskaya, I. M.; Obolonkova, E. S.; Valetsky, P. M.; Wenz, E.; Antonietti, M. *Colloid polym. Sci.* **1997**, *275*, 426.

76. Tadd, E. H.; Bradley, J.; Tannenbaum, R. *Langmuir* **2002**, *18,* 2378.

77. Goubault, C.; Jop, P.; Fermigier, M.; Baudry, J.; Bertrand, E.; Bibette, J. *Phys. Rev. Lett.* **2003**, *91*, 260802/1.

78. Pich, A.; Bhattacharya, S.; Ghosh, A.; Adler, H. J. P. *Polymer* **2005**, *46*, 4596.

79. Sohn, B. H.; Cohen, R. E. *Chem. Mater.* **1997**, *9*, 264.

80. Abes, J. I.; Cohen, R. E.; Ross, C. A. *Chem. Mater.* **2003**, *15*, 1125.

81. Warren, S. C.; Messina,L. C.; Slaughter, L. S.; Kamperman, M.; Zhou, Q.; Gruner, S. M.; DiSalvo, F. J.; Wiesner, U. *Science* **2008**, *320*, 1748.

82. Bockstaller, M. R.; Lapetnikov, Y.; Margel, S.; Thomas, E. L. *J. Am. Chem. Soc.* **2003**, *125*, 5276.

83. Gaines, M. K.; Smith, S. D.; Samseth, J.; Bockstaller, M. R.; Thompson,R. B.; Rasmussen, K. Ø .; Spontak, R. J. *Soft Matter* **2008**, *4*, 1609.

84. Lee, J. Y.; Shou, Z; Balazs, A. C. *Macromolecules* **2003**, *36*, 7730.

85. Lin, Y.; Böker, A.; He, J.; Sill, K.; Xiang, H.; Abetz, C.; Li, X.; Wang, J.; Emrick, T.; Long, S.; Wang, Q.; Balazs, A.; Russell, T. P. *Nature* **2005**, *434*, 55.

86. Sknepnek, R.; Anderson, J. A.; Lamm, M. H.; Schmalian, J.; Travesset, A. *ACS Nano* **2008**, *2*, 1259.

87. Deng, Y.; Yang, W.; Wang, C.; Fu, S. *Adv. Mater.* **2003**, *15*, 1729.

88. Holzapfel, V.; Lorenz, M.; Weiss, C. K.; Schrezenmeier, H.; Landfester, K.; Mailaender, V. *J. Physics: Condensed Matter* **2006**, *18*, S2581.

89. Liu, G.; Yang, H.; Zhou, J. *Biomacromolecules* **2005**, *6*, 1280.

90. Van Emon, J. M. *Immunoassay and other bioanalytical techniques*, CRC press, Taylor & Francis Group 2007.

91. Wu, H. B. *Clin. Chim. Acta* **2006**, *369*, 119.

92. Boland J.; Garey G.; Krodel E.; Kwiatkowski M. *Clin. Chem.* **1990**, *36*(9), 1598.

93. David Wild *The Immunoassay Handbook 2nd Ed*. Nature Publishing Group, New York, 2001.

94. Schmitt, V.; Leal-Calderon, F.; Bibette, J. *Top. Curr. Chem.* **2003**, *227*, 195.

95. Montagne, F.; Mondian-Monval, O.; Pichot, C.; Mozzanega, H.; Elaissari, A. *J. Magn. Magn. Mater.* **2002**, *250*, 302.

96. Lu, Z.; Liu, G.; Liu, F. *Macromolecules* **2001**, *34*, 8814.

97. Scheutijens, J. M. H. M.; Fleer; G. J. *J. Phys. Chem.* **1979**, *83*, 1919.

98. Scheutijens, J. M. H. M.; Fleer; G. J. *Adv. Colloid Interface Sci.* **1982**, *16*, 341.

99. Milner, S. T. *Science* **1991**, *251*, 905.

100. Tadros, T. *Adv. Colloid Interface Sci.* **2009**, *147-148*, 281

101. Tadors, T.; Dederen, C.; Taelman, M. C. *Cos. Toi.* **1997**, *112*, 75.

Chapter 2

Characterization of polymers and polymer-based nanostructures

This section will discuss the characterization of the polymers that were used, as well as the nanostructures that were built from these polymers. The characterization of the polymers is achieved by determining their composition, molecular weight and molecular weight distribution. The composition of the polymers was determined by nuclear magnetic resonance (NMR) spectroscpoy, in order to provide information about the nature of the polymer backbone, the nature of the side groups or functional groups connected to the backbone, the end groups of the polymer chains, and the molar ratios between the different blocks. The molecular weight and size of the polymers were analyzed by light scattering (LS), and gel permeation chromatography (GPC), which is also referred to as size exclusive chromatography (SEC). The morphologies of the nanostructures, as well as their compositions, were studied by transmission electron microscopy (TEM) and atomic force microscopy (AFM). Additional experiments to determine the composition of the nanostructures were done with thermal gravmetry analysis (TGA). Finally, spectral techniques such as UV-visible, FT-IR, and fluorescence spectroscopy were also used to characterize the polymers and their polymeric nanostructures.

2.1 Characterization of polymers

2.1.1 ^{1}H NMR spectroscopy

Nuclear magnetic resonance (NMR) spectroscopy is a popular method to characterize the composition of a chemical. The nucleus of an atom, which is composed of protons and neutrons, has an intrinsic spin property. The overall spin of the nucleus is characterized by the spinning quantum number (*s*). If *s* is not zero, the nucleus has degenerated spin states, which have the same energy level when not exposed to an external magnetic field. However, when placed in a magnetic field (H_0), the degenerated spinning states split to different energy levels. If an electromagnetic radiation is then applied and the frequency of the radiation (ν_o) is exactly the value to allow the photon of the radiation to have an energy ($h\nu_o$) that is equal to the energy gap (ΔE) between the spinning states of the nucleus, the photon will be absorbed and excite the nucleus from the lower energy level to a higher energy level. This process is called nuclear magnetic resonance.[1] The frequency (ν_o) is called the Larmor frequency. The relation between the frequency and the magnetic field is given by:

$$\nu_0 = \frac{gH_0}{2\pi} \qquad (2.1)$$

Where g is the magnetogyric ratio.[2] The NMR signal is collected as the nucleus relaxes from the higher energy level to the lower energy level.. In a modern NMR instrument, a superconducting magnet is used while a short pulse of radiofrequency is applied to excite the nuclei to higher energy states. The nuclei relax to the lower energy state, and this is

detected as an interferogram or known as a free induction decay (FID). This FID will be converted into an NMR spectrum by Fourier transformation. The proton (^{1}H) nucleus is the most commonly used for NMR spectroscopy.

A nucleus can be affected by the magnetic dipoles of neighbouring nuclei. Therefore, the frequency of the electromagnetic radiation to generate nuclear magnetic resonance is affected by the chemical environment of the proton.[3] In the same way that NMR spectroscopy provides information about small molecules, it can also provide information about the structure of a polymer chain, and which functional groups are connected to the polymer backbone. For copolymer systems, ^{1}H NMR spectroscopy can be used to determine the ratio between the different types of repeating units present in the polymer. For samples of small molecules, Brownian motion can lead to the cancellation of neighbouring magnetic fields experienced by the nucleui, due to the rapid changes in the orientations of the molecules. However, the mobility of a polymer chain is less than that of a small molecule. Therefore, the net magnetic dipole surrounding a nucleus is not zero, and this leads to the broadening of the signal.[4] Furthermore, the relaxation times of polymeric samples are longer than those of smaller molecules. The relaxation duration of a sample is related to the dipole-dipole interactions occurring between the molecules, which are affected by the mobility of these molecules.[4] Since polymer samples generally have a lower mobility than smaller molecules, during the aquisition of their ^{1}H NMR spectra the relaxation delay should be adjusted to a longer value (three seconds was used for the experiments described in this thesis).

2.1.2 Gel permeation chromatography

The molecular weight of a polymer can be obtained by GPC analysis. GPC is performed by passing a polymer sample through a series of columns which are packed with gels containing pores. The hydrodynamic radius (R_h) of a polymer is related to its molecular weight. When polymers with different hydrodynamic radii pass through a GPC column, the smaller polymers are more likely to become entrapped in the pores of the gels, which leads to longer retention times for small polymers as the polymeric sample is eluted through the column. Consequentially, larger polymer chains pass through the columns more quickly. Therefore, the GPC separates polymer chains based on their size. This process is illustrated in Figure 2.1.

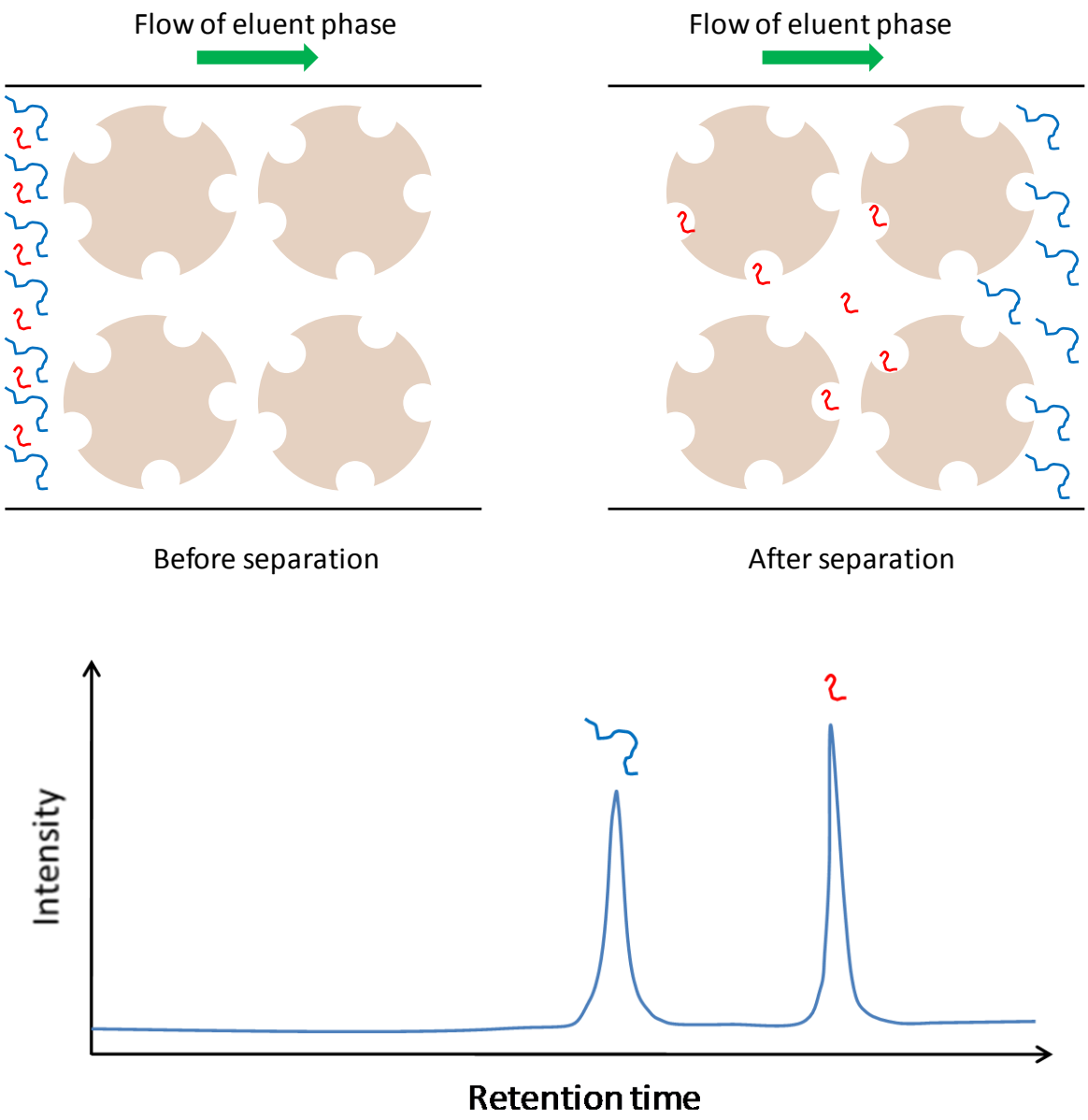

Figure 2.1. The separation of polymers in a GPC column, based on the differences of their hydrodynamic diameters.

After the polymer sample passes through the column, it is detected by a detector. Since the sample has been separated according to size, an indirect measurement of the polymer's molecular weight, each fraction of the polymer containing eluent represents a sample with a narrow molecular weight distribution. This fraction is therefore treated as

though it contains polymer chains with uniform molecular weight. One type of detector used is the refractive index (RI) detector, which consists of a flow cell that is separated into two halves. One half of this flow cell is filled with pure eluent as a reference (in the samples described in this thesis THF was usually used as the eluent). The sample solution, which has a different refractive index due to the presence of the dispersed polymer, passes through the other half of the cell. The differences of the observed refractive indices between the sample and the reference cells generate a signal that is proportional to the concentration of the polymer. The molecular weight distribution would be obtained with the information of the molecular weight corresponding to the concentration of the polymer fractions. Another type of detector used for GPC analysis is a combination between a RI detector and a light scattering detector. This type of detector will be described in Section 2.1.3.

Generally, there are two ways to determine the molecular weight of an unknown polymer using GPC analysis. One commonly used method is to calibrate the system using a series of polystyrene standards which have narrow molecular weight distributions. Theoretically, the retention time of a uniform polymer sample after GPC separation is proportional to the logarithm of the molecular weight of that polymer, as shown in equation 2.2.[5]

$$\ln M = A_0 + A_1 V_R + A_2 V_R^2 + \cdots + A_n V_R^n \qquad (2.2)$$

Where M is the molecular weight of the polymer fraction, V_R is the retention volume of that fraction, and A_0 to A_n are coefficients. A calibration curve can be obtained by plotting retention times vs. ln M for a series of standards (for example polystyrene standards). Each retention time value along the calibration curve corresponds to a molecular

weight value. Using this calibration curve, the molecular weight of the unknown sample can therefore be calculated. The molecular weight distribution can then be calculated.

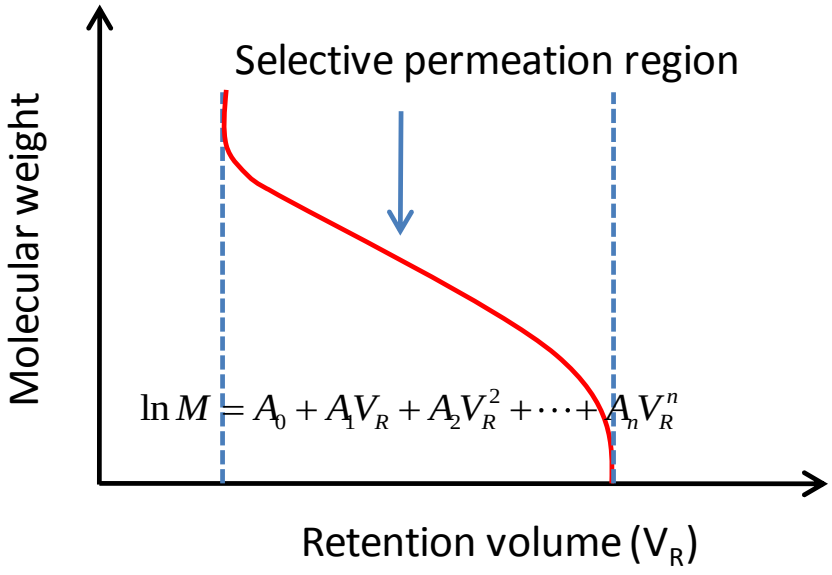

Figure 2.2. Relationship between the retention time and the molecular weight of a polymer.

2.1.3 Light scattering

When the molecular weight of a polymer is determined using a GPC calibration curve, the resulting value is not the absolute molecular weight of the sample. This value is actually the relative molecular weight compared to that of the calibration standard used. In order to obtain the absolute molecular weight of the sample, a static light scattering detector is used.

When photons of light pass through a dispersion of particles, a fraction of these photons may be scattered by the particles. This kind of scattering is in fact an elastic interaction between the photon and the particle. If the scattered photons are scattered by different parts of the same molecule, the scattered light is coherent. Meanwhile, if the photons are scattered by different molecules, the scattered light is incoherent (Figure 2.3). The addition of coherent and incoherent scattered light to the electromagnetic field leads to an observed scattering intensity. The intensity of this scattered light is proportional to the molecular weight of the sample, the concentration of the sample, and the square of the refractive index increment.[6]

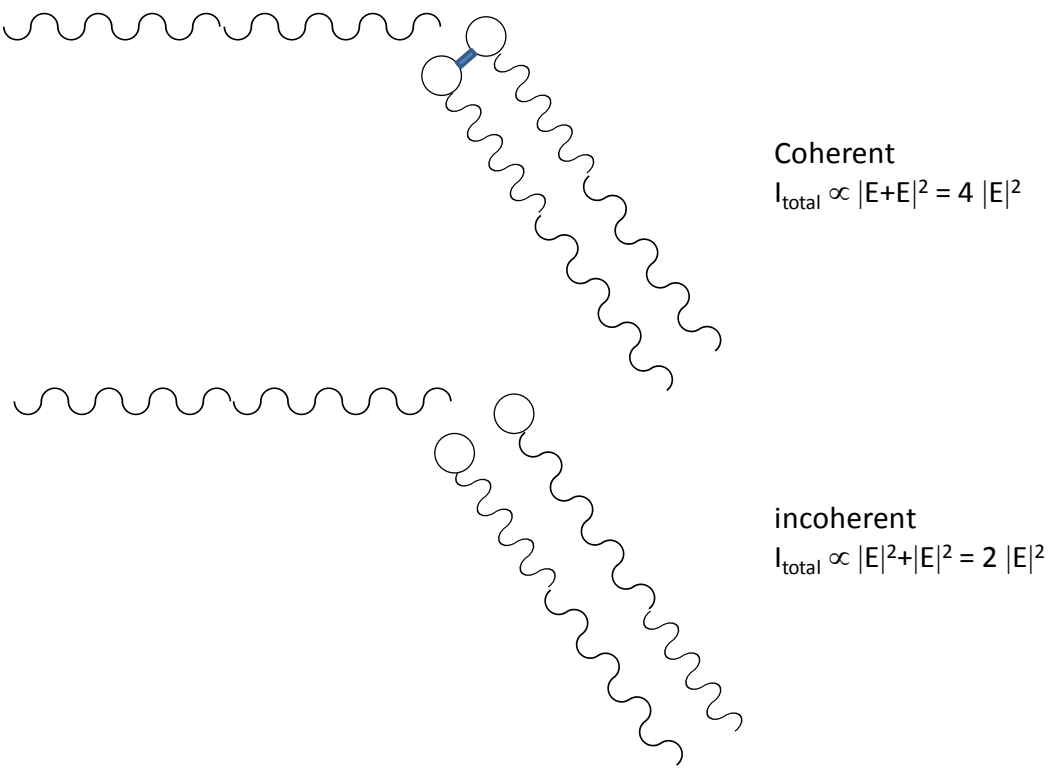

Figure 2.3. Coherent interference (above) and incoherent interference (below) of scattered light produced by particles during static light scattering.

If a polymer's hydrodynamic diameter (which is typically less than 10 nm in diameter) is much less than the wavelength of the incident light (for example, 633 nm), according to Rayleigh's theory,[7] the following equation applies:

$$\frac{KC}{\Delta R_\theta} = \frac{1}{\overline{M}_w} + 2A_2c \qquad (2.3)$$

where ΔR_θ is the Rayleigh ratio which is determined by the system, c is the concentration of the sample in g/mL, M_w is the weight-average molecular weight of the polymer, and A_2 is the second virial coefficient. K is the optical constant, which is given by:

$$K = \frac{2\pi^2 n_0^2 \left(dn/dc\right)^2}{N_A \lambda^4} \qquad (2.4)$$

Where n_0 is the refractive index of the solvent, dn/dc is the refractive index increment, N_A is Avogadro constant, and λ is the wavelength of the incident light.

If the size of the sample is larger than 10 nm, equation 2.3 is modified and becomes:

$$\frac{KC}{\Delta R_\theta} = \frac{1}{P(\theta)}\left(\frac{1}{\overline{M}_w} + 2A_2C\right) \qquad (2.5)$$

where $P(\theta)$ is a form factor characterizing the shape and size of the particles. $P(\theta)$ is given by the following equation as a function of q, which is shown below

$$P(\theta) = 1 - q^2 \frac{R_G^2}{3} \qquad (2.6)$$

$$q = \frac{4\pi n_0}{\lambda} \sin\left(\frac{\theta}{2}\right) \qquad (2.7)$$

where θ is the angle of scattered light and R_G is the radius of gyration. If it is assumed that $q^2 \frac{R_G^2}{3} << 1$, then Equation 2.5 can be derived into:

$$\frac{KC}{\Delta R_\theta} = \left(\frac{1}{\overline{M}_w} + 2A_2C \right) \left(1 + \frac{16\pi^2 n_0^2 R_G^2}{3\lambda^2} \sin^2 \frac{\theta}{2} \right) \quad (2.8)$$

If a light scattering experiment is performed at a series of angles for a series of concentrations, a plot of $Kc/\Delta R_\theta$ vs. $\sin^2(\theta/2) + kC$ can be prepared. This plot is called a Zimm plot, where the intercept of the $\theta = 0$ line is $1/M_w$, and the slope of the $C = 0$ line is related to the R_G value.[8] The M_w value determined using this method is the absolute weight-average molecular weight.

If the GPC system uses a light scattering detector together with a RI detector, both the absolute molecular weight and the molecular weight distribution can be calculated. A light scattering detector typically consists of a flow cell surrounded by 18 photodiodes, located at different scattering angles (bottom of Figure 2.4). When a sample passes through the flow cell, the scattering intensities of light at the different angles are recorded at each time point. The relative concentration of the sample at each time point is obtained by the RI detector, as explained in Section 2.1.2. Therefore, a Zimm plot can be constructed using the data from the scattering intensities at different angles and different known concentrations. The absolute weight-average molecular weight can be calculated if the refractive index increment, *dn*/*dc*, value of the sample is known.

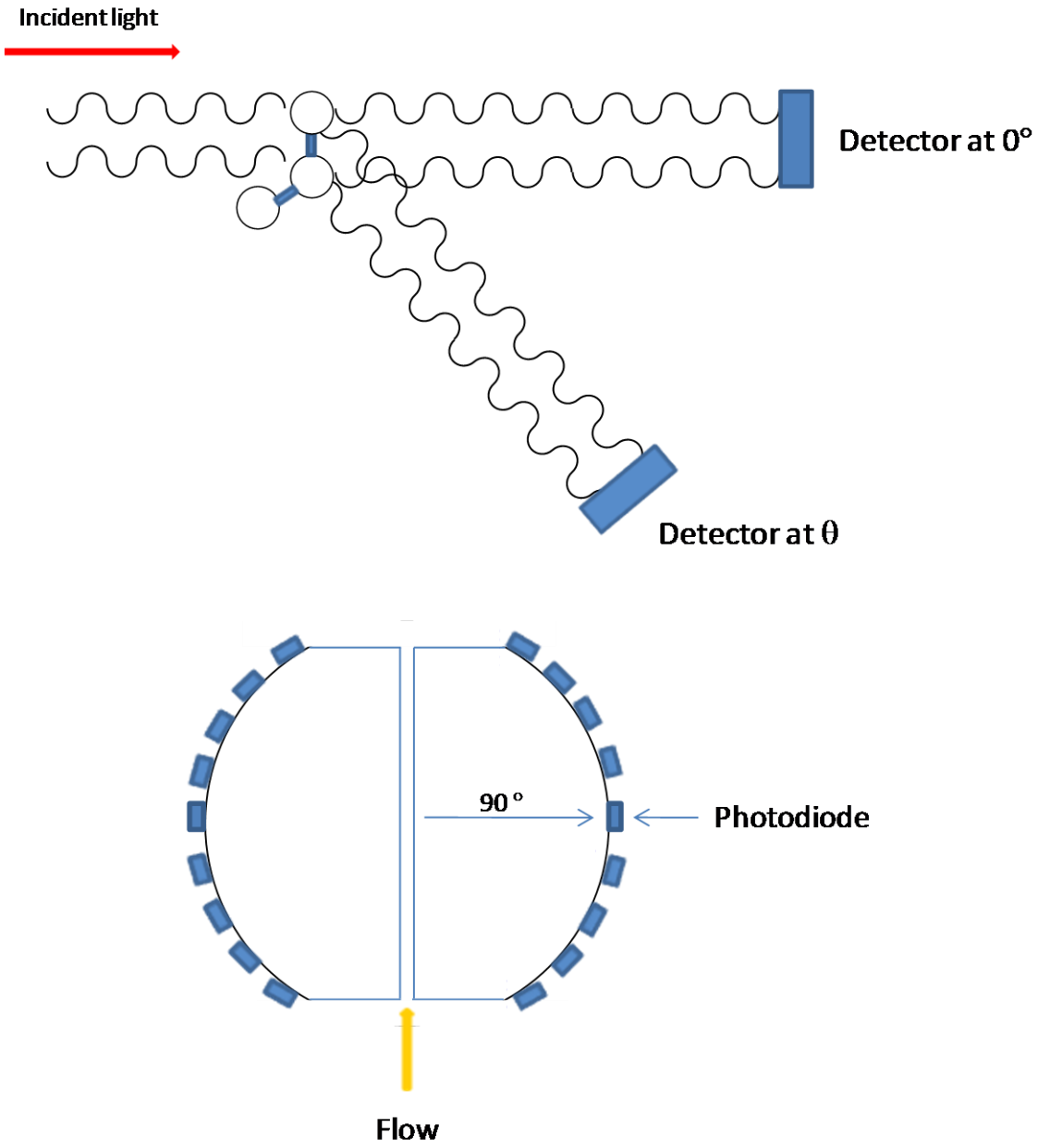

Figure 2.4. The angular dependence of the static light scattering intensity (top) and the flow cell used in the light scattering detector of a GPC system (bottom).

The *dn*/*dc* value can be obtained by a batch experiment, in which a series of sample solutions with known concentrations are passed through the flow cell of the RI detector and the refractive index can then be recorded. By plotting the concentration of the sample versus the refractive index, the *dn*/*dc* value is read as the slope of the curve.

2.2 Characterization of nanostructures

2.2.1 Transmission electron microscopy

A direct method to characterize the morphology of a nanostructure is to record its image. The resolution of an imaging technique is related to the wavelength of the light used. Theoretically, the limit of the resolution of the imaging technique is determined by the Rayleigh criterion, which postulates that the resolution is half of the wavelength used in the device.[9] Therefore, common visible light microscopy has a resolution of hundreds of nanometers. However, this level of resolution is clearly not suitable for the examination of nano devices. In order to increase the imaging resolution, it is therefore necessary to use electromagnetic radiation with very short wavelengths. An electron is a type of matter wave having a wavelength in the picometer scale. With the use of electrons as the radiation source, even though the accuracy of the electromagnetic lenses is low due to mechanical limitations, the resolution is sufficient to allow imaging on the nanometer scale.[10]

Figure 2.5 shows a diagram of a TEM instrument.[11] The electron beam is generated by an electron gun, and in our study a tungsten filament was used for this purpose. The electrons are then accelerated by an electric field (in our study this was a 75 kV field) and penetrate through an electromagnetic lens, whose function is very similar to that of the glass lenses used for adjusting a light beam. When the electrons contact the sample, some

of these electrons will be scattered or absorbed by the sample, while the rest will penetrate through the sample and reach the film, to form an image. A sample with a high electron density will scatter a greater number of electrons. Therefore, as long as the electron density of the sample is different from that of the background, the changes in the density of the transmitted electrons will be captured on film, and an image of the sample will appear. Areas of the sample with higher electron densities appear dark on the TEM image.

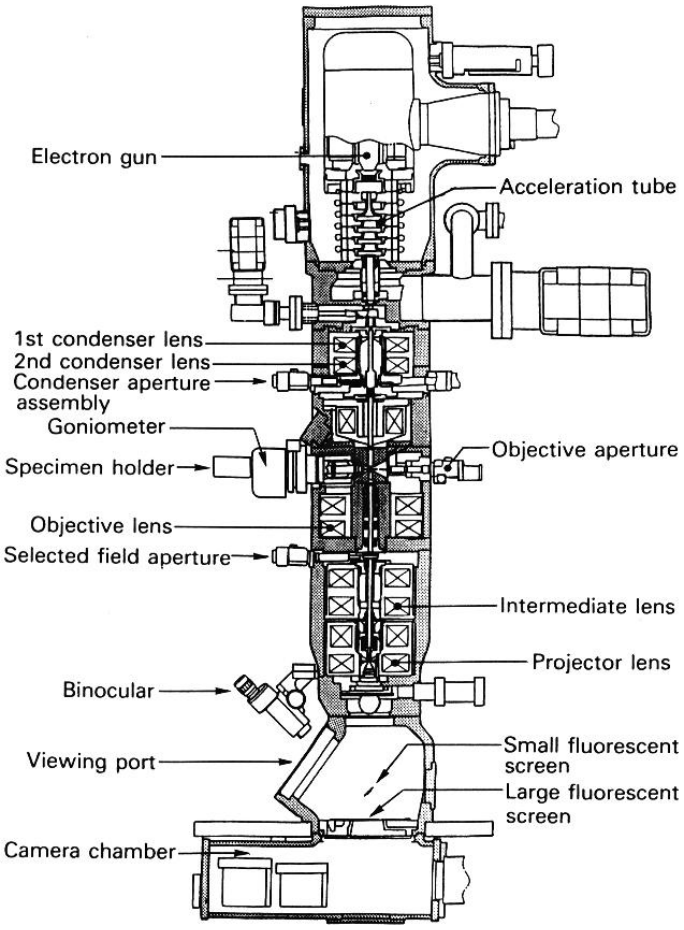

Figure 2.5. Diagram of a typical TEM instrument.[11]

Samples dispersed in a solvent can be sprayed onto copper grids covered by a carbon or nitrocellulose film. Solid samples can be embedded in a solid matrix, such as a polystyrene matrix or an epoxy resin matrix, and then cut into slices with a thickness of 50-100 nm. In order to increase the electron density of the sample, heavy metals can be used to selectively stain the sample. Polymer chains stained with metals appear as dark areas in a TEM image. For example, CEMA double bonds can be stained with OsO_4 or RuO_4.[12,13] The aromatic ring of CEMA can also be stained with RuO_4. In order to stain carboxylic groups, the COOH groups can be reacted with uranyl acetate to form a uranyl complex.[14] The selective staining of either one or of multiple functional groups on a specific polymer chain allows one to determine the conformation of the polymer chains in the nanostructure, as well as detect possible chain segregation.

2.2.2 Atomic force microscopy

AFM is a technique which provides 3-D information of the morphology of a sample. The advantages of AFM include high resolution, ultra-low forces exerted on the surface of the sample and its use on insulating materials. Depending on its intended use, researchers involved with AFM have developed different scanning modes, including contact mode, non-contact mode and tapping mode.[15-18] Originally, AFM was commonly used in the contact mode, where the tip and sample were maintained in a repulsive force regime. In the contact mode, the surface topography is obtained by graphing the change of the force exerted on the tip due to height variations of the sample as the tip moves along the surface. The drawback of this method is that the force required induces elastic deformation of polymeric and biomolecular samples, which may result in artifacts. In order to overcome

this problem, non-contact mode AFM was developed, where the tip oscillates close to the surface with an amplitude of approximately 5 nm. However, a disadvantage of this method is that if a liquid layer is present on a sample's surface, the tip is likely to become captured in that layer. Tapping mode AFM was invented to overcome the above problems. In tapping mode AFM, the tip is made to strike the surface as the cantilever oscillates. The oscillation amplitude must be sufficient to prevent the tip from becoming stuck on the surface, and an amplitude of 20 to 100 nm is typically required. A feedback system is set up to measure the perturbation of the oscillation caused by the interactions between the surface and the tip. By applying a relatively small force, the deformation of the surface is also minimized and, in principle, the resolution should improve. The instrumentation of a tapping mode AFM is illustrated in Figure 2.6.

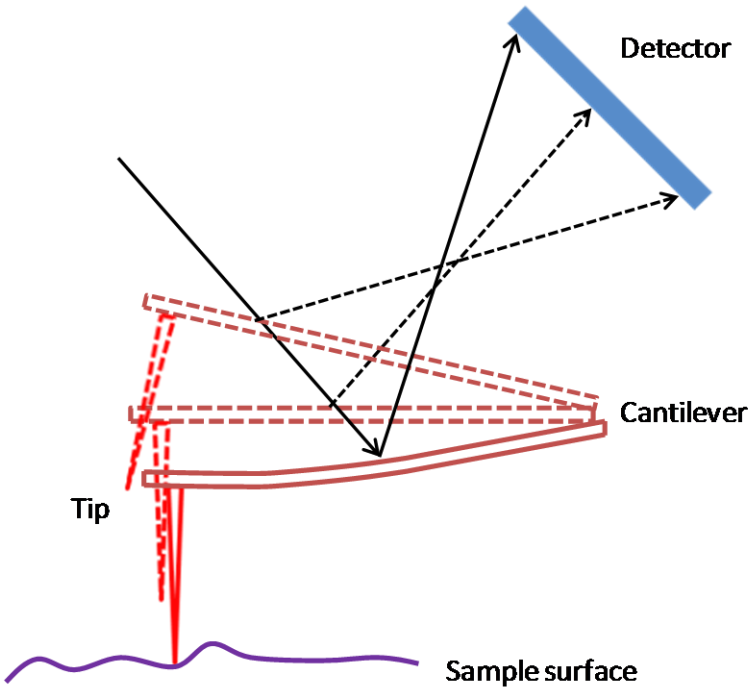

Figure 2.6. Illustration of how tapping mode AFM is analyzing a surface

Normally, by applying tapping mode AFM, a height image and a phase image of a surface can be obtained.

The oscillation of an AFM tip is defined by the equation:

$$A = A_0 Sin(\omega_0 t + \phi_0) \qquad (2.9)$$

where A_0, ω_0 and ϕ_0 represent the amplitude, frequency and phase angle of free oscillation, respectively.

During the scanning process, the equation of the oscillation changes over time, and has the form:

$$A = A_t Sin(\omega_t t + \phi_t) \qquad (2.10)$$

where A_t, ω_t and ϕ_t are the amplitude, frequency and phase angle of the oscillation at each point in time, respectively. A set-point ratio, r_{sp}, is chosen.

The feedback system will maintain the position of the piezo so that the actual oscillation amplitude will be maintained at A_{sp}, as defined by:

$$r_{sp} = A_{sp} / A_0 \qquad (2.11)$$

The actual oscillation amplitude (A_{sp}) is determined by considering the change of the height of the piezo. The topography of the surface is then determined based on this height change. This will lead to the height image of the sample.

During the oscillation, the frequency and phase angle also change. When the frequency matches that of the original frequency (ω_0), the phase angle at that point (ϕ_0), is recorded. The phase angle shift is defined as

$$\Delta\phi_0 = \phi_{0t} - \phi_0 \qquad (2.12)$$

The $\Delta\phi_0$ value for each point on the surface will be recorded. The phase image of the surface is then determined based on this phase angle shift. A phase image is useful for demonstrating chain or phase segregation between polymer domains, particularly if one polymer is more rigid than the other.

Generally, AFM images obtained in tapping mode are sensitive to the r_{sp} and A_0 values. It is recommended to use high A_0 and r_{sp} values in order to obtain images which more accurately represent the topography of a surface. When high A_0 value (45 nm) and moderate r_{sp} values (0.5) are used, the resulting phase image has an appropriate contrast which reflects the variation of stiffness that occurs along the surface of the sample.[18]

2.3 Other techniques

Dynamic light scattering is used to characterize the hydrodynamic radius (R_h) of a sample. Suppose two particles with the same hydrodynamic diameter are distributed in a solvent where photons with the same frequency and phase angle are scattered by the two particles. If the positions of the particles are fixed, the interference pattern of the photons will also

be fixed, and exhibit constructive interference. However, due to Brownian motion, the positions of the particles are constantly changing, which leads to fluctuation of the interference pattern and the intensity of the scattered light. This fluctuation can be analyzed by an auto-correlation function. This auto-correlation function reveals the mobility or diffusion coefficient (D) of the particles. The relationship between the diffusion coefficient of a particle and its hydrodynamic radius (R_h) is given by the Einstein-Stokes equation: [19]

$$R_h = \frac{k_B T}{6\pi\eta D} \text{ or } D = \frac{k_B T}{6\pi\eta R_h} \qquad (2.13)$$

where η is the viscosity of the solvent, k_B is Boltzmann's constant and T is the temperature of the solvent in Kelvin. Thus, the hydrodynamic diameter of a sample can be calculated. The polydispersity index (PDI) of the hydrodynamic diameter can also be obtained. The relative standard deviation of the hydrodynamic diameter is the square root of the value of the PDI.

Ultra-violet and visible spectra or UV-vis spectra can be used to quantitatively characterize functional groups which have absorbance in the UV-vis range (190 nm to 900 nm). According to the Beer-Lambert law, the absorbance (Abs) of a sample is proportional to its concentration.[20] This relationship is shown in the following equation:

$$Abs = \varepsilon\, c\, l \qquad (2.14)$$

where ε is the molar absorbtivity or extinction coefficient, *c* is the concentration of the sample and *l* is the pathlength of the light. In this thesis, the double bond of CEMA was analyzed by UV-vis spectroscopy.

Thermogravimetric analysis (TGA) is used to monitor the weight loss of a sample during thermal decomposition. The polymer sample or nanostructure is placed in a thermo-balance and heated from room temperature up to 800 °C. The weight of the sample is monitored continuously. The polymer decomposes when the temperature reaches its thermal decomposition temperature. The weight loss of the sample is recorded as a function of temperature.

References

1. Bovey, F. A.; Mirau, P. A. *NMR of Polymers* Academic Press, San Diego, 1996.

2. Fawcett, A. H. *Polymer Spectroscopy* Wiley, Chichester England, 1996.

3. Staurt, B. H. *Polymer Analysis* Wiley, Chichester, 2002.

4. Koenig, J. L. *Spectroscopy of Polymers 2nd Ed.* Elsevier, Amsterdam, New York, 1999.

5. Wu, C.-S. Ed. *Handbook of Size Exclusion Chromatography and Related Techniques* Marcel Dekker Inc. New York, 2004.

6. Schartl, W. Light *Scattering from Polymer Solution and Nanoparticle Dispersions* Springer-Verlag, Berlin, 2007.

7. Kratochvil, P. *Classical Light Scattering from Polymer Solutions* Elsevier, Amsterdam, 1987.

8. Zimm, B. H. *J. Chem. Phys.* **1948**, *16*, 1099.

9. Born, M. & Wolf, E. *Principles of Optics* Cambridge Univ. Press, Cambridge, U.K. 1999.

10. Williams, D. B.; Carter, C. B. *Transmission Electron Microscopy: A Textbook for Materials Science* Plenum Publishing, New York, 1996.

11. Flutz, B.; Howe, J. *Transmission Electron Microscopy and Diffractometry of Materials* Springer, Berlin, 2008.

12. Hu, J.; Liu, G.; Njikang, G. *J. Am. Chem. Soc.* **2008**, *130*, 3236.

13. Dupont, J.; Liu, G.; Nihara, K.; Kimoto, R.; Jinnai, H. *Angew. Chem. Int. Ed.* **2009**, *121*, 6260.

14. Zhou, Z.; Liu, G.; Han, D. *ACS Nano* **2009**, *3*, 165.

15. Magonov, S. N.; Whangbo, M.-H. *Surface Analysis with STM and AFM*; VCH: Weinheim, 1996.

16. Chowdhury, S.; Laugier, M. T. *Nanotechnology* **2004**, *15*, 1017.

17. Bar, G.; Thomann, Y.; Brandsch, R.; Cantow, H.-J.; Whangbo, M.-H. *Langmuir* **1997**, *13*, 3807.

18. Wang, J.; Horton, J. H.; Liu, G.; Lee, S.; Shea, K. J. *Polymer* **2007**, *48*, 4123.

19. Kuhn, H.; Forsterling, H.; Waldeck, D. H. *Principles of Physical Chemistry* J. Wiley & Sons. Inc. Hoboken, New Jersey, 2009.

20. Fifield, F. W. *Principles and practice of Analytical Chemistry* International Text Co. London, 1983.

Chapter 3

Morphology and swelling of poly(glyceryl methacrylate)-*block*-poly(2-cinnamoyloxyethyl methacrylate)-*block*-poly(*tert*-butyl acrylate) aggregates in water

3.1 Introduction

Poly(glyceryl methacrylate)-*block*-poly(2-cinnamoyloxyethyl methacrylate)-*block*-poly(*tert*-butyl acrylate) (PGMA-*b*-PCEMA-*b*-P*t*BA) is an interesting polymer (structure is shown below and in Figure 1.1), as the PGMA block is water soluble, the PCEMA block is photo-crosslinkable, and the P*t*BA block can be readily hydrolysed. For example, these triblock copolymers ($PGMA_{300}$-*b*-$PCEMA_{120}$-*b*-$PtBA_{100}$) have been used to produce cylindrical nanoaggregates in water with PGMA as the corona, PCEMA as the shell, and P*t*BA as the core.[1] The PCEMA shell of the cylindrical aggregates was then photo-crosslinked to yield structurally-stable nanofibers. The P*t*BA block of the nanofibers can be hydrolyzed to yield water-dispersible nanotubes with PAA-lined cores. The nanotubes can be further coupled with hydrophobic nanotubes in order to yield amphiphilic nanotube multiblocks that can form supermicelles by self-assembly.[1] Also the

hydrophilic core of the nanotubes can be used as host for inorganic nanoparticles, such as the catalytic Pd particles.[2] The electroless catalytic deposition of Ni on such Pd nanoparticles has, for example, allowed us to produce water-dispersible polymer/Pd/Ni superparamagnetic hybrid nanofibers[2] with potential applications in immunoassays. Cylindrical nanoaggregates of this polymer can also be obtained in block selective solvents, such as water. Hu *et al.* reported that these cylindrical nanoaggregates underwent a morphological change to twisted cylinders when water was replaced with methanol by dialysis.[3] Moreover Zheng *et al* reported the preparation of vesicles with this copolymer in a mixture of methanol and decahydronaphthalene (DN).[4] While cylindrical nanoaggregate formation from PGMA-*b*-PCEMA-*b*-P*t*BA has been exploited by our group for the preparation of exciting and interesting nanomaterials,[1-4] a systematic study of factors governing the morphologies and the morphological transitions of nanoaggregates formed from triblock copolymers was lacking. In this chapter, we report our results from such a systematic study. We also report our accidental discovery that cylindrical nanoaggregates of a PGMA-*b*-PCEMA-*b*-P*t*BA sample in water could be swollen by decahydronaphalene (DN), a selective solvent for only the P*t*BA block, to yield nanotubes and vesicles. This morphological change was dependent on the preparation protocol of the cylindrical nanoaggregates. The core diameters of these nanotubes could be tuned by adjusting the DN swelling time, and a three-fold increase of their diameters could be observed, compared to those which were not swollen by DN.

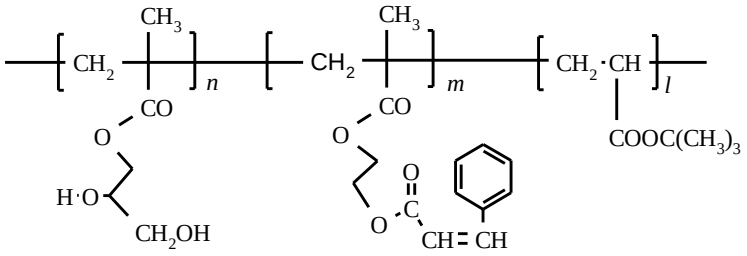

PGMA-PCEMA-P*t*BA

3.2 Experimental

PGMA-*b*-PCEMA-*b*-PtBA Samples. The three PGMA-*b*-PCEMA-*b*-P*t*BA samples used in this study were derived from PSMA-*b*-PCEMA-*b*-P*t*BA, where PSMA denotes poly(solketal methacrylate). The procedure for the preparation of PSMA-*b*-PCEMA-*b*-P*t*BA has been described before [3] and is therefore not repeated here. In order to hydrolyze the PSMA block of $PSMA_{300}$-*b*-$PCEMA_{120}$-*b*-$PtBA_{100}$, 10 mg of the triblock copolymer was dissolved in 2 mL of THF. To the solution was then added 0.5 mL of 6.0 M aqueous HCl. The resultant mixture was stirred for 2 h before it was transferred into a dialysis tube, with a cut-off molecular weight of 12000-14000 (Spectra/Por®, supplied by VWR) and dialyzed against methanol, which was changed 6 times over 2 days. The final methanol solution in 0.5 mL was added into 5 mL of diethyl ether (supplied by Fisher Scientific, ACS grade > 99.0 %) in order to precipitate the polymer. The precipitate was collected by centrifugation at 1550 *g* for 5 min. Other triblocks were prepared in a similar way.

Aggregate Formation. After the diethyl ether supernatant was removed from the triblock copolymer precipitates described above, 15 mL of deionized water was immediately added. This yielded a suspension at ~0.5 mg/mL (or 25 mg/mL for the swelling experiment). All the aggregates analyzed in this study had been stirred for a minimum of two days, either at room temperature, or at elevated temperatures (85 or 100 °C) under the protection of nitrogen. The estimated yields of these aggregates were approximately 80%.

Swelling of Cylindrical Aggregates. To each vial was added 1.0 mL of decahydronaphthalene (DN), 5.0 mL of deionized water, and 200 μL of $PGMA_{300}$-*b*-$PCEMA_{100}$-*b*-P*t*BA_{100} cylindrical aggregates at concentrations of 25 mg/mL. The heterogeneous mixtures were stirred in different Pyrex® vials at room temperature for 1 to 3 days for nanoaggregate swelling in water by DN.

TEM Imaging of the Aggregates. Morphologies of the aggregates were analyzed by transmission electron microscopy (TEM) using a Hitachi H-7000 instrument operated at 75 kV. The specimens were prepared by aspirating nanoaggregate solutions onto a carbon-coated copper grid. In order to stain the CEMA groups, the grid was equilibrated in OsO_4 vapor for one hour.

In order to stain the *t*BA units of the swollen nanotubes, it was necessary to crosslink the PCEMA layer first, and then hydrolyze the *t*BA groups. PCEMA crosslinking was achieved by photolyzing the nanoaggregates in water/DN for two hours by a focused UV beam from a 500-W mercury lamp. The crosslinked aggregates were then dialyzed against methanol, which was changed six times during two days to remove DN and water. The crosslinked aggregates in methanol were added into diethyl ether in order to precipitate the aggregates. The precipitate was dispersed in a mixture of dichloromethane and trifluoroacetic acid at v/v = 75/25 in the presence of 3 molar equivalents of triethyl silane relative to the *t*BA units. The mixture was stirred for 1.5 h before it was added into diethyl ether in order to precipitate the hydrolyzed aggregates. After redispersing the sample in methanol, the aggregates were aspirated onto a carbon-coated copper grid. One drop of 0.1 % uranyl acetate aqueous solution was also added onto the grid. After 30 min, the water was sucked away by a filter paper and the grid was rinsed by methanol droplets 10 times.

3.3 Results and Discussion

3.3.1 Polymer Characterization

Three PGMA-*b*-PCEMA-*b*-P*t*BA samples, Polymers 1, 2, and 3, were used in this study. These samples were derived from the hydrolysis of their PSMA-*b*-PCEMA-*b*-P*t*BA precursor samples, Polymers 1S, 2S, and 3S whose characteristics are provided in Table 3.1.

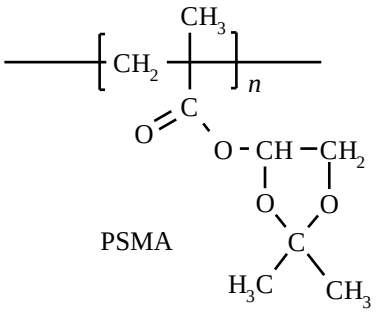

PSMA

The polymers were characterized in the PSMA-*b*-PCEMA-*b*-P*t*BA form for the analogous solubility of PSMA, PCEMA, and P*t*BA. All of the three blocks of PSMA-*b*-PCEMA-*b*-P*t*BA were soluble in solvents such as butanone, tetrahydrofuran (THF), chloroform, and *N*,*N*-dimethylforamide (DMF). Meanwhile, PGMA dissolved only in polar solvents such as water, methanol, pyridine, and DMF. The specific refractive index increment dn_r/dc and light scattering (LS) weight-average molar mass M_w were determined in butanone. Butanone was chosen because it had the lowest refractive index among solvents such as butanone, THF, chloroform, and DMF, and its use afforded sufficiently large dn_r/dc values to reduce measurement errors in both dn_r/dc and M_w. The size-exclusion chromatography (SEC) polydispersity indices M_w/M_n were determined in DMF based on polystyrene standards, and the number of repeat unit ratios $n/m/l$ was determined by comparing the intensities of characteristic peaks of the three blocks from ^{1}H NMR spectra measured in $CDCl_3$.

Table 3.1. Characteristics of PSMA-*b*-PCEMA-*b*-P*t*BA copolymers used

Sample	dn_r/dc (mL/g)	LS $10^{-5} \times M_w$ (g/mol)	SEC M_w/M_n	NMR $n/m/l$	n	m	l
Polymer 1S	0.108	1.22	1.15	1.00/0.48/0.30	290	140	88
Polymer 2S	0.100	1.22	1.03	1.00/0.33/0.32	380	123	119
Polymer 3S	0.0785	1.37	1.18	1.00/0.28/0.31	440	125	135

The data in Table 3.1 shows that all three copolymers had PCEMA and PtBA blocks of similar lengths, and they differed mainly in the lengths of their PSMA blocks (or their PGMA blocks after PSMA hydrolysis). After the PSGMA blocks were converted to PGMA blocks, the weight fractions of PGMA in Polymers 1, 2, and 3 are 54, 56, and 59%, respectively. The data also show that dn_r/dc values decreased as the PSMA length increased.

3.3.2 Morphology of the nanoaggregates

Effect of Copolymer Composition Variation. Nanoaggregates could be prepared by directly stirring PGMA-*b*-PCEMA-*b*-P*t*BA, which was freshly precipitated from diethyl ether, in water. After 5 days, the samples were centrifuged at 1550 *g* for 5 min in order to

remove large aggregates or components that did not dissolve. Our gravimetric analysis indicated that more than 80 wt% of the triblock copolymers became dispersed in the supernatant after this treatment. Figure 3.1 compares TEM images of nanoaggregates of the three triblocks which were aspirated from water and stained by OsO_4.[5] As the weight fraction of PGMA increased from 49 (for Polymer 1), to 56 (for Polymer 2), and to 59% (for Polymer 3), the morphlogis of the nanoaggregates changed from branched cylinders, to a mixture of cylinders and spheres, and then to spheres.

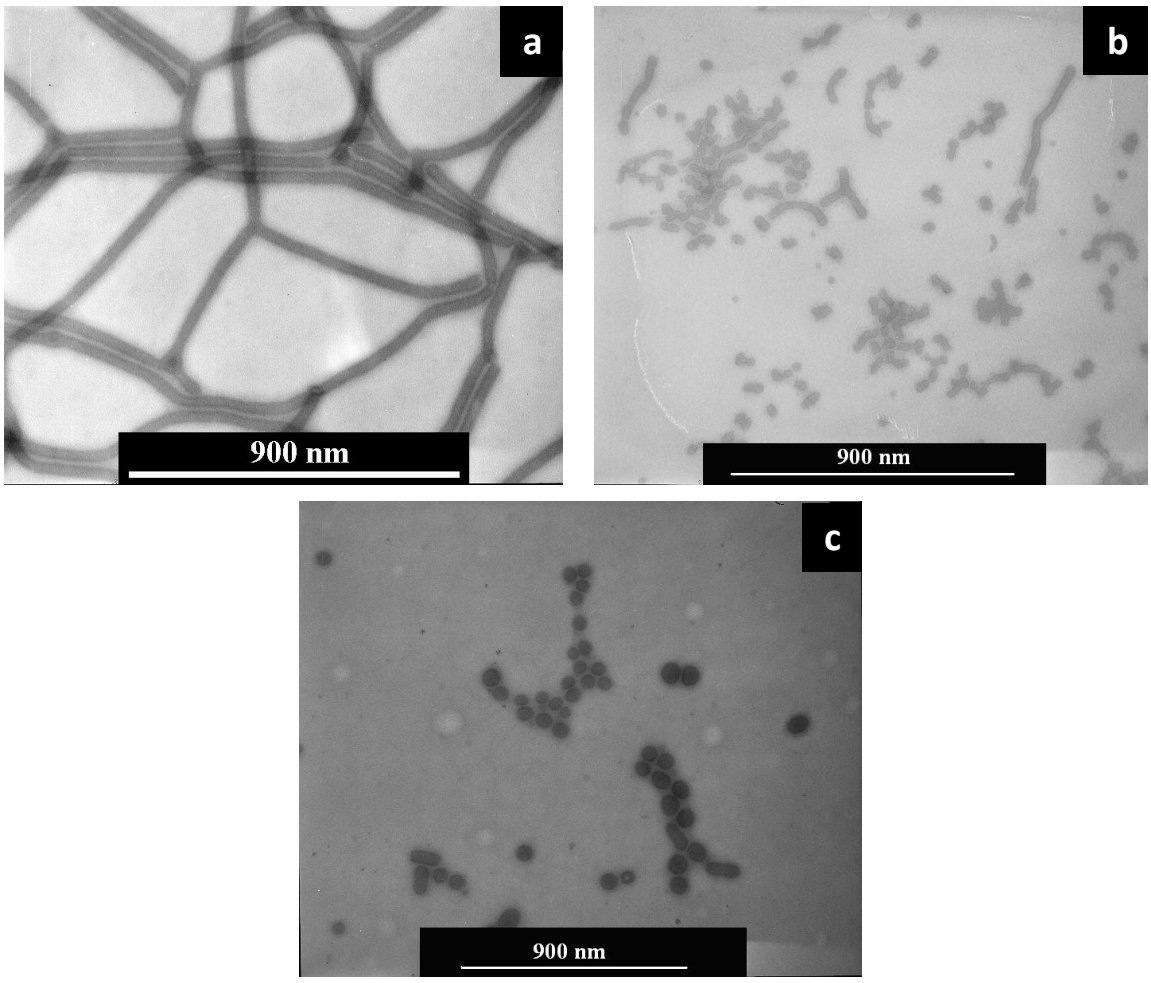

Figure 3.1. TEM images of nanoaggregates formed from Polymers 1 (a), 2 (b), and 3 (c) after stirring for 5 days in water. The samples were stained by OsO_4 vapor before analysis.

This morphological variation with the weight fraction of the soluble block is in agreement with many prior experimental observations.[6-8] Despite this, one should be cautioned that the aggregates observed are not necessarily the equilibrium structures in water for several reasons. First, the glass transition temperatures T_g of PCEMA and P*t*BA are rather high, at 69 and 73 ^{o}C, respectively.[9] At room temperature in water, these two blocks lack the dynamic mobility required to achieve their equilibrium segregation morphologies. Secondly, we have attempted the preparation of nanoaggregates in water by different pathways, and found that the morphology of the final nanoaggregates obtained depended on the preparation pathway. We have, for example, attempted to form nanoaggregates of Polymer 2 in water by dissolving the triblock in pyridine first. We then added water up to a volume fraction of 95% before the sample was dialyzed against water in order to remove pyridine. Using this procedure, we produced exclusively spherical aggregates from Polymer 2.

Nanoaggregates formed by block copolymers in block selective solvents are strongly affected by the preparation methods.[10] In most cases kinetic products are obtained when the polymer chains are in contact with the selective solvent in which they are not soluble. In this case, the polymer chains lose mobility. This leads to the freezing of the polymer chains.

Effect of Thermal Annealing. Annealing the nanoaggregates above the T_g values of PCEMA and P*t*BA should increase the chain mobility of these polymers, and lead to the

eventual formation of the equilibrium morphologies of the nanoaggregates or micelles. Figure 3.2 compares TEM images of nanoaggregates that we prepared in water at room temperature after their annealing at 85 ^{o}C for 1 and 3 days, or after annealing at 100 ^{o}C for 1 d. After annealing at 85 ^{o}C for 1 d, the branched cylinders shown in Figure 3.1 (a) have become shorter. Only straight cylinders and spherical aggregates are visible in Figure 3.2 (b) after sample annealing at 85 ^{o}C for 3 days. This suggests that the thermodynamically favored morphology of the nanoaggregates at 85 ^{o}C may be spheres or a mixture of spheres and straight cylinders. Annealing at 100 ^{o}C for 1 day yielded also a mixture of spheres and cylinders (Figure 3.2 (c)), a situation analogous to that after sample annealing at 85 °C for 3 days. This is in agreement with the increased mobility of chains at 100 ^{o}C than at 85 ^{o}C.

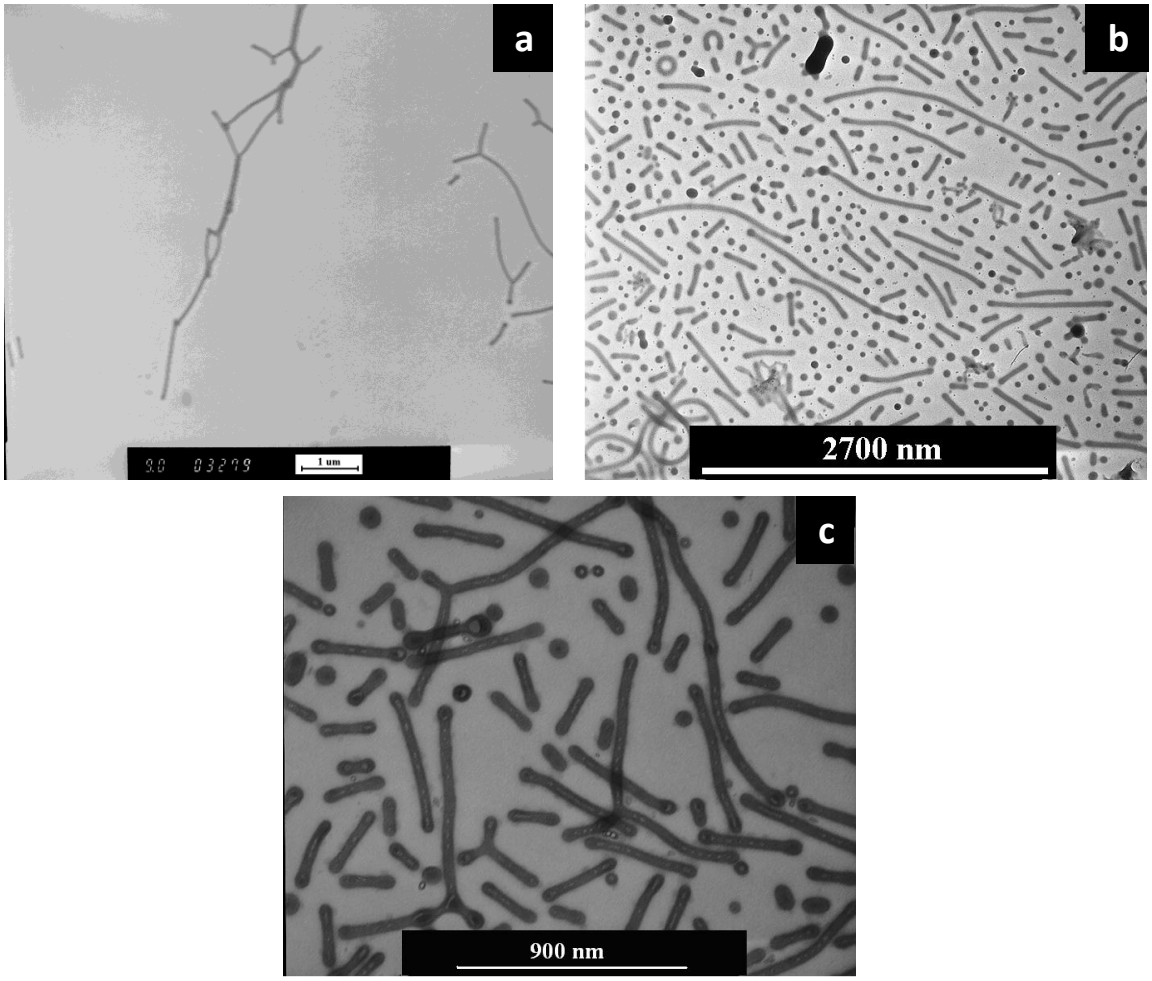

Figure 3.2. TEM images of aggregates of Polymer 1 prepared at room temperature after their annealing at 85 ^{o}C for one day (a), three days (b), or after annealing at 100 ^{o}C for one day (c).

Nanoaggregates of Polymers 2 and 3 prepared at room temperature were annealed at 85 ^{o}C for one day. In contrast manner to the nanoaggregates of Polymer 1, the nanoaggregates of Polymers 2 and 3 did not undergo noticeable morphological transitions under these conditions.

Effect of Sample Annealing in the Presence of THF. THF is a good solvent for both PCEMA and P*t*BA chains. The addition of THF decreases the T_g of the PCEMA and P*t*BA chains, and therefore introduces mobility to the polymer chains. We annealed the nanoaggregates in the presence of 1 % (v/v) THF at 95 °C for one day. The TEM images of the nanoaggregates are shown in Figure 3.3. The aggregates formed by Polymer 1 are transformed into a mixture of spheres and short rods after THF has been added, while at room temperature it forms branched cylindrical aggregates. The morphology of the aggregates formed by Polymer 2 become totally spherical in the presence of THF, while in water the aggregates show a mixture of spheres and cylinders. The aggregates formed by Polymer 3 in the presence of THF are spherical, which are similar to those formed in water.

As discussed in the previous section, the hydrodynamically favored morphology of aggregates formed by Polymer 1 at 85 °C is a mixture of spheres and short cylinders. The polymer chains in this aggregate should obtain greater mobility when they are annealed at a higher temperature (95 °C). However, after thermo-annealing at 100 °C, their aggregates still retained a portion of cylinders within their mixture. The length of the cylindrical aggregates was not less than 500 nm. The almost complete transformation of the morphology from cylinders to spheres shown in Figure 3.3 (a) should therefore be the attributed to the addition of THF. THF is miscible with water. The small THF molecules become uniformly distributed in the water phase, so that they could pass through the PGMA corona chains and come into contact with the PCEMA layer. Since PCEMA is soluble in THF, the THF molecules may diffuse into the PCEMA phase, and

subsequently come into contact with the P*t*BA core phase. Therefore, some of the THF solvent molecules may migrate into the PCEMA and P*t*BA phases. The T_g of a polymer chain should decrease if the polymer interacts with a good solvent. In this case, the T_g of PCEMA and P*t*BA decreased. In other words, the polymer chains acquired sufficient mobility to yield the hydrodynamic states which have spherical morphologies. Similarly, the spherical morphology formed by Polymer 2 in the presence of THF should be considered as the thermodynamically favored morphology.

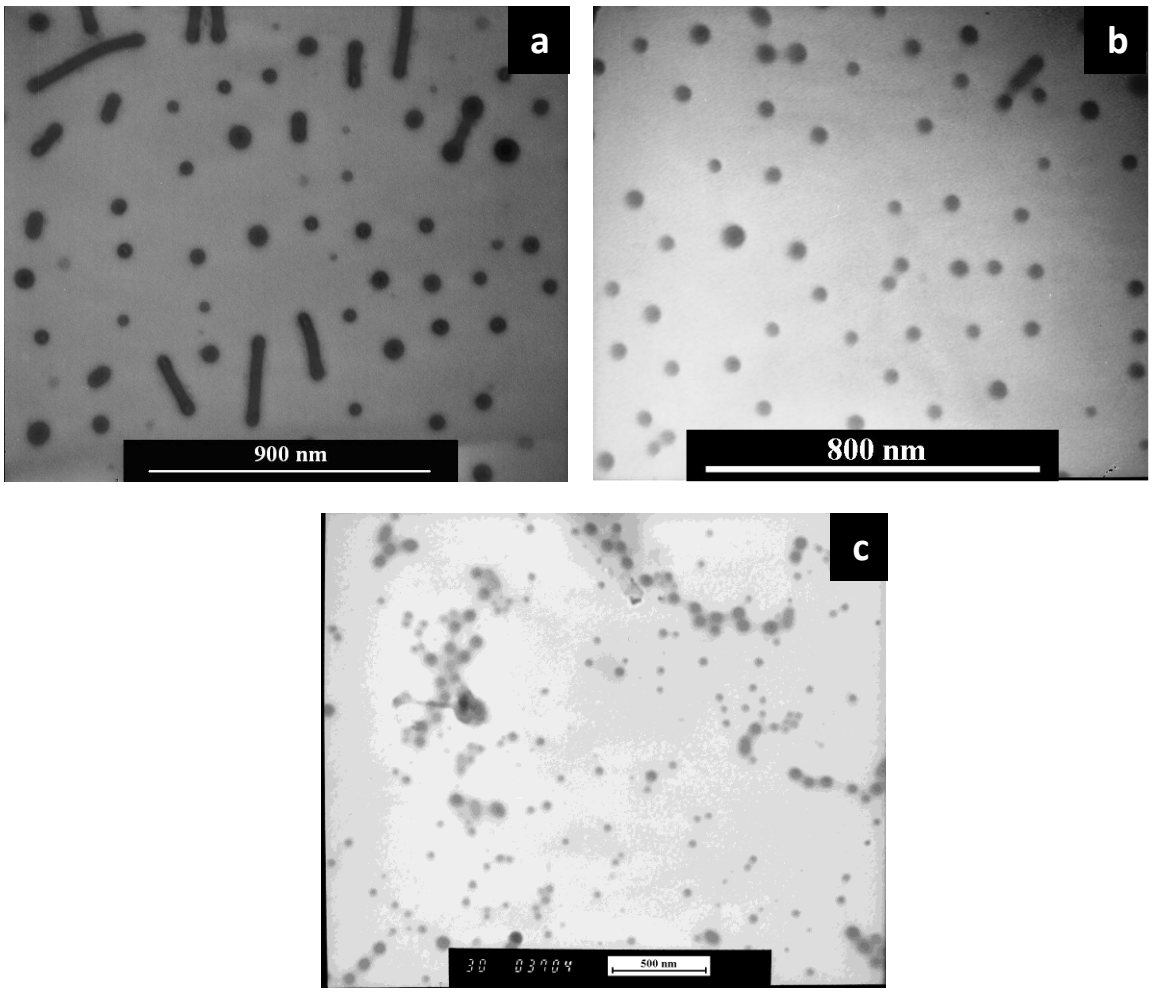

Figure 3.3. TEM images of nanoaggregates of (a) Polymers 1, (b) 2, and (c) 3 after they were annealed at 95 ^{o}C in the presence of 1 vol% of THF in water.

The Swelling of Cylindrical Nanoaggregates of Polymer 1 in DN. The hydrolysis of the P*t*BA core of the cylindrical aggregates formed by Polymer 1 will lead to the formation of a cavity in the cylinder. The hydrolysis of P*t*BA yields carboxylic acid groups of the PAA chain. A cavity bearing these functional groups has many potential applications, such as acting as a template for the synthesis of nanoparticles.[2,11] In such an application, the total number of incorporated nanoparticles is related to the volume of the cavity. As mentioned in the previous section, the PCEMA and P*t*BA domains could absorb THF in order to obtain chain mobility. If a solvent that is good for P*t*BA only is selected, and is mixed with a dispersion of the cylindrical aggregates, the solvent should diffuse into the P*t*BA core, and subsequently the volume of the core phase will expand. After the hydrolysis reaction, the volume of the cavity should increase accordingly.

Decahydronaphthlene (DN) was chosen as the solvent for the swelling of P*t*BA. The solubility tests showed that PGMA and PCEMA are not soluble in DN, while P*t*BA is soluble in this solvent. We first prepared a batch of cylindrical aggregates of Polymer 1 at room temperature. Water and DN were mixed at a ratio of 5 to 1. Under vigorous stirring, the cylindrical aggregates were added into the solvent mixture dropwise. The mixture was then stirred for 3 days. The TEM image of the obtained sample is shown in Figure 3.4 (b). Despite our expectation, the cylindrical aggregates were broken into vesicle-like morphologies, rather than becoming swellon. The sample was stained with OsO_4, so that the PCEMA domain appears dark in the image. The products bear light cores. According to the label in the image, the diameter of the core phase is approximately 50 nm. This value is much greater than the extended length of P*t*BA

chains. Thus, the cores of the obtained spherical product are most likely hollow. The preparation of vesicles of the same polymer was reported elsewhere by Zheng *et al.*, using a different procedure.[4]

3.3.3 The swelling of cylindrical aggregates using water/DN mixtures

We then prepared a sample by mixing the cylindrical aggregates with water/DN for only one day. In the TEM image of this sample, the body of the cylindrical aggregates is not uniform in width after being exposed to DN for this length of time. Some parts of the cylinder are swelling more quickly than other parts, and generating bumpiness. This change in the morphology should be attributed to the presence of DN, since we did not observe this morphology with the water dispersions of the aggregates even after a few weeks of incubation. This swelling should be driven by the expansion of the P*t*BA domain, which uptakes DN. Even though DN is not miscible with water, it still has some solubility in water. The DN molecules that dissolve in water are able to penetrate through the PGMA and PCEMA domains, and reach the P*t*BA core. However, from the TEM image, the diffusion rate of DN along the body of the cylinder is not uniform. Obviously, the uptake of DN is faster at the ends of the cylinder so that diameters of the termini of the cylinder are greater than the diameter of the body. This is reasonable, since the ends of the cylinder have greater surface areas than the body does. Therefore, even though the diffusion rate of DN per specific surface area is uniform, the amount of DN diffused into the core phase is faster at the ends of the cylinder than along the body. However, the DN appears to have diffused into the core phase at a non-uniform rate along the body of the cylinder. We will explain this behaviour in the following section.

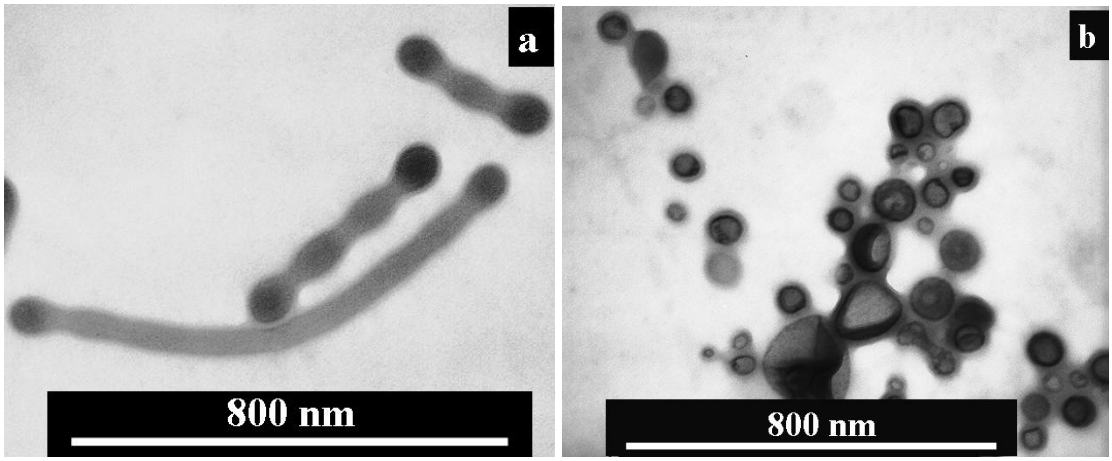

Figure 3.4. TEM images of cylindrical nanoaggregates of Polymer 1 prepared at room temperature and equilibrated in water/DN for one day (a) and three days (b), respectively.

Another batch of cylindrical aggregates was annealed for one day at 85 °C before it was mixed with a water/DN mixture. From Figure 3.2 (a), it is apparent that the morphologies of the cylindrical aggregates do not change significantly after the annealing process. After adding this sample into the mixture of water/DN, and incubating the mixture for three days, we then crosslinked the sample by exposing it to UV light. The P*t*BA core was then hydrolyzed into PAA. The TEM images (Figure 3.5) were obtained by staining the PAA chains with uranyl acetate. From the TEM image, the core of the cylinder appears as a light channel-like domain, which is covered by a dark coating, which represents the PAA chains. It can be seen that the core phase has expanded, while the cylindrical morphology remained. In this case, the DN diffused into the P*t*BA core in a much more uniform manner than was observed with the non-annealed sample.

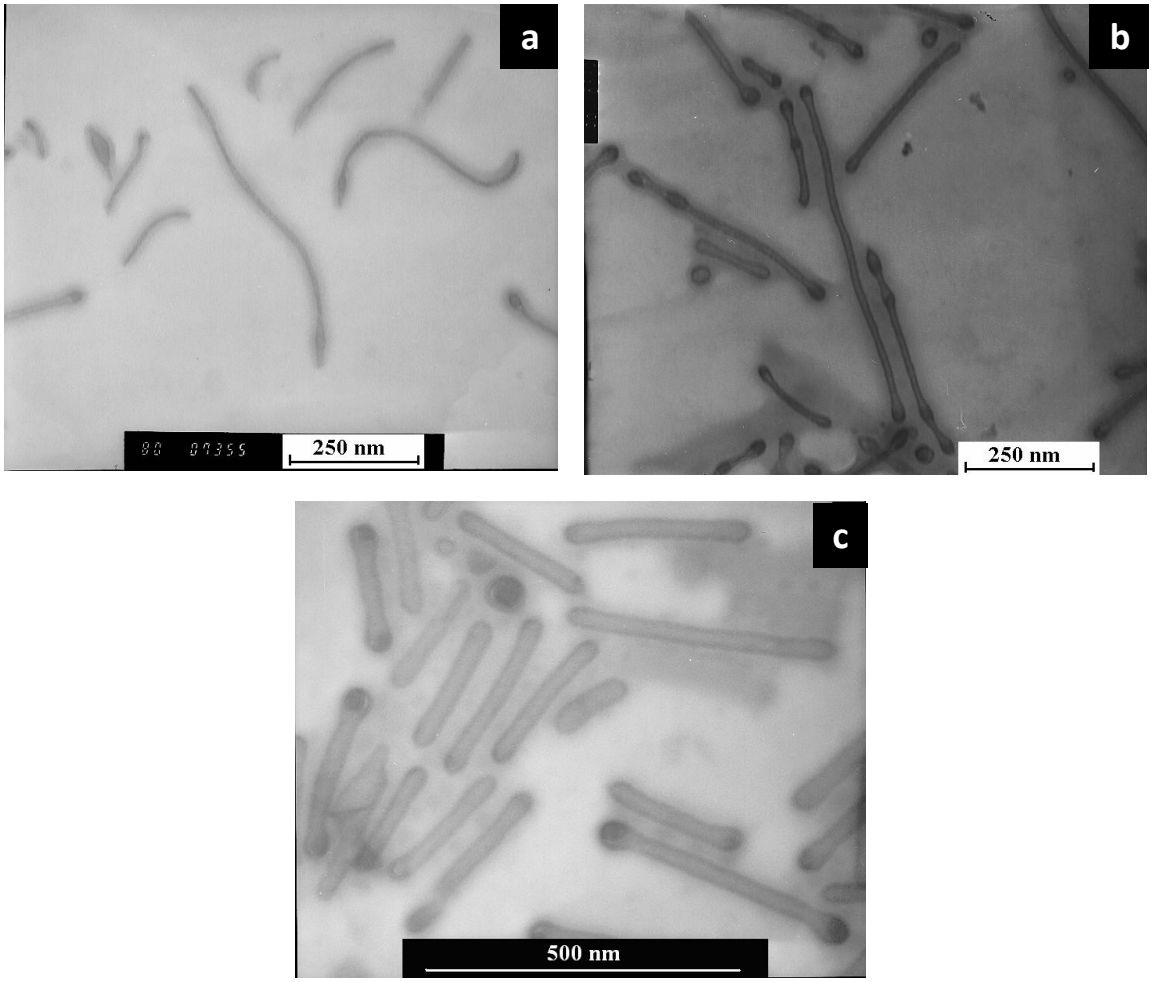

Figure 3.5. TEM images of cylindrical nanoaggregates that were prepared at room temperature and annealed at 75 ^{o}C for five days after equilibration in water/DN for 0 days (a), one day (b), and three days (c), respectively. The specimens were stained by uranyl acetate.

We also studied the kinetics of the swelling process. The TEM image of the aggregates after 3 days of swelling is shown in Figure 3.5. By measuring the diameters of the light channels, we were able to plot these diameters against the swelling time, as shown in Figure 3.6. As the swelling time increased, the diameter of the core phase increased also. The extent of swelling can therefore be adjusted by varying the swelling time. With this technique, we can tune the size in the channel in a controllable way. If the carboxyl

groups in the channel are used to synthesize nanocrystals, the weight fraction and the size of the crystals may be tunable as well.

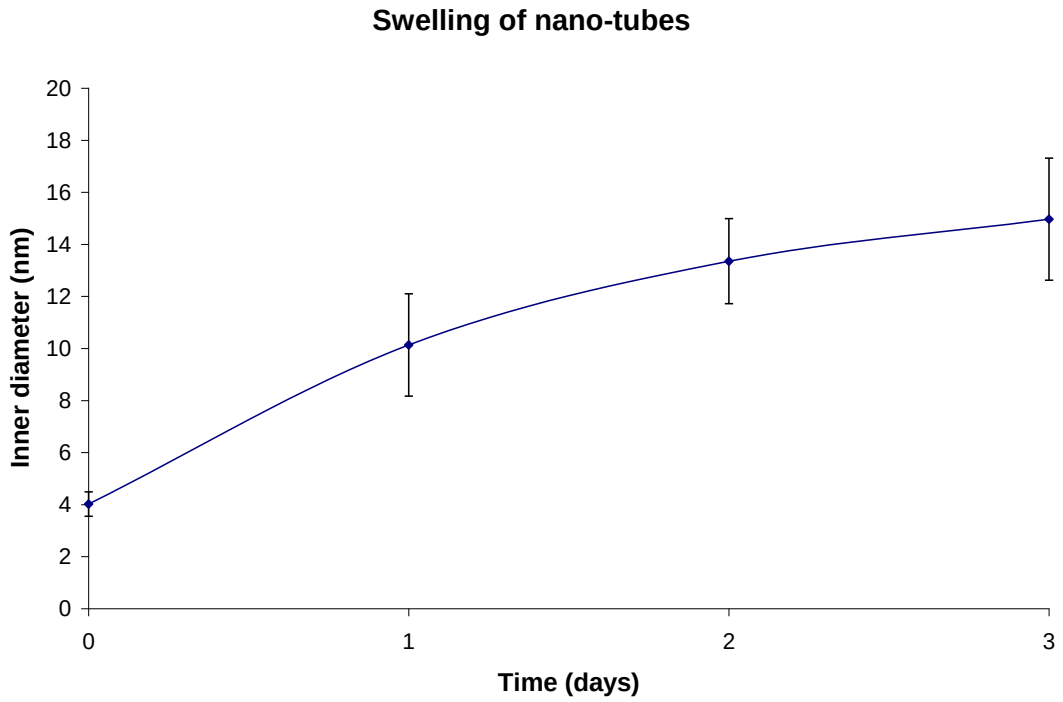

Figure 3.6. Plot of the increase of the PAA core diameter as a function of cylindrical nanoaggregate swelling time by DN.

A possible explanation of this uniform swelling behaviour is based on the role of the P*t*BA chains. Since P*t*BA and PCEMA are not soluble in water, initially when the polymer was mixed with water, the mobility of those polymer chains was restricted, or even frozen. This could lead to incomplete phase segregation between the three blocks, as shown in Figure 3.4. There may be some small P*t*BA domains which are non-uniformly distributed in the PCEMA layer, as shown in Figure 3.7. When DN passes through the PCEMA layer, these P*t*BA defects may uptake DN. The uptake of DN

therefore occurs more rapidly at the regions of the P*t*BA domain that are near these defects, than other parts of the P*t*BA core domain. Therefore, non-uniform swelling occurs. Finally, the non-uniform expansion of the core phase leads to the breakdownof the cylinders.

However, the P*t*BA and PCEMA chains obtained some mobility during the thermo-annealing process. This leads to a better phase segregation between the blocks. The P*t*BA chains which had formed the defect regions of the PCEMA layer will then be able to migrate into the core phase. When DN passes through the PCEMA layer, it then has to penetrate through the PCEMA layer uniformly at all positions. This leads to a uniform swelling of the cylinders. As the P*t*BA core absorbs more DN, which leads to an expansion of the total volume of the core phase, the density of the P*t*BA chains in the core decreases. After the P*t*BA chains were converted into PAA chains, the volume fraction of the polymer chains in the core phase decreased further. Therefore, the core phase appears lighter in the TEM images.

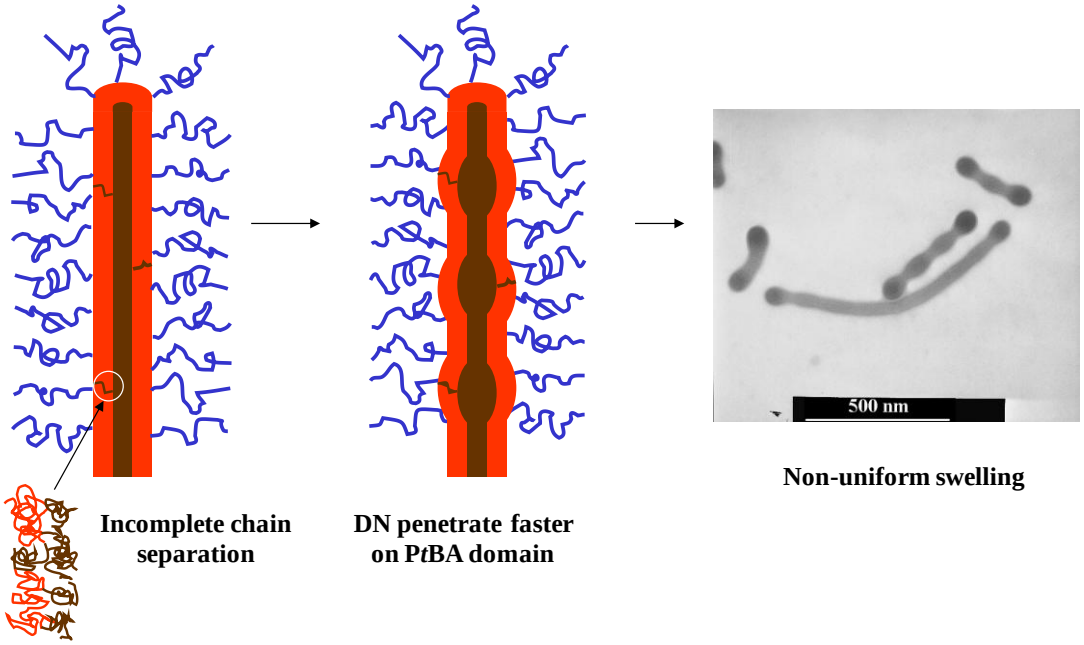

Figure 3.7. The mechanism of the non-uniform swelling of the cylindrical aggregates in water/DN mixture.

3.4 Conclusions

Nanoaggregates formed by PGMA-*b*-PCEMA-*b*-P*t*BA block copolymers were prepared by directly dispersing the block copolymer in water. Factors affecting the morphologies of the obtained nanoaggregates were studied. The relationship between the morphological transition of these nanoaggregates and the weight or volume fraction of the hydrophilic blocks are similar to results obtained with the PS-b-PAA diblock copolymers. The morphologies of the nanoaggregates were also affected by varying the composition of the solvent and the annealing temperature, which may affect the mobility of the polymer chains. The hydrolysis of P*t*BA core of the cylindrical nano aggregates lead to the formation of a cavity in the cylinder. The volume, or the width, of the cavity could be expanded by diffusing DN into the P*t*BA core before hydrolysis. The expansion of the

core could be adjusted by varying the duration of the DN swelling time. These swollen nano channels have potential applications as templates for the growth of inorganic nanocrystals.

References

1. Liu, G.; Yan, X.; Li, Z.; Zhou, J.; Duncan, S. *J. Am. Chem. Soc.* **2003**, *125*, 14039.

2. Yan, X.; Liu, G.; Haeussler, M., Tang, B. Z. *Chem. Mater.* **2005**, *17*, 6053.

3. Hu, J.; Njikang, G.; Liu, G. *Macromolecules* **2008**, *41*, 7993.

4. Zheng, R.; Liu, G. *Macromolecules* **2007**, *40*, 5116.

5. Tao, J.; Stewart, S.; Liu, G.; Yang, M. *Macromolecules* **1997**, *30*, 2738.

6. Zhang, L.; Eisenberg, A. *Science* **1995**, *268*, 1728.

7. Cameron, N. S.; Corbierre, M. K.; Eisenberg, A. *Can. J. Chem.* **1999**, *77*, 1311.

8. Ben-Shaul, A.; Gelbart, W. M. *Ann. Rev. Phys. Chem.* **1985**, *36*, 179.

9. Brandrop, J.; Immergut, E. H.; Grulke, E. A.; Abe, A.; Bloch, D. R. *Polymer Handbook 4th Ed.* John Wiley & Sons, Inc., New York, 1999.

10. Riess, G. *Prog. Poly. Sci.* **2003**, *28*, 1107.

11. Yan, X; Liu, G.; Liu, F.; Tang, B. Z.; Pang, H.; Pakhomov, A. B.; Wong, C. Y. *Angew. Che. Imt. Ed.* **2001**, *40*, 3593.

Chapter 4

Coating and structural locking of dipolar chains of cobalt nanoparticles

4.1 Introduction

Above a critical size, Co nanoparticles may overcome repulsion provided by the coating surfactant molecules, and aggregate due to dipole-dipole interactions, and form chain-like structures.[1,2] These structures include linear chains, loops, networks, and three-dimensional suprastructures as has been predicted theoretically,[3-5] and verified experimentally.[1,2,6,7] While these structures can be beautiful, they are normally not very stable. Multiple rinsing of surfactant-coated Co nanoparticles by a good solvent for the surfactant normally leads to the removal of the surfactant, and thus the collapse of these structures and the precipitation of the Co nanoparticles.[8] The locking of these aggregated structures by crosslinking the coating surfactant molecules may yield interesting materials with novel applications. For example, one can imagine the locking of a three-dimensional network structure, to yield a porous film.[9] Such a framework consisting of polymer-coated Co nanoparticle chains may contract or expand in the presence or absence of a magnetic field, and may be useful in controlled release applications. While such a material will be difficult to prepare, we report in this paper our first step toward this goal. This involves the coating of linear dipolar chains of Co nanoparticles by a diblock

copolymer, and the crosslinking of the anchoring layer of the coating copolymer, to yield "permanent" polymer-coated Co nanoparticle chains.

More specifically, the Co nanoparticles used here were prepared from the high temperature decomposition of $Co_2(CO)_8$ utilizing the diblock copolymer poly(2-cinnamoyloxyethyl methacryate)-*block*-poly(acrylic acid) (PCEMA-*b*-PAA), which we refer to as Polymer I, as a surfactant. This polymer had 30 CEMA units and 4 AA units. The resulting particles were coated by PCEMA-*b*-PAA, with PAA anchored onto the Co surfaces, and the PCEMA block stretching out into the solvent phase (A, Figure 4.1). The Co nanoparticles aggregated into linear chains due to magnetic dipole-dipole interactions. The Co nanoparticles along these linear chains were separated from each other by their PCEMA-*b*-PAA coatings (A→B, Figure 4.1). In order to fully coat the dipolar chains, in a solvent ($CHCl_3$) we mixed them with another diblock copolymer poly(*tert*-butyl acrylate)-block-poly(2-cinnamoyloxyethyl methacrylate) (P*t*BA-*b*-PCEMA), which we refer to as Polymer II, consisting of 210 *t*BA units and 70 CEMA units. To the solution was then added methanol, a block selective solvent in which P*t*BA was soluble. Above a sufficiently high methanol content, the PCEMA blocks of Polymers I and II collapsed from the solvent phase, and the coated dipolar chains were provided colloidal stability by the P*t*BA chains (B→C). Photolysis of this mixture with UV light led to the crosslinking of the collapsed PCEMA layer (B→C), and the structural locking of the dipolar chains.

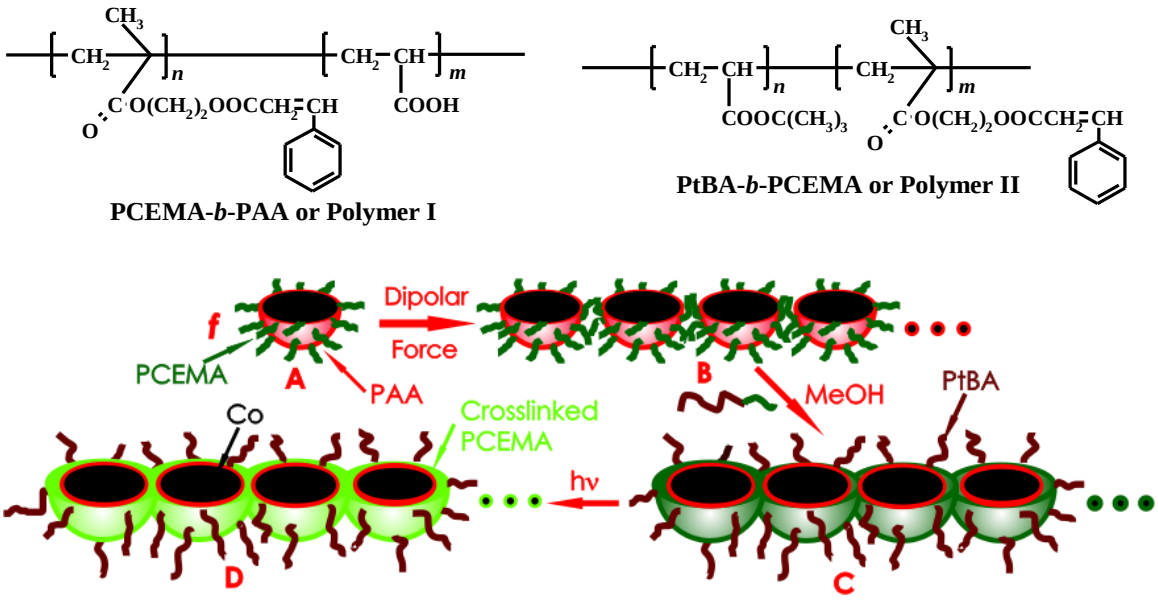

Figure 4.1. Cross-sectional schematic diagram of the formation (A→B), coating (B→C), and structural locking (C→D) of a Co dipolar chain.

While we are unaware of reports of the preparation of solvent-dispersible crosslinked magnetic dipolar chains, Co nanoparticle chains have been assembled at an oil/water interface, and have been "fossilized", or frozen, onto the oil phase surface by photocrosslinking the oil quickly so that it forms a gel.[10] The polymer-coated-particles (POCOPAR) chains described here are closer in structure and properties than the fossilized chains are to the polymer/Ni or polymer/γ-Fe_2O_3 hybrid nanofibers[11-13] that we prepared previously via the production of Ni or γ-Fe_2O_3 in the cores of pre-formed triblock copolymer nanotubes.

4.2 Experimental

Materials. Trioctylphosphine oxide (TOPO, 99%), cinnamoyl chloride (98%), trifluoroacetate acid (TFA, 99%), xylanol orange indicator, ethylenediaminetetraacetic acid disodium salt dehydrate (EDTA, ACS grade), sodium acetate (anhydrous), sodium hydroxide (97%), calcium chloride (Technical grade), and calcium hydride (95%) were purchased from Sigma-Aldrich, and were used as received. The solvent 1,2-dichlorobenzene (DCB, Aldrich, anhydrous, 99%) was washed with concentrated H_2SO_4 once and deionized water thrice. It was then pre-dried by $CaCl_2$ for 24 h, and further dried by refluxing with CaH_2 for another 24 h at 80 ºC. It was distilled under vacuum immediately before use. Cobalt carbonyl [$Co_2(CO)_8$, Fluka, 90-95%] was added in a N_2-filled glove box into DCB, to yield a solution at 100 mg/mL before use. Chloroform (ACS grade), methanol (ACS grade), methylene chloride (ACS grade), diethyl ether (ACS grade), hydrochloric acid (36.5%-38% or 12 M), tetrahydrofuran (THF, ACS grade), and sulfuric acid (96%-98%) were purchased from Fisher Scientific Ltd., and were used as received. Pyridine was purchased from Fisher, and was dried by passing it through two columns of alumina.

The precursors of the diblock copolymers used in this study were all prepared by anionic polymerization.[14,15] Their preparation and characterization have been described previously by our group and are thus not repeated here. As described in the Results and Discussion Section, Polymer I consisted of 30 CEMA units and 4 AA units, while Polymer II consisted of 210 *t*BA units and 70 CEMA units.

Synthesis of Cobalt (Co) nanoparticles. Three batches of Co nanoparticles were prepared under identical conditions, and were found by microscopy analyses to possess essentially identical sizes and shell thickness. The preparation of one batch of nanoparticles involved discharging 36.8 mg of Polymer I, and 4.5 mg of TOPO, into a 50-mL two-neck round-bottom flask. The flask and the attached condenser were sealed with rubber septa. The system evacuated, and then filled with N_2. This process was repeated five times before 3.0 mL of freshly distilled DCB was injected into the flask. The solution was heated in an oil bath to 180 °C within 20 min. Under vigorous stirring, 1.00 mL of a DCB solution of $Co_2(CO)_8$ with a concentration of 100 mg/mL was rapidly injected into the flask. Two minutes later, another 1.0 mL of this $Co_2(CO)_8$ solution was rapidly injected into the flask. The mixture was stirred at 180 °C for 10 min. After this, the heater was turned off, and the solution was allowed to cool to room temperature over ~30 min. The solution was transferred into a glass vial for storage.

Yield analysis. The yield of one batch of particles was determined gravimetrically. This involved first adding into a pre-weighed vial 0.714 g (~0.55 mL) of the synthesized cobalt nanoparticle dispersion in DCB. Approximately 0.6 mL of diethyl ether was then added to precipitate the particles. The precipitate was kept at the bottom of the vial by a 0.47 T magnetic field, and the supernatant was decanted. Our preliminary experiment demonstrated that at this DCB/diethyl ether volume ratio, Polymer I remained dispersed in the solvent phase. The precipitate was subsequently dried under vacuum for 24 h before being weighed. The yield, defined as the ratio of the weight of Polymer I-coated Co nanoparticles relative to that of Polymer I and Co fed into the system, was 77%.

Permanent Cobalt nanoparticle chains. Into a glass vial 0.645 g (~0.50 mL) of a Co nanoparticle dispersion at 16 mg/mL in DCB was charged. The cobalt particles were captured by a magnet at 0.47 T, and the DCB was decanted. The captured Polymer-I-coated Co nanoparticles were redispersed in 5.00 mL of $CHCl_3$, which is a good solvent for both PCEMA and PtBA. 9.0 mg of Polymer II was added into the dispersion. The mixture was vortexed for 3 min before it was transferred into a 250-mL two-neck round-bottom flask. This mixture was stirred mechanically at 100 rpm for 5 min, and 20 mL of methanol, was added over 5 min in order to induce the precipitation of PCEMA. This was followed by the immediate transfer of the resulting mixture into a 30-mL crosslinking cell, and the mixture underwent photolysis for 24 h in order to crosslink the PCEMA block. The light beam was from a 500 W mercury lamp in an Oriel 6140 lamp housing, powered by an Oirel 6128 power supply. Short-wavelength light was removed by passing it through a 270-nm cut-off filter.

The crosslinked cobalt nanoparticle chains were stable against repeated solvent (i.e. $CHCl_3$) rinsing. Placing the dispersion against a magnet with a field strength of 0.47 T for 10 min essentially allowed the complete capture of the chains. This was followed by the decantation of $CHCl_3$. The particles, or chains, were redispersed into $CHCl_3$ and were subjected to the magnetic decantation rinsing treatment thrice before physical analysis and characterization.

CEMA double bond conversion during photolysis. The degree of CEMA double bond conversion for the crosslinked Co nanoparticle chains was determined by absorbance analysis in $CHCl_3$ at 278 nm, which was the absorption maximum for PCEMA. Since Co also absorbed light at this wavelength, the spectrophotometric analysis was performed only after Co dissolution by HCl. In order to determine the extent of the PCEMA double bond conversion for the Polymer II-coated dipolar chain sample described above, 2.00 mL of the Co nanoparticle sample in $CHCl_3$/methanol at v/v = 1/4 before photolysis, and another sample after the photolysis, were blown by N_2 to remove the solvents. These samples were further dried under vacuum for 24 h. Each of the solid samples (3.608 mg for the uncrosslinked sample, and 3.162 for the crosslinked sample) was redispersed in a precisely-weighed amount of $CHCl_3$ (0.9203 g for the uncrosslinked sample, and 1.0301 g for the crosslinked sample) and 0.5 mL of 6.0 M HCl. After the cobalt particles were fully dissolved, the aqueous phase was separated, and the oil phase was extracted again with 0.5 mL of 6.0 M HCl. This was repeated twice. From the oil phase, a solution (66.9 mg for the uncrosslinked sample, and 65.8 mg for the crosslinked sample) was taken and was diluted by a weighed amount of $CHCl_3$ (7.055 g for the uncrosslinked sample, and 7.3562 g for the corsslinked sample). Comparison of UV absorbance of the two samples yielded a CEMA double bond conversion of 43%. All other Polymer II-coated Co particles were irradiated under similar conditions, and should possess a similar degree of CEMA double bond conversion.

Analysis of Co Content of the Nanoparticles. In order to determine the Co content in 8.9 mg of a Polymer I-coated Co nanoparticle sample, the particles were dispersed in 0.30

mL of $CHCl_3$ in a vial. This was followed by the addition of 0.50 mL of 6.0 M HCl to dissolve the Co, and the mixture was stirred for 4 h. The appearance of a light blue color in the aqueous phase, and the loss of the dark color of Co in the organic phase indicated the complete dissolution of Co. At this stage, the mixture was transferred into a 100 mL round-bottom flask, and the vial was rinsed five times with 1.0 mL solutions of 3.0 M sodium acetate. The pH of the combined solution was adjusted to 5.8 using a 3.0 M NaOH aqueous solution. The solution was then heated to 90 °C in an oil bath to evaporate $CHCl_3$, and precipitate the polymer. This was followed by the addition of 4 drops of xylanol orange indicator, which caused the color of the solution to change from pink to purple. The amount of Co^{2+} ions in the solution was determined by complexometric titration using a 3.88×10^{-3} M EDTA solution. At the endpoint, the color of the solution changed from purple to yellow, and the amount of EDTA solution used was 27.02 mL. The Co mass content in the Polymer-I-coated Co nanoparticles was calculated to be 70%. The Co utilization rate, defined as the mass ratio of the Co found in the product, compared to that fed into the system in the form of $Co_2(CO)_8$, was 82%. The Co content in the Polymer II-coated Co chains was determined analogously, and was found to be 46%. The Co utilization rate in this case was 40%.

TEM analyses. Transmission electron microscopy (TEM) images were obtained using a Hitachi H-7000 instrument, operating at an accelerating voltage of 75 kV. When samples were prepared to allow viewing of the Co cores, the samples were aspirated on carbon-coated copper grids, and were analyzed directly without further staining. In order to view

the polymer layer, aspirated samples were stained by OsO_4 or RuO_4 vapor for 30 min before analyses.

X-Ray diffraction analysis. A 50 mg sample of Polymer I-coated Co nanoparticles was mounted as a thin layer on a Si disc. The sample was scanned with a Philips X'Pert Pro MPD diffractometer, fitted with an X'Celerator high speed strip detector. Co Kα radiation (Fe filtered) was used. The count time was 40 sec, at 0.02º 2θ increments. The sample was rotated at a rate of 2 sec/revolution. The scan pattern was converted into Cu radiation, which gives a 2θ range of 17°-96°.

Magnetic property measurement Magnetization curves of Co nanoparticle and cobalt nanoparticle chains were measured at 300 K on a Quantum Design SQUID magnetometer. The amount used for the cobalt nanoparticles was 5.81 mg and that for the cobalt nanoparticle chains was 4.12 mg. To obtain cobalt nanoparticles, a cobalt particle dispersion (1.5 mL in DCB at 16 mg/mL) was placed next to a 0.47-T magnet for 2 h to capture the Co nanopartricles. The solvent was removed by a pipet before 5.0 mL of hexane was added. The solid was vortexed with hexane and the solid was captured once again by the magnet. The rinsing step was repeated another time to fully remove DCB. The cobalt particles were then dried under vacuum for 2 d to yield the solid. Sample 2 solid was obtained by placing a cobalt nanoparticle chain solution in $CHCl_3$ next to the magnet to capture the solid. The solid was dried under vacuum.

4.3 Results and discussion

4.3.1 Polymer characterization

Polymer I was characterized in the PCEMA-*b*-P*t*BA form for the similar solubility of the two blocks. Since the typical protocol for the characterization of block copolymers has been reported previously,[16,17] it was not repeated in the Experimental Section. The repeat unit number ratio, n/m, for each diblock copolymer was determined by comparing the intensities of the ^{1}H-NMR peaks measured in $CDCl_3$ of its two constituent blocks. The specific refractive index increment, dn_r/dc, and the light scattering (LS) molecular weight M_w of the copolymers were determined in butanone. The polydispersity index M_w/M_n of the sample was measured by size-exclusion chromatography (SEC) in THF based on polystyrene standards. By Combining the n/m ratios and light scattering M_w values, the weight-average repeat unit numbers n_w and m_w for each diblock copolymer were calculated (Table 1). Polymer I consisted of 30 CEMA and 4 AA units. Polymer II consisted of 210 *t*BA and 70 CEMA units.

Table 4.1. Molecular properties of Polymers I and II

Polymer	SEC M_w/M_n	dn_r/dc (mL/g)	LS $10^{-4} \times M_w$ (g/mol)	NMR n/m	n_w	m_w
I [a]	1.04	0.121	0.83	8.0/1.0	30	4
II	1.08	0.117	6.4	2.9/1.0	210	70

[a]: Characterized in the PCEMA-*b*-PtBA form.

4.3.2 Co nanoparticles

There have been many reports of the preparation of Co nanocrystals having different geometries.[18] Co nanoparticles have been prepared typically from two methods at high temperatures. Method 1 involves the high temperature decomposition of a Co(0) precursor, such as $Co_2(CO)_8$, in the presence of a surfactant (such as oleic acid) and a co-surfactant (such as TOPO).[19,20] The surfactants were used to regulate the growth of the Co nanoparticles, and to provide the final nanoparticles with colloidal stability. TOPO, binding reversibly to Co, was used mainly to provide a narrow particle size distribution. Method 2 involves the reduction of Co^{2+}, using a reductant in presence of a surfactant and co-surfactant.[21,22] Aside the use of small-molecule surfactants, random copolymers,[23-25] block copolymers,[8,26] and end-functionalized copolymers[7] have also been used as surfactants.

We prepared Co nanoparticles from the high temperature decomposition of $Co_2(CO)_8$ in dichlorobenzene, using Polymer I and TOPO as the surfactant and co-surfactant, respectively.[20] We used a double injection protocol for the $Co_2(CO)_8$ precursor, because

it helped yield particles with narrow size distributions, as discovered by Peng and coworkers.[27] After each preparation, the particles were purified by magnetic decantation, which involved the capturing of the particles on the wall of a vial placed next to a magnet, the decantation of dichlorobenzene, and redispersion of the particles into chloroform. TEM images of a Co nanoparticle sample that was aspirated onto carbon-coated copper grids are shown in Figures 4.2 (a) and (b).

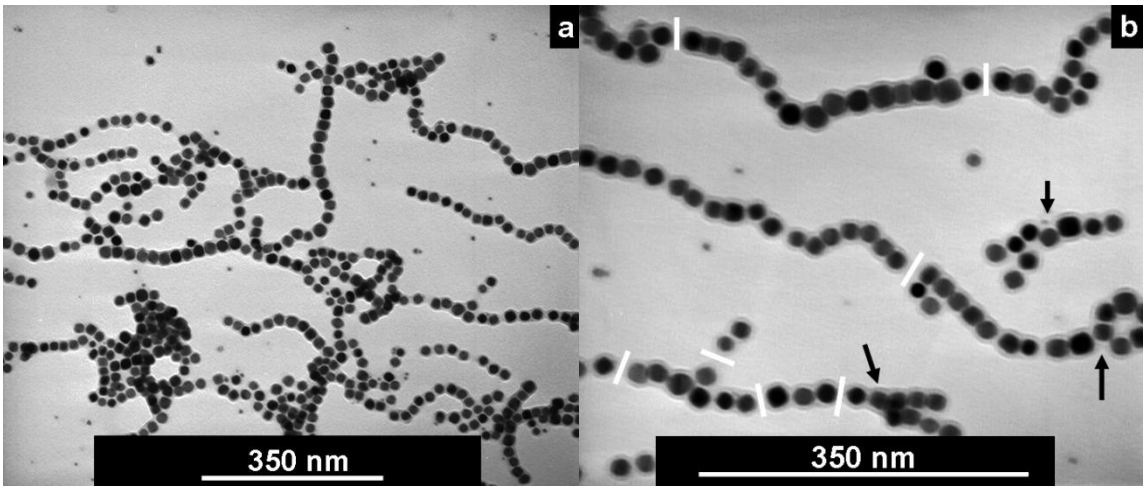

Figure 4.2. TEM images of Co nanoparticles aspirated onto carbon-coated copper grids at low (a) and high (b) magnifications. The left sample was stained by OsO_4.

These images reveal a number of features of the particles. First, the particles had a core-shell structure, as seen in Figure 4.2 b. The core apparently consisted of the more strongly electron-diffracting Co nanocrystal, while the shell consisted of PCEMA-*b*-PAA. The shell thickness was measured along the line which coincided with the radial directions of each constituent Co nanoparticle and the dipolar chain. The average shell thickness of over more than 100 particles was 5.5 ± 0.7 nm for this sample. Secondly, the particles had a relatively narrow size distribution, in agreement with results reported for another polymer-ligand-based system.[7] Averaging a sample of over 100 Co nanocrystals,

we obtained an average Co core diameter of 19.4 ± 2.1 nm. Also, most of the particles existed in an aggregated form. Rather than aggregation into compact three-dimensional clusters, which would be expected if non-directional or isotropic van der Waals attractions operated between the different particles, the particles aligned into linear and branched chains (marked by regular arrows). We also observed that the average spacing, or the shortest distance between two neighboring Co particles in the dipolar chains was 3.6 ± 1.0 nm. In order to obtain this average, we have excluded the pairs of particles which are marked by white lines in Figure 4.2 b, because they had separation distances larger than 6 nm, and appeared to belong to different dipolar chains, or to be in a transition between association and dissociation.

Since the AA groups should bind much more strongly to Co than PCEMA,[28] Polymer I should bind to the Co nanoparticle surfaces through the PAA block, as depicted in Figure 4.1. The diblock copolymer consisted of a total of 34 units of CEMA and AA. The length of a fully stretched chain of this copolymer is 8.6 nm. Assuming Gaussian chain conformation, and a statistical bond length of 0.15 nm, the root-mean-square end-to-end distance is 4.1 nm. The fact that the layer thickness was at 5.5 nm, which is between 4.1 and 8.6 nm, is consistent with the lengths of this copolymer.

While linear and branched chains are theoretically-predicted structures formed from the self-assembly of dipolar particles,[4,5] we should be cautious in drawing conclusions about the true existence of the branched chains in the solution phase. They could have formed

during chloroform evaporation or TEM specimen preparation. The linear chains must have already existed in the solution phase, because they were far more ubiquitous than the branched structures. Their existence in solution has been demonstrated by various groups using techniques such as cryo-TEM,[1] as well as structural-locking of Co dipolar chains followed by the confirmation of the chain structures using microscopy.[10] In our case, the existence of chain structures solution will be unambiguously proven by our ability to coat and lock these structures in solution.

The average particle spacing for both batches of Co nanoparticles in dipolar chains is 3.6 nm. This was much smaller than 2×5.5 nm, with 5.5 nm being the PCEMA-*b*-PAA shell thickness. This suggests extensive compression of the surface PCEMA chains was occurring between different particles, as depicted in B of Figure 4.1. Zhulina *et al.*[29] have argued that two identical approaching brush layers should each become compressed, rather than undergo intermixing, if the spacing between the substrates is greater than the unperturbed dimension of the polymer coils in solvent. For PCEMA, with 30 repeat units, its radius of gyration should be near 1.6 nm. Based on these considerations, we have thus depicted in B of Scheme 1 compressed, rather than mixed, PCEMA chains between two neighboring Co nanoparticles in a dipolar chain. Later in this chapter, experimental evidence will be presented which proves this assumption to be correct.

The small interparticle distance observed in the dipolar chains described above suggests that the dipolar attraction force between these chains was strong. Quantitatively, the

dipolar coupling constant (λ), defined as the ratio between the dipolar interaction energy and the thermal energy k_BT, can be expressed as:[7,30]

$$\lambda = \frac{\mu^2}{4\pi\mu_r\mu_0\sigma^3 k_B T} \qquad (4.1)$$

Where μ_0, $4\pi\times10^{-7}$ NA^{-2}, is the magnetic permeability of the vacuum, μ_r is the relative permeability for the diamagnetic $CHCl_3$/MeOH solution mixture at v/v=1/4, which should be close to 1.[31] Also σ is the overall diameter of a Polymer I-coated Co nanoparticle, which was assumed to be 30.4 nm, and μ is the magnetic dipole moment of a Co particle. For a Co particle with a radius *r*, μ is given by:

$$\mu = \frac{4\pi r^3 \mu_0 M_s}{3} \qquad (4.2)$$

where M_s, the saturation magnetization of bulk Co, is 1.4×10^6 Am^{-1}.[32] Inserting equation (4.2) and the relevant information into equation (4.1), we estimated a λ value of 27.5 for Co particles with a diameter of 19.4 nm, thus confirming the presence of a strong dipole-dipole interaction.

Figure 4.3 shows X-ray diffraction data for the Co nanoparticles before their fractionation by magnetic decantation. A comparison with literature data suggests that the particles existed as ε-Co nanocrystals.[22,33,34] We also calculated the average sizes of the nanocrystals using the Scherrer equation:

$$d_X = \frac{K\lambda}{\delta_{2\theta}\cos\theta} \qquad (4.3)$$

where the wavelength λ of X-ray used was $\lambda = 0.15418$ nm, $\delta_{2\theta}$ was the width of a peak at half maximum, θ was the diffraction angle, and K was 1.107 for spherical particles.[35] Using the data of peak 221 (Figure 4.3) and 310 we obtained the nanocrystal diameters of 18.4 and 19.3 nm, which are in agreement with the TEM diameter of 19.4 ± 2.1 nm for these Co nanocrystals.

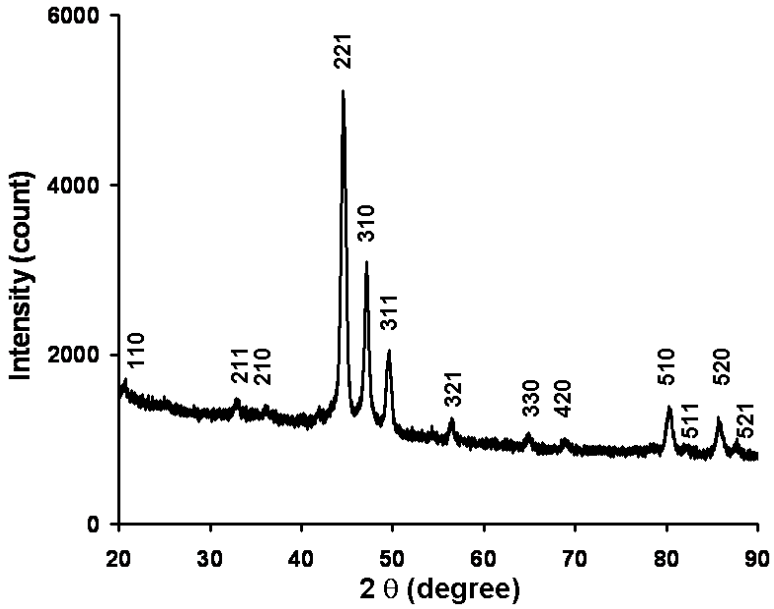

Figure 4.3. X-ray diffraction data for the PCEMA-*b*-PAA-coated Co nanoparticles before their fractionation by magnetic decantation.

To determine the amount of Co in PCEMA-*b*-PAA-coated Co nanoparticles, we stirred the sample in $CHCl_3$ with 6 M hydrochloric acid, in order to dissolve the Co core. The dissolution of Co was indicated by the appearance of a purple color in the aqueous phase and the disappearance of a dark color from the organic phase. The Co^{2+} concentration

was then determined by complexometric titration.[36] This yielded a weight fraction of 70 % for Co in the nanoparticle. Using the densities of 8.9 and 1.25 g/cm^3 for Co,[37] and the diblock copolymer,[38] and a diameter of 19.4 nm for the Co nanoparticles, we calculated a shell thickness of 5.8 nm, which agreed with the value of 5.5 ± 0.7 nm obtained from TEM analysis.

We observed through gravimetric analysis that the utilization rate for the Co element in the precursor $Co_2(CO)_8$ was 82%, while that for PCEMA-*b*-PAA was lower at 67%. This lower than 100% utilization rate values for Co probably resulted from operational sample loss, and the removal of some of the smaller Co nanoparticles during the magnetic decantation step.

In order to determine the extent to which the PCEMA block had undergone thermal crosslinking during the preparation of the Co nanoparticles, a control experiment was performed. In this experiment, PCEMA-*b*-PAA was subjected to the same heat treatment that it would have received during a normal Co nanoparticle preparation protocol, except that $Co_2(CO)_8$ was not used. The polymer was then analyzed spectrophotometrically for PCEMA absorbance analysis at 278 nm. This yielded a CEMA double bond conversion rate of 14%.[39]

4.3.3 Coating and structural locking of the Co dipolar chains

In order to coat the dipolar chains, we mixed the Co nanoparticles with Polymer II, and then added methanol slowly. Due to its insolubility in methanol, the PCEMA block of Polymer I should precipitate from the solvent phase above a critical methanol content. Because of its greater length, the PCEMA block of Polymer II should precipitate from solution before the PCEMA block of Polymer I. Obviously, these two blocks should be compatible with each other. The PCEMA block of Polymer II spread along the surface of the dipolar chains, and the PtBA chains stretched into the solvent phase. Thus, Polymer II formed a brush layer[40-43] on the dipolar chain surface, as depicted in Figure 4.1. The dipolar chains remained dispersed in $CHCl_3$/MeOH, because of the steric stabilization provided by the soluble P*t*BA chains of Polymer II.[44]

Once the dipolar chains were coated by Polymer II, we used a standard protocol, as described in the Experimental Section, for the photolysis of the resulting samples in order to produce "permanent" polymer/Co chains. These samples normally had a PCEMA double bond conversion rate of ~43% during the photolysis step.

We experimented with different dipolar chain-to-Polymer II weight ratios, and found that a mass ratio of ~1/1 worked the best. The use of too much Polymer II yielded samples containing many micellar particles of Polymer II as the background in TEM images. The use of insufficient Polymer II yielded samples that precipitated after two to three rinses of

$CHCl_3$, suggesting incomplete coverage of the dipolar chains by Polymer II. The use of excess Polymer II created no technical problems in purification, as the micelles could be easily removed by magnetic decantation. This involved the capturing of the Co chains by a magnet, and the subsequent decantation of the solvent phase.

Figure 4.4 shows TEM images of a Polymer II-coated and PCEMA-crosslinked Co dipolar chain (or cobalt wire) sample. The sample was coated and crosslinked using the optimized protocols described in the previous paragraph. The dipolar chain structure seen in Figure 4.2 was clearly retained here. The TEM image of Figure 4.4 b shows the thickness of the stained PCEMA layer had increased from 5.5 ± 0.7 to 9.2 ± 1.5 nm, in agreement with the deposition of Polymer II on the original dipolar chains.

We have determined by complexometric titration a Co weight fraction of 46% for cobalt wire sample. Assuming that the weight ratio between Co and Polymer I remained unchanged in the final Polymer II-coated dipolar chains, we calculated weight fractions of 34% for Polymer II, and 20% for Polymer I, in the final dipolar chains. Using the weight fraction of 41% for PCEMA in Polymer II, we estimated that the PCEMA layer thickness in the final Polymer II-coated Co dipolar chains, which had a diameter of 19.4 nm, should be 8.2 nm. This was somewhat smaller than the experimental value of 9.2 ± 1.5 nm, but was within the range for the determined thickness.

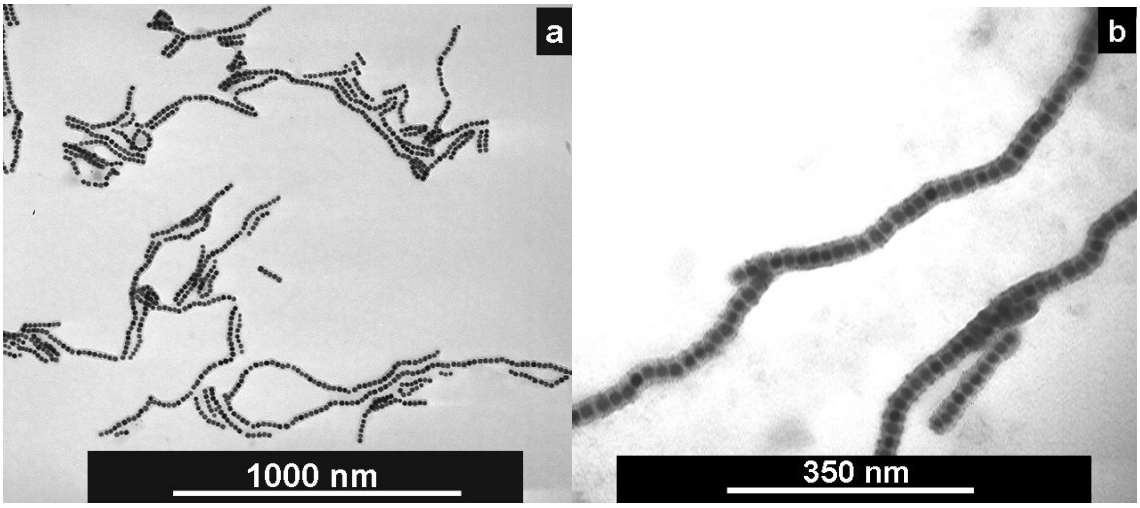

Figure 4.4. Low (left) and high (right) magnification TEM images of Polymer II-coated and crosslinked Batch 2 Co dipolar chains aspirated from $CHCl_3$ on carbon-coated copper grids.

4.3.4 Properties of crosslinked dipolar chains

Aside from the retention of structural integrity as confirmed by TEM, the crosslinked Co dipolar chains retained the magnetic properties of their precursors. Figure 4.5 shows two photographs comparing the status of a Co chain solution in $CHCl_3$ placed in the absence and presence of a magnetic field. In the absence of a magnet field, the particles remained dispersed essentially infinitely long without any agitation. The right picture of Figure 4.5 was taken 5 min after the sample was placed next to a magnet with a field strength of 0.47 T. The clustering of the particles next to the magnet is evident.

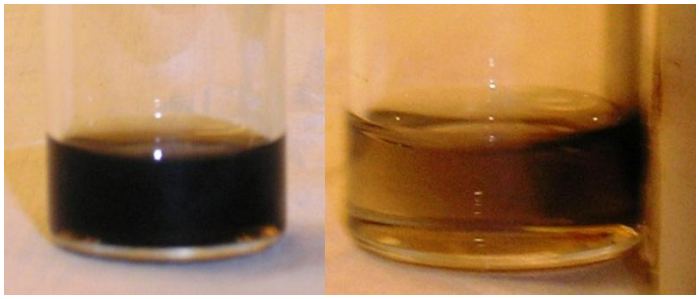

Figure 4.5. Photographs comparing the dispersion states in $CHCl_3$ of a crosslinked Co nanoparticle sample away from (left), and next to (right) a magnet.

Figure 4.6 shows the magnetization curves for powders of Co nanoparticles and cobalt dipolar chains obtained at 300 K. For Co nanoparticles, the saturation magnetization M_S, remanence magnetization M_R, and coercivity H_C were 110 emu/g, 34 emu/g, and 0.79 kOe, respectively. These values changed to 65 emu/g, 19.0 emu/g, and 0.85 kOe for cobalt dipolar chains. Taking the Co weight fractions of 70% and 46% for cobalt nanoparticles and cobalt dipolar chains into consideration, the M_S and M_R values were 157 and 49 emu per g of Co for sample 1 and 141 and 41 emu per g of Co for Co dipolar chains. The two sets of M_S, M_R, and H_C values evidently agree reasonably well with each other. The nonzero M_R and H_C values suggest that the Co nanoparticles at a TEM diameter of 19.4 ± 2.1 nm were ferromagnetic at 300 K, a conclusion in accord with observations made by others before. The M_S values of 157 and 141 emu/g of Co for Co nanoparticles and Co dipolar chains are close to the M_S value of 161 emu/g reported for bulk Co.[7] This suggests the high purity of the Co crystals.

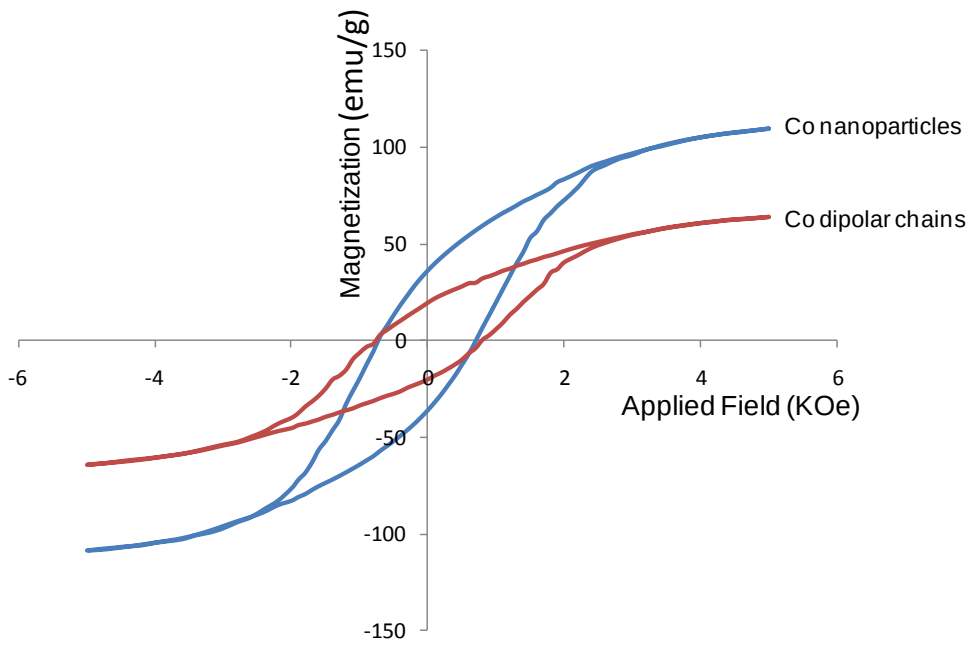

Figure 4.6. Magnetization curve of Co nanoparticles and Co dipolar chains.

To determine what happened to the dipolar chains in magnetic fields on a microscopic scale, we dispensed one drop of a crosslinked Co dipolar chain solution onto a carbon-coated TEM grid placed next to the 0.47 T magnet. After evaporation of the CH_2Cl_2 solvent, we obtained TEM images, with an example shown in Figure 4.7. Some of the dipolar chains became clustered in the presence of the magnetic field. Also, they had a tendency to align along the direction of the magnetic field. These behaviors are similar to those that we have observed for triblock copolymer/γ-Fe_2O_3 hybrid nanofibers.[13]

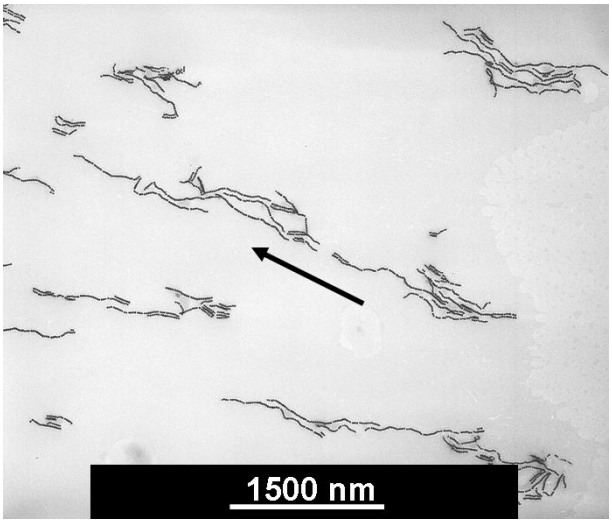

Figure 4.7. TEM image of crosslinked Co dipolar chains left on a carbon-coated copper grid after the evaporation of solvent from one drop of a chain solution in CH_2Cl_2 in the presence of a magnetic field. The arrow denotes the magnetic field direction.

The anticipated advantage of the crosslinked Co dipolar chains was their stability towards repeated solvent rinsing with a variety of different solvents. To show this, we rinsed by magnetic decantation Co dipolar chains that were coated with Polymer II before and after PCEMA crosslinking. Figure 4.8 compares the dispersion states after $CHCl_3$ rinsing three times of two Polymer II-coated samples that were irradiated and not irradiated by UV light. Evidently, the sample that was not irradiated completely lost its ability to disperse after $CHCl_3$ rinsing. We rinsed the crosslinked sample up to ten times, and noticed no change in colloidal dispersibility of this sample. Our suspicion is that the sample would retain its colloidal stability regardless the number of rinsing times. Also, the crosslinked sample could become dispersed in a wide range of good solvents for PtBA, including solvents such as methanol, toluene, and tetrahydrofuran.

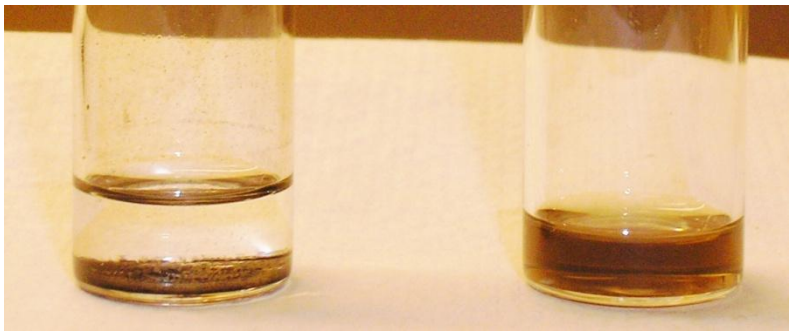

Figure 4.8. Photograph comparing dispersions of Polymer-II-coated Co nanoparticles subjected to no UV irradiation (left) and UV irradiation (right) after rinsing by $CHCl_3$ for three times.

4.3.5 Solvent-dispersible porous nanofibers

As mentioned earlier, Co dissolves readily in HCl. After Co dissolution, the polymer coating remained dispersed in the $CHCl_3$ phase. Samples were aspirated onto a carbon-coated TEM grid and stained by RuO_4. The residual polymer was then analyzed by TEM, with images shown in Figure 4.9 a. This Figure shows that the fibers contained internal cavities that were originally occupied by Co nanoparticles before their dissolution. These polymer/Co dipolar chains may serve as precursors for the preparation of solvent-dispersible porous polymer nanofibers, thus presenting us with a novel architecture.

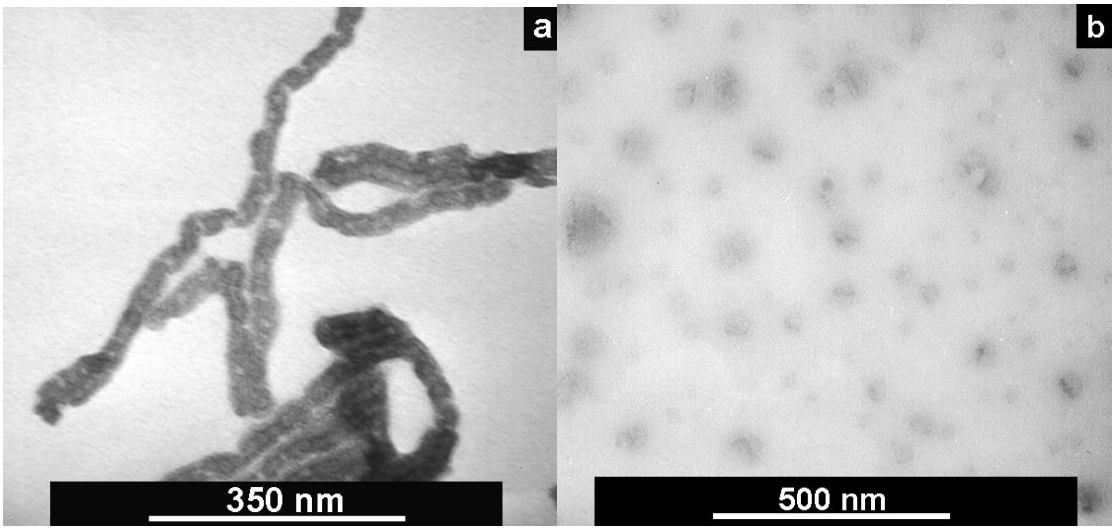

Figure 4.9. TEM images of polymer residues after Co dissolution and aspiration from $CHCl_3$. Image (a) is of a Polymer II-coated and PCEMA-crosslinked sample, while image (b) is of a Polymer I-coated and PCEMA-crosslinked sample.

4.3.6 Crosslinking of Polymer I-coated Co nanoparticles

We have attempted to lock the dipolar chain structure at Stage B of Figure 4.1 for dipolar chains coated by Polymer I. The photocrosslinking of PCEMA at this stage under conditions similar to those used for the Polymer II-coated dipolar chains did help stabilize the dipolar chains against $CHCl_3$ rinsing. The photolyzed Polymer I-coated dipolar chains, however, failed to redisperse into organic solvents such as THF and chloroform after they had been vacuum-dried. This behaviour was similar to that of shell-crosslinked diblock copolymer spherical micelles that we had studied previously.[45] We suspect that this happened probably because the Co nanocrystals were not properly locked into the structures by the PCEMA-*b*-PAA layer. After sample drying and polymer shrinkage, the fragile PCEMA net may have become broken, and the Co eventually escaped partially or fully from the encapsulating net. Without a proper stabilizing layer, the Co particles failed to disperse.

Shown in Figure 4.9 b is a TEM image of the organic residual after Co was dissolved by HCl from a dipolar chain sample. Unidentified pieces of various sizes are seen, including possibly some nanocapsules. While a detailed account of the species seen in Figure 4.9 b is beyond the scope of this thesis, it is clear that the fiber-like structures seen in Figure 4.9 a are not present in this image. This suggests little reaction occurred between the Polymer I chains attached to different Co particle surfaces, and confirms our prior assertion that PCEMA chains of neighboring particles did not undergo significant intermixing.

4.4 Conclusions

$PCEMA_{30}$-*b*-PAA_4 and $PtBA_{210}$-*b*-$PCEMA_{70}$ block copolymers have been synthesized and characterized. Using $PCEMA_{30}$-*b*-PAA_4 as a surfactant, uniform Co nanoparticles coated by $PCMEA_{30}$-*b*-PAA_4 have been prepared from the high temperature decomposition of $Co_2(CO)_8$. With Co diameters of 19.4 ± 2.1 nm, the Co weight fraction of these particles was determined by complexiometric titration to be 70%. The thickness of the $PCMEA_{30}$-*b*-PAA_4 layer was determined by TEM measurements to be 5.5 ± 0.7 nm. The Co nanoparticles aggregate, due to magnetic dipole-dipole interactions, into dipolar chains. Adding methanol into a mixture containing an approximately equal weight of the dipolar chains and P*t*BA_{210}-*b*-$PCEMA_{70}$ in chloroform to a methanol volume fraction of 80% led to the deposition of P*t*BA_{210}-*b*-$PCEMA_{70}$ onto the dipolar chain surfaces. Colloids of these dipolar chains remained stable in solution due to steric stabilization provided by the P*t*BA chains. The PCEMA layer of these chains was crosslinked by

photolysis. These “permanent” and solvent-dispersible dipolar chains were stable against solvent rinsing. These architectures are novel, and may have interesting applications.

References

1. Butter, K.; Bomans, P. H. H.; Frederik, P. M.; Vroge, G. J.; Philipse, A. P. *Nat. Mater.* **2003,** *2*, 88.

2. Pyun, J. *Polymer Reviews* **2007,** *47*, 231.

3. de Gennes, P. G.; Pincus, P. A. *Phys. Kondens. Mater.* **1970,** *11*, 189.

4. Tlusty, T.; Safran, S. A. *Science* **2000,** *290*, 1328.

5. Camp, P. J.; Shelley, J. C.; Patey, G. N. *Phys. Rev. Lett.* **2000,** *84*, 115.

6. Tripp, S. L.; Dunin-Borkowski, R. E.; Wei, A. *Angew. Chem. Int. Ed.* **2003,** *42*, 5591.

7. Keng, P. Y.; Shim, I.; Korth, B. D.; Douglas, J. F.; Pyun, J. *Acs Nano* **2007,** *1*, 279.

8. Liu, G. J.; Yan, X. H.; Lu, Z. H.; Curda, S. A.; Lal, J. *Chem. Mater.* **2005,** *17*, 4985.

9. Safran, S. A. *Nature Materials* **2003,** *2*, 71.

10. Benkoski, J. J.; Jones, R. L.; Douglas, J. F.; Karim, A. *Langmuir* **2007,** *23*, 3530.

11. Yan, X. H.; Liu, G. J.; Haeussler, M.; Tang, B. Z. *Chem. Mater.* **2005,** *17*, 6053.

12. Li, Z.; Liu, G. J. *Langmuir* **2003,** *19*, 10480.

13. Yan, X. H.; Liu, G. J.; Liu, F. T.; Tang, B. Z.; Peng, H.; Pakhomov, A. B.; Wong, C. Y. *Angew. Chem. Int. Ed.* **2001,** *40*, 3593.

14. Wang, G. C.; Henselwood, F.; Liu, G. J. *Langmuir* **1998,** *14*, 1554.

15. Henselwood, F.; Liu, G. J. *Macromolecules* **1997,** *30*, 488.

16. Liu, G.; Yan, X.; Li, Z.; Zhou, J.; Duncan, S. *J. Am. Chem. Soc.* **2003,** *125*, 14039.

17. Yan, X. H.; Liu, G. J.; Li, Z. *J. Am. Chem. Soc.* **2004,** *126*, 10059.

18. Puntes, V. F.; Krishnan, K. M.; Alivisatos, A. P. *Science* **2001,** *291*, 2115.

19. Puntes, V. F.; Krishnan, K.; Alivisatos, A. P. *Topics In Catalysis* **2002,** *19*, 145.

20.Puntes, V. F.; Zanchet, D.; Erdonmez, C. K.; Alivisatos, A. P. *J. Am. Chem. Soc.* **2002,** *124*, 12874.

21. Murray, C. B.; Sun, S. H.; Gaschler, W.; Betley, T. A.; Kagan, C. R. *IBM J. Res. Dev.* **2001,** *45*, 47.

22. Sun, S. H.; Murray, C. B. *J. Appl. Phys.* **1999,** *85*, 4325.

23. Thomas, J. R. *J. Appl. Phys.* **1966,** *37*, 2914.

24. Hess, P. H.; Parker, P. H. *J. Appl. Polym. Sci.* **1966,** *10*, 1915.

25. Burker, N. A. D.; Stover, H. D. H.; Dawson, F. P. *Chem. Mater.* **2002,** *14*, 4752.

26. Platonova, O. A.; Bronstein, L. M.; Solodovnikov, S. P.; Yanovskaya, I. M.; Obolonkova, E. S.; Valetsky, P. M.; Wenz, E.; Antonietti, M. *Colloid Polym. Sci.* **1997,** *275*, 426.

27. Peng, X. G.; Wickham, J.; Alivisatos, A. P. *J. Am. Chem. Soc.* **1998,** *120*, 5343.

28. Zheng, R. H.; Wang, J. D.; Liu, G. J.; Jao, T. C. *Macromolecules* **2007,** *40*, 7601.

29. Zhulina, E. B.; Borisov, O. V.; Priamitsyn, V. A. *J. Colloid Interface Sci.* **1990,** *137*, 495.

30. Rosensweig, R. E., *Ferrohydrodynamics*. Cambridge University Press: Cambridge, 1985.

31. Svoboda, J., *Magnetic Techniques for the Treatment of Materials*. Kluwer Academic Publishers: Dordrecht, 2004.

32. Jeong, U.; Teng, X. W.; Wang, Y.; Yang, H.; Xia, Y. N. *Adv. Mater.* **2007,** *19*, 33.

33. Dinega, D. P.; Bawendi, M. G. *Angew. Chem. Int. Ed.* **1999,** *38*, 1788.

34. Puntes, V. F.; Krishnan, K. M.; Alivisatos, P. *Appl. Phys. Lett.* **2001,** *78*, 2187.

35. Klug, H. P.; Alexander, L. E., *X-ray Diffraction Procedures for Polycrystalline and Amorphous Materials*. John Wiley & Sons: New York, 1954.

36. Malati, M. A., *Experimental Inorganic/Physical Chemistry: An Investigative Approach to Practical Project Work*. Horwood Publishing: Chichester, UK, 1999.

37. Weast, R. C.; Lide, D. R.; Astle, M. J.; Beyer, W. H., *CRC Handbook of Chemistry and Physics. 70th Edition.*; CRC Press: Boca Raton, 1989.

38.Liu, G. J.; Ding, J. F.; Hashimoto, T.; Kimishima, K.; Winnik, F. M.; Nigam, S. *Chem. Mater.* **1999,** *11*, 2233.

39. Guo, A.; Liu, G. J.; Tao, J. *Macromolecules* **1996,** *29*, 2487.

40. Milner, S. T. *Science* **1991,** *251*, 905.

41. Tao, J.; Guo, A.; Stewart, S.; Birss, V. I.; Liu, G. J. *Macromolecules* **1998,** *31*, 172.

42. Tao, J.; Guo, A.; Liu, G. J. *Macromolecules* **1996,** *29*, 1618.

43. Ding, J. F.; Birss, V. I.; Liu, G. J. *Macromolecules* **1997,** *30*, 1442.

44. Napper, D. H., *Polymeric Stabilization of Colloidal Dispersions*. Academic Press: London, 1983.

45. Ding, J. F.; Liu, G. J. *Macromolecules* **1998,** *31*, 6554.

Chapter 5

Preparation of magnetic spheres having segregated surface chains

5.1 Introduction

In this chapter, the preparation and properties of magnetic spheres will be discussed. These spheres (or beads) consist of magnetic material and polymers, which allow the magnetic material to become dispersible in a solvent, which in most cases is water. These beads are of great interest, because one of the potential applications of the beads is towards immunoassays.[1] As shown in Figure 1.10, in such an assay, the beads are first bound with an antigen or antibody. The immobilized biomolecules can then capture their antibody or antigen (or anti-antibody) from a sample mixture containing interference molecules. Consequently, the precise measurement of the antibody or antigen in a biological sample is possible.

The magnetic beads used in these immunoassays should have two important properties. First, the bead should contain sufficient magnetic materials to allow it to be captured magnetically. Second, the surface of the bead should have a sufficient amount of functional groups, which could be used to immobilize biomolecules (such as antigens or antibodies) covalently. A direct method to prepare these kinds of beads is to introduce

ligands that contain desired functional groups onto the surface of the magnetic spheres.[2] The functionalized ligand can be a polymer chain with functional groups attached on the side chains.

Micelles were prepared with magnetic spheres at their cores by mixing the diblock copolymer and magnetic spheres in a block selective solvent. For example, Roullier *et al.* prepared micelles containing iron oxide nanoparticles and fluorescence quantum dots by adding water to the nonpolar solvent dispersion of the nanoparticles in the presence of an amphiphilic polymer ligand.[3] To reduce the total free energy of the system, some nanoparticles were encapsulated in the polymeric micelles. A drawback of these strategies was that the magnetic responses of the beads obtained were not sufficiently high.

Beads with better magnetic properties could be prepared with a polymer template obtained using an emulsion process. For example, uniform polystyrene beads were made via emulsion polymerization. Magnetic particles were attached on the surface of the latex, and the magnetic particle layer was then covered by a polymer layer containing functional groups. Commercial Seradyn beads were produced following this procedure.[4,5] Omer-Mizrahi *et al.* reported the growth of magnetic particles on the surfaces of uniform size-distributed microspheres composed of a polystyrene core and PGMA shell, which was produced by emulsion polymerization.[6] Another example was the preparation of porous polymer beads using the emulsion process.[7] Magnetic nanoparticles were then grown

inside the pores. The resulting magnetic beads were finally covered with a polymer layer bearing the functional groups. Magnetic beads made using these methods had very good magnetic responses, binding capacities, and uniform size distributions. However, the preparation of these beads required many steps.

A direct recipe was to emulsify the magnetic particles in the oil phase by an oil-in-water emulsion process. Recently, Isojima *et al.* reported the preparation of magnetic beads by emulsifying the oil phase containing magnetic particles into the water phase in the presence of a small molecule surfactant.[8] After the solvent evaporation step, emulsion spheres were produced containing solid magnetic cores. Similarly, magnetic beads could be produced by mixing the monomer and magnetic nanoparticles in the oil phase at the beginning, and initiating emulsion polymerization of the monomers.[9] After the monomer was polymerized, the magnetic particles were loaded into the beads without any further steps. However, the beads needed be treated in order to introduce the desired functional groups, which could be used to react with biomolecules.

A one-pot preparation procedure is to prepare the beads by loading magnetic particles into the cores of emulsion droplets in the presence of a polymeric surfactant containing the desired functional groups. Our group reported the preparation of magnetic emulsion spheres by a water-in-oil process using poly(*tert*-butyl acrylate)-*b*-poly(2-hydroxyethyl methacrylate) (P*t*BA-*b*-PHEMA).[10] The obtained emulsion spheres were permanently locked by connecting the PHEMA chains in the core with a small molecule linker. The

spheres were then treated with trifluoroacetic acid (TFA) to convert the P*t*BA chains into poly(acrylic acid) (PAA) chains. After this treatment, the spheres could be dispersed into water. Magnetic spheres obtained from such a process were demonstrated to have potential application in immunoassays, such as those described earlier in this chapter. However, the preparation process of these kinds of spheres had a number of drawbacks, which may limit their application.

The magnetic spheres obtained using the water-in-oil emulsion process were not inherently dispersible in water. Since the desired application of the spheres required their compatibility with aqueous media, these spheres had to be chemically treated in order to allow them to disperse into water. Furthermore, in the chemical treatment reaction, trifluoroacetic acid, an acid that is not compatible with most of the biomolecules, was used. A better preparation process would be to obtain similar spheres using an oil-in-water emulsion process which does not require an additional hydrolysis reaction. Another concern was that the crosslinking of the spheres was conducted in the presence of an organic solvent, which should be avoided in further biological applications.

In this chapter, we report the one-pot preparation of magnetic emulsion spheres *via* an oil-in-water process. One of the surfactants used in the emulsion process contained carboxyl groups in the hydrophilic section. To enhance the stabilization effect of this surfactant, another surfactant, with a hydrophilic section that was not a polyelectrolyte, was used as a co-surfactant. The obtained emulsion spheres were further stabilized by photo-

crosslinking the spheres under a UV beam. Every step was done in aqueous solution without the addition of any organic reactants.

The preparation method and the polymers used in this report are shown in Figure 5.1. Magnetic particles were first synthesized by the thermal decomposition of their precursor in the presence of small molecule ligands. To improve the compatibility between the polymeric surfactant and the ligand used to stabilize the nanoparticle, a diblock copolymer ligand poly(2-cinnamoyloxyethyl methacrylate)-*block*-poly(acrylic acid) (PCEMA-*b*-PAA) was introduced to cover the nanoparticles *via* a ligand exchange process. The emulsion process was accomplished by dispersing the chloroform phase, containing the magnetic particles and the poly(2-cinnamoyloxyethyl methacrylate) (PCEMA) homopolymer, in the water phase in the presence of two diblock copolymer surfactants, poly(2-cinnamoyloxyethyl methacrylate)-*block*-poly(succinoylglyceryl methacrylate) (PCEMA-*b*-PSGMA) and poly(2-cinnamoyloxyethyl methacrylate)-*block*-poly(glyceryl methacrylate) (PCEMA-*b*-PGMA). After the emulsion droplets were formed, the oil phase was removed, yielding spheres with solid cores. The structures of the spheres were then locked by photo-crosslinking the PCEMA chains.

We will demonstrate that the two polymer chains are segregated, and thus generate bumpiness on the surfaces of the magnetic spheres, similar to what we have previously reported in the absence of magnetic particles.[11] We then show that the spheres could be

used to immobilize biomolecules (such as antigens) and capture the antibody of the immobilized antigen.

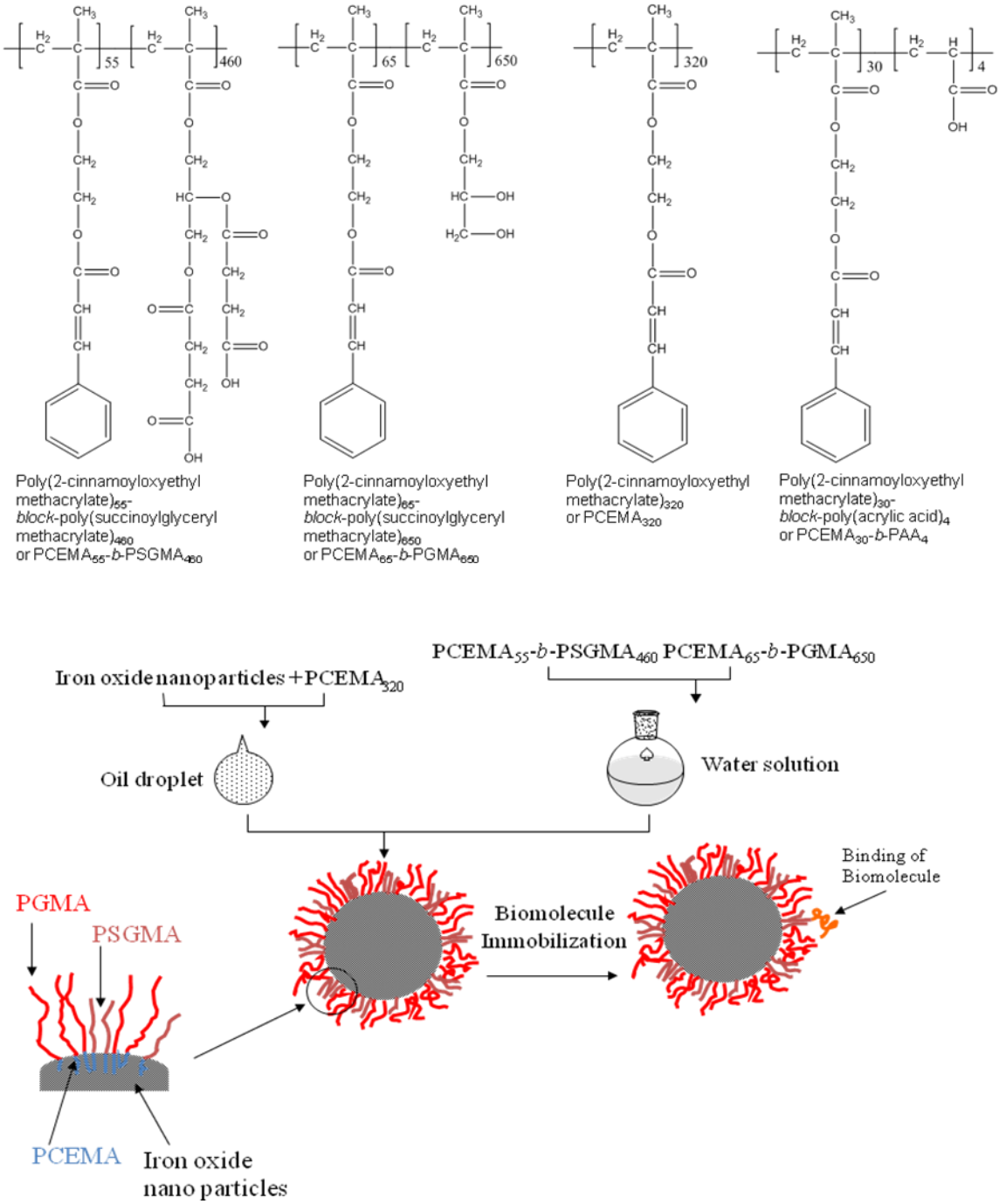

Figure 5.1. Polymers used in the emulsion process (top) and the preparation scheme of the magnetic emulsion spheres (bottom).

5.2 Experimental

Synthesis of the polymers by anionic polymerization. The precursors of the polymers used in this study were synthesized by Dr. Liangzhi Hong *via* anionic polymerization. The polymer precursors were poly(trimethylsiloxyethyl methacrylate)$_{55}$-*block*-poly(solketal methacrylate)$_{460}$ (P(HEMA-TMS)$_{55}$-*b*-PSMA$_{460}$), poly(trimethylsiloxyethyl methacrylate)$_{65}$-*block*-poly(solketal methacrylate)$_{650}$ (P(HEMA-TMS)$_{65}$-*b*-PSMA$_{650}$), poly(trimethylsiloxyethyl methacrylate)$_{30}$-*block*-poly(*tert*-butyl acrylate)$_4$ (P(HEMA-TMA)$_{30}$-*b*-PtBA$_4$), and poly(trimethylsiloxyethyl methacrylate)$_{320}$ (P(HEMA-TMS)$_{320}$). The P(HEMA-TMS) blocks of the polymers were converted into poly(2-hydroxyethyl methacrylate) (PHEMA) blocks by Dr. Liangzhi Hong through the hydrolysis of HEMA-TMS in the presence of methanol. Dr. Hong also prepared poly(2-cinnamoyloxyethyl methacrylate)$_{320}$ (PCEMA$_{320}$) by reacting PHEMA$_{320}$ with cinnamoyl chloride in pyridine. The preparation of PCEMA$_{30}$-*b*-PAA$_4$ from PCEMA$_{30}$-*b*-P*t*BA$_4$was done following the same procedure as described in Chapter 4.

Preparation of PCEMA$_{55}$-*b*-PSGMA$_{460}$ surfactant solution. In a sealed flask, the poly(2-hydroxyethyl methacrylate)$_{55}$-*block*-poly(solketal methacrylate)$_{460}$ (PHEMA$_{55}$-*b*-PSMA$_{460}$) diblock copolymer (1.0 g) was dissolved in 10.0 mL of freshly distilled pyridine. To this solution, cinnamoyl chloride (0.40 g) was added. The mixture was stirred at room temperature overnight. The polymer was then precipitated from 100 mL of methanol. This precipitate was collected by centrifugation at 3000 rpm for 5 min. After the supernatant was decanted, the precipitate was dissolved in 5.0 mL of THF, and

then precipitated upon the addition of 50.0 mL of methanol. After being centrifuged at 3000 rpm for 5 min, the precipitate (PCEMA-*b*-PSMA) was vacuum dried overnight. The conversion of PHEMA chains was measured as 100 % by ^{1}H NMR. The molecular composition of this copolymer was measured by GPC.

The PCEMA-*b*-PSMA diblock copolymer (0.50 g) was dissolved in 6.00 mL of THF. To this solution, 1.50 mL of HCl (6.0 M) was added. The mixture was initially turbid, but became transparent after two hours.[12] This indicated the complete hydrolysis of PSMA into poly(glyceryl methacrylate) (PGMA). The solution was then transferred into a dialysis tube with a cut-off of 12,000 Dalton, and was dialyzed against methanol. The resulting PCEMA-*b*-PGMA was precipitated from ether three times, and was then dried overnight. The ^{1}H NMR spectrum of the sample showed the complete hydrolysis of the PGMA chains.[12]

PCEMA-*b*-PGMA (0.40 g) was charged into a sealed 50 mL round bottom flask. To this flask, 4.0 mL of freshly distilled pyridine and 0.70 g succinic anhydride were added. The mixture was stirred overnight to convert the PGMA chains into PSGMA chains. The conversion was calculated as 100 %, based on the ^{1}H NMR spectrum, which will be discussed in the next section.

The PCEMA-*b*-PSGMA block copolymer (80.0 mg) was dissolved in a mixture of 1.60 mL of THF and 1.60 mL of methanol. To this solution, 12.80 mL of HCl solution (0.10 M) was added dropwise. The precipitated polymer was collected after being centrifuged at 3000 rpm for 5 min. After the supernatant was decanted, the polymer was washed with 5.0 mL of deionized (DI) water five times. The polymer was then dissolved in a mixture of 3.20 mL of THF and 3.20 mL of methanol. To this solution, 11.20 mL of DI water was added. The surfactant solution was stored at 4 °C.

Preparation of $PCEMA_{65}$-*b*-$PGMA_{650}$ surfactant solution. In a sealed flask, the $PHEMA_{65}$-*b*-$PSMA_{650}$ diblock copolymer (1.0 g) was dissolved in 10.0 mL of freshly distilled pyridine. To this solution, cinnamoyl chloride (0.40 g) was added. The mixture was stirred at room temperature overnight. The polymer was then precipitated upon the addition of 100 mL of methanol to this solution. This precipitate was collected by centrifugation at 3000 rpm for 5 min. After the supernatant was decanted, the precipitate was dissolved in 5.0 mL of THF, and was precipitated from 50.0 mL of methanol. After being centrifuged at 3000 rpm for 5 min, the precipitate (PCEMA-*b*-PSMA) was vacuum dried overnight. The conversion of PHEMA chains was measured as 100 % by ^{1}H NMR. The molecular composition of this copolymer was measured by GPC.

The PCEMA-*b*-PSMA copolymer (0.17 g) was dissolved in 2.00 mL of THF. To this solution, 0.50 mL of HCl (6.0 M) was added. The mixture was initially turbid, but became transparent after two hours of incubation. This indicated the complete hydrolysis

of PSMA into PGMA. The solution was then transferred into a dialysis tube with a cut off of 12,000 g/mol, and was dialyzed against methanol. The resulting PCEMA-*b*-PGMA copolymer was precipitated from ether once. The polymer was then dissolved in a solvent mixture consisting of 1.0 mL of THF and 2.0 mL of methanol. This solution was dialyzed against water in a 12,000 g/mol cut-off dialysis tube. After changing the water three times, the solution was transferred into a glass vial. In a pre-weighed glass vial, 0.30 mL of the polymer solution was dried under vacuum, and the weight of the polymer was measured as 9.8 mg. Based on this, the concentration of the surfactant solution was adjusted to 10.0 mg/mL. The dried polymer sample was then analyzed by ^{1}H NMR to verify the 100 % hydrolysis of the PSMA chains.

Preparation of the iron oxide nanoparticles. The iron oxide particles were formed by the thermal decomposition of iron oleate ($Fe(Oleate)_3$).[13] In a 250 mL round bottom flask, 1.44 g of $FeCl_3$ and 8.20 g of sodium oleate were charged. Water (8.0 mL), methanol (11 mL) and hexane (19 mL) were then added, and the salts dissolved immediately. The color of the hexane layer then became dark red, indicating the formation of iron oleate. The mixture was then heated to 70 °C, and this temperature was maintained for three hours. The resulting mixture was then washed three times with water. The hexane layer was collected and dried with anhydrous magnesium sulfate, and the hexane was then removed by rotatory evaporation. In order to prepare wustite nanoparticles, the iron oleate was dried under vacuum at 25 °C for 24 hours. Meanwhile, to make magnetite or Fe_3O_4 nanoparticles, the iron oleate was dried at 70 °C for three hours, and then kept under vacuum at 25 °C for another 20 hours. The recovery yield was 94 %.

To prepare wustite nanoparticles, 4.0 g of the iron oleate, which was vacuum dried at 25 °C, was mixed with 16.0 mL of 1-octadecene in a 100 mL round bottom flask, to give a dark red mixture. The temperature of this mixture was increased at a rate of 3.3 °C/min until it reached 320 °C, and the color of the mixture became black. The mixture was annealed at this temperature for three hours. The obtained iron oxide particles were collected after the mixture was cooled to room temperature.

To prepare magnetite nanoparticles, in a 100 mL flask, 3.0 g of the iron oleate, which was vacuum dried at 70 °C, was mixed with 10.0 mL of 1-octadecene. The temperature of the mixture was increased at a rate of 3.3 °C/min until it reached 320 °C, and the color of the mixture became black. The mixture was annealed at this temperature for 60 min. A portion of the sample (about 3.0 mL) was collected when the reaction mixture was cooled to room temperature. To obtain maghemite or γ-Fe_2O_3, to the rest of the reaction mixture of Fe_3O_4, 0.50 g of trimethylamine oxide was added under nitrogen atmosphere. The mixture was heated to 180 °C at a rate of 5 °C/min, and the temperature was maintained at 180 °C for two hours before the mixture was cooled to room temperature.[22]

To purify the obtained iron oxide nanoparticles, the dispersion of the nano particles (4.0 mL) was first mixed with 16 mL of ethanol. After the precipitate was magnetically captured by a magnet (0.47 T), the supernatant was decanted. To the precipitate, 4.0 mL of hexane was added in order to disperse the particles. These particles were then precipitated upon the addition of 10 mL of acetone.. This process was repeated three

times. The magnetic particles were then dispersed in 4.0 mL of chloroform (containing about 120 mg of iron oxide nanoparticles, the yield was about 95 %).

Ligand exchange. To 4.0 mL of the chloroform dispersion of the iron oxide particles, 240 mg of $PCEMA_{30}$-*b*-PAA_4 diblock copolymer was added. The mixture was then transferred into a dialysis tube with a cut-off of 3500 g/mol, and was dialyzed against chloroform. The sample was collected after changing the solvent six times. The obtained nanoparticles were not dispersible in ether. In a pre-weighed glass vial, to 1.00 mL of this dispersion, 1.50 mL of ether was added to induce the precipitation of the nanoparticles. These nanoparticles were then dispersed in 1.00 mL of chloroform and were precipitated upon the addition of 1.20 mL of ether. The precipitates were captured by a magnet while the supernatant was removed by a glass pipette. This process was repeated four times before the nanoparticles were dried under vacuum. The nanoparticles were then dispersed in chloroform at a concentration of 50 mg/mL. Yield was calculated as 80 %.

Preparation of the magnetic emulsion spheres. In a glass vial, 1.00 mL of the $PCEMA_{55}$-*b*-$PSGMA_{460}$ solution (5.0 mg/mL) was mixed with 0.50 mL of $PCEMA_{65}$-*b*-$PGMA_{650}$ solution (10.0 mg/mL). To this mixture, 0.100 mL of $MgSO_4$ solution (20.0 mg/mL) and 0.08 mL of NaOH solution (0.20 M) were added. The solution was then transferred into a 250 mL double necked round bottom flask. Chloroform-saturated DI water (11.0 mL) was then added into the flask. The pH of the solution was adjusted to

7.0 with 0.10 M HCl and 0.20 M NaOH. The side neck of the flask was then sealed with a septum. To the solution, 0.15 mL of chloroform was added by a syringe, with the needle penetrating the septum. To the dispersion of γ-Fe_2O_3 nanoparticles (0.50 mL, containing 25 mg of the nanoparticles), 16.0 mg of $PCEMA_{320}$ homopolymer was added. The oil phase was transferred into a 1.0 mL syringe after the polymer was fully dissolved. While the aqueous phase was mechanically stirred at 1200 rpm, the oil phase was added dropwise into the aqueous phase in two min. The emulsion mixture was stirred at room temperature for 30 min, and the septa were then removed to allow the chloroform to vaporize. After five min, the mixture was immersed into an oil bath. The temperature of the emulsion dispersion was raised to 45 °C over a period of 15 min, and was left at this temperature for 10 min. The temperature was then increased to 75 °C over a period of 15 min, and this temperature was maintained for 30 min, in order to fully remove the chloroform. The emulsion was then collected.

Purification of the emulsion spheres. The emulsion sphere dispersion (about 8.0 mL) was charged into a 25 mL crosslinking cell. The sample was exposed to a UV beam for three hours in order to crosslink the PCEMA chains. The crosslinked spheres were then centrifuged at 500 rpm twice, and the supernatant was collected. This supernatant was then placed beside a 0.47 T magnet, and the captured magnetic spheres were collected while the supernatant was decanted. This process was repeated three times. The sample was dispersed in water at a concentration of 3.0 mg/mL. The yield was about 85 %.

Crosslinking density analysis. In a glass vial, a 1.00 mL sample of the uncrosslinked spheres (without UV exposure) was placed beside a 0.47 T magnet for 30 min, to ensure that all of the spheres were captured. The precipitate was dispersed into a mixture of 1.0 mL of THF and 1.0 mL of methanol. To this mixture, 0.5 mL of 12 M HCl was added. In another glass vial, 1.00 mL of the crosslinked spheres was treated following the same procedure. The mixtures were allowed to react with acid for two hours before they were transferred into dialysis tubes (12000 g/mol cut off) separately. The samples were dialyzed against methanol for 24 hours. The solvent was changed two times during this duration, until the solution in the dialysis membrane was totally colorless. The dialyzed solutions were transferred separately into two pre-weighed glass vials. The mass of the sample of the uncrosslinked spheres was 1.9971 g, and the mass of the sample of the crosslinked spheres was 2.4793 g. A sample of the uncrosslinked spheres (0.1580 g) was mixed with 1.4120 g of methanol, and the absorbance of this sample at 282 nm was 0.498. A sample of the uncrosslinked spheres (0.1611 g) was mixed with 1.4084 g of methanol, and the absorbance of this sample at 282 nm was 0.203. The mass of the solid residue of each sample after vacuum drying was 1.8 mg for both of the samples. Therefore, the crosslinking density was calculated as 49 %.

Coupling of the emulsion spheres with protein. Bovine serum albumin (BSA) was used as a model protein. In a glass vial, 1.50 mL of the magnetic sphere dispersion was magnetically captured while the supernatant was decanted. Phosphate buffered saline or PBS buffer (1.50 mL) was then added to disperse the spheres. The reaction binding between the calboxylic groups of PSGMA and the amine group of BSA is following a

reported recipe.[14] In another glass vial, 20.0 mg of EDCI and 30.0 mg of NHS was dissolved in 1.00 mL of PBS. To the magnetic sphere dispersion, 0.10 mL of the coupling agent solution was added. The spheres or beads were activated for 15 min before the excess catalyst was removed by magnetic decantation. The beads were then washed twice with PBS. To the magnetic spheres, 1.0 mL of BSA solution (10.0 mg/mL) was added. The mixture was then left in a 4 °C room and was stirred for 20 hours to complete the protein coupling. Finally, the obtained magnetic spheres were washed with PBS three times followed by magnetic decantation. The resulting sample was dispersed in 1.5 mL of PBS.

Determination of the BSA coupling capacity of the magnetic spheres. A standard procedure was used.[14] A bicinchoninic acid or BCA working solution was prepared by mixing BCA reagents A, B and C at a ratio of 25 : 24 : 1. The dispersion of BSA-coupled spheres (0.50 mL) was transferred into a pre-weighed glass vial containing 0.50 mL of PBS. Also prepared were a series of BSA standard solutions with concentrations of 40, 20, 10, 5, and 0 μg/mL. To each of the standard solutions, and the sample dispersion, 1.00 mL of the working solution was added. The samples were then placed in a 60 °C oil bath, and left in it for one hour. The sample dispersion was then placed beside a 0.47 T magnet for three min, to allow the magnetic spheres to be captured, and the supernatant was then collected. The supernatant, together with the standard solutions, was then analyzed by UV-visible spectroscopy within 10 min, and their absorbances at 562 nm were recorded. A calibration curve was plotted using the absorbance of the standards. The amount of BSA coupled to the magnetic spheres was determined from this curve to

be 49 μg. The vial containing the captured magnetic spheres was dried under vacuum overnight. The weight of the dried spheres was 2.2 mg. Thus, the coupling capacity of the magnetic spheres was determined to be 22 μg of BSA per mg of beads.

The binding of anti-BSA with the BSA-coupled magnetic spheres. The anti-BSA-Fluorescein isothiocyanate (anti-BSA-FITC) was diluted to a concentration of 10 μg/mL by PBS buffer. The BSA-coupled magnetic spheres were magnetically captured while the supernatant was decanted. The magnetic spheres were mixed with 2.00 mL of the anti-BSA solution, and the mixture was incubated at room temperature for two hours. The beads were then magnetically captured while the supernatant was transferred into a fluorescence cell, and the fluorescence intensity was measured. The same cell was washed with PBS six times before 2.00 mL of 10 μg/mL anti-BSA-FITC solution was transferred into it, and the fluorescence intensity was measured. The difference between the fluorescence intensities was used to calculate the amount of anti-BSA that was captured onto the beads through antigen-antibody interactions.

Sample characterization. The molecular weights of the copolymers were analyzed by gel permeation chromatography (GPC) using THF as eluent. The ^{1}H NMR spectra of the copolymers were measured in $CDCl_3$ or pyridine-d_5 using a Bruker AC400 instrument.

Thermal gravimetric analysis (TGA) was performed on a TA Q-500 TGA instrument. The sample was first heated from 25 to 200 °C, at a rate of 10 °C/min. This was followed by increasing the temperature from 200 to 500 °C, at a rate of 5 °C/min. Finally, the sample was heated from 500 to 800 °C, at a rate of 10 °C/min.

FT-IR analysis was performed using a Varian 1000 FT-IR instrument. The sample was first dispersed into chloroform. The concentration of the polymer sample was about 5.0 mg/mL, while the concentration of the nanoparticle sample was about 15 mg/mL. The sample dispersion (0.2 mL) was dropped onto a KBr crystal, and formed a uniform layer on the crystal after the solvent was vaporized. The IR spectra were obtained in the transmission mode. Quantitative analysis was performed on a Varian 600-FT-IR instrument. The dried sample was mixed with 100 mg of KBr powder. The sample and the mixture were then ground together, and transferred into a sample holder. The sample was analyzed in DRIFT-IR mode. The absorbance of the sample was recorded using the Kubelka-Munk function. A series of PCEMA-*b*-PAA samples with different polymer/KBr ratios were prepared and analyzed in order to plot a calibration curve. The amount of PCEMA-*b*-PAA in the ligand-exchanged nanoparticles was calculated according to this calibration curve.

Transmission electron microscopy (TEM) images were obtained using a Hitachi H-7000 instrument with an accelerating voltage of 75 kV. The iron oxide samples were sprayed onto carbon-coated copper grids, and were analyzed without further staining. The

emulsion spheres were sprayed onto nitrocellulose-coated copper grids. In order to identify the polymer samples, the PSGMA domains were stained by mixing with uranyl acetate for 20 min. The sample was rinsed with water ten times in order to remove the excess uranyl acetate.

The X-ray diffraction (XRD) analysis of the iron oxide particles was performed on a Philips X'Pert Pro MPD diffractometer using the Co Kα (λ = 1.7890 Å) radiation.

5.3 Results and discussion

5.3.1 Polymer characterization

The polymers used in this study were $PCEMA_{55}$-*b*-$PSGMA_{460}$, $PCEMA_{65}$-*b*-$PGMA_{650}$ and $PCEMA_{320}$. The precursors were synthesized by anionic polymerization in the forms of $P(HEMA\text{-}TMS)_{55}$-*b*-$PSMA_{460}$, $P(HEMA\text{-}TMS)_{65}$-*b*-$PSMA_{650}$ and $P(HEMA\text{-}TMS)_{320}$. The HEMA-TMS blocks were hydrolyzed into the PHEMA form in the presence of methanol. This was followed by conversion of the HEMA blocks into the CEMA form in the presence of cinnamoyl chloride. The polymers were characterized at this stage, in the forms of $PCEMA_{55}$-*b*-$PSMA_{460}$, $PCEMA_{65}$-*b*-$PSMA_{650}$ and $PCEMA_{320}$. The results of these characterizations are summarized in Table 5.1. $PCEMA_{30}$-*b*-$PtBA_4$ was characterized as described in Chapter 4.

Table 5.1. Molecular characterization of the polymers

Polymer composition	dn/dc (mL/g)	GPC result			PSMA/PCEMA from ^{1}H NMR
		M_w	M_n	M_w/M_n	
$PCEMA_{55}$-*b*-$PSMA_{460}$	0.096	108000	106000	1.02	8.3 : 1.0
$PCEMA_{65}$-*b*-$PSMA_{650}$	0.088	152000	148000	1.03	10 / 1.0
$PCEMA_{320}$	0.162	84000	82000	1.02	
$PCEMA_{30}$-*b*-P*t*BA_4	0.121	8300	8000	1.04	8.0 : 1.0*

* PCEMA/P*t*BA from ^{1}H NMR

The diblock copolymers were then treated with HCl to convert PSMA into the PGMA form. The $PCEMA_{55}$-*b*-$PGMA_{460}$ copolymer was reacted with succinic anhydride to yield $PCEMA_{55}$-*b*-$PSGMA_{460}$. The ^{1}H NMR spectrum of the $PCEMA_{55}$-*b*-$PSGMA_{460}$ is shown in Figure 5.2. The integration of H_g is 3.0, and the integration of $H_b + H_c$ is 45. Therefore the contribution from H_c to the integral of $H_b + H_c$ is 4.0. The integration of H_b is calculated as 41, and the integration of H_a is 65. Therefore, the ratio between succinic acid groups to the PGMA backbone is calculated as 1 : 1, indicating a 100 % conversion. The $PCEMA_{30}$-*b*-PAA_4 block copolymer was the same sample that was studied in Chapter 4.

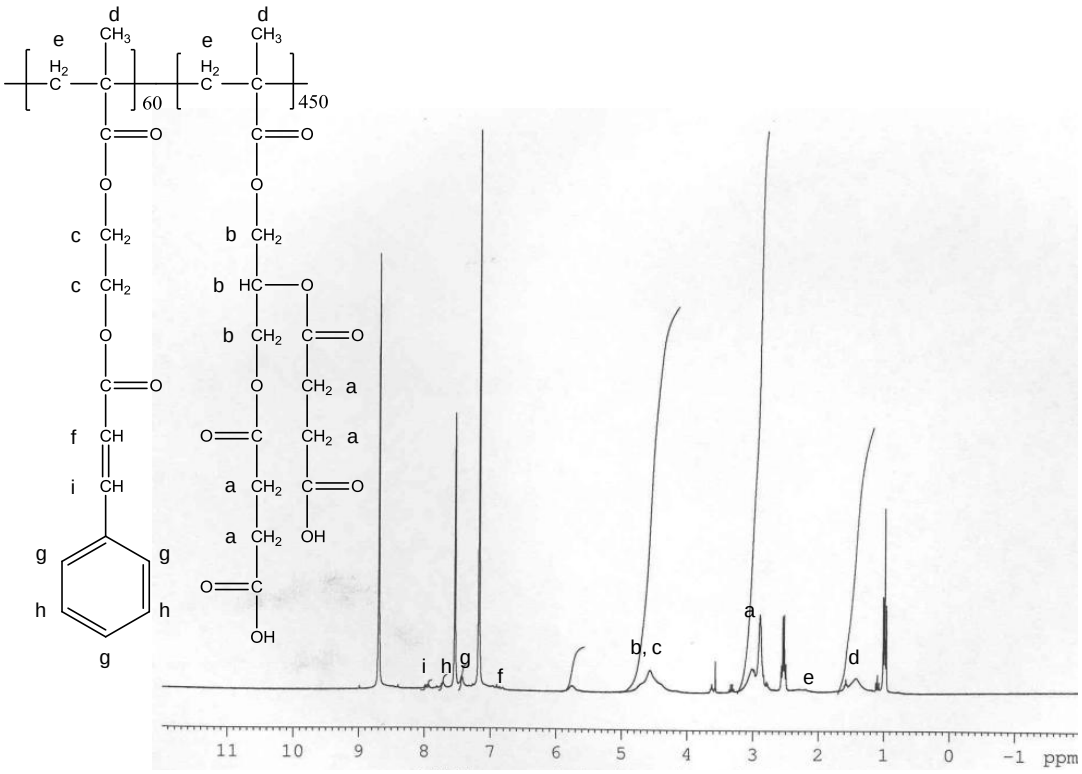

Figure 5.2. ^{1}H NMR spectrum of $PCEMA_{55}$-*b*-$PSGMA_{460}$.

We attempted to analyze the composition of the block copolymers used in this project using TGA (Figure 5.3). However, the decomposition temperature range of PCEMA was not resolved from the decomposition temperature ranges of PGMA and PSGMA blocks. The thermal decomposition curve of $PCEMA_{320}$ shows a 4 % weight loss betweem 100 and 150 °C. The ^{1}H NMR spectrum of the sample does not show significant impurity signals. Therefore, we suspect that this mass loss is due to the moisture acquired by the sample during long term storage (approximately 2 months).

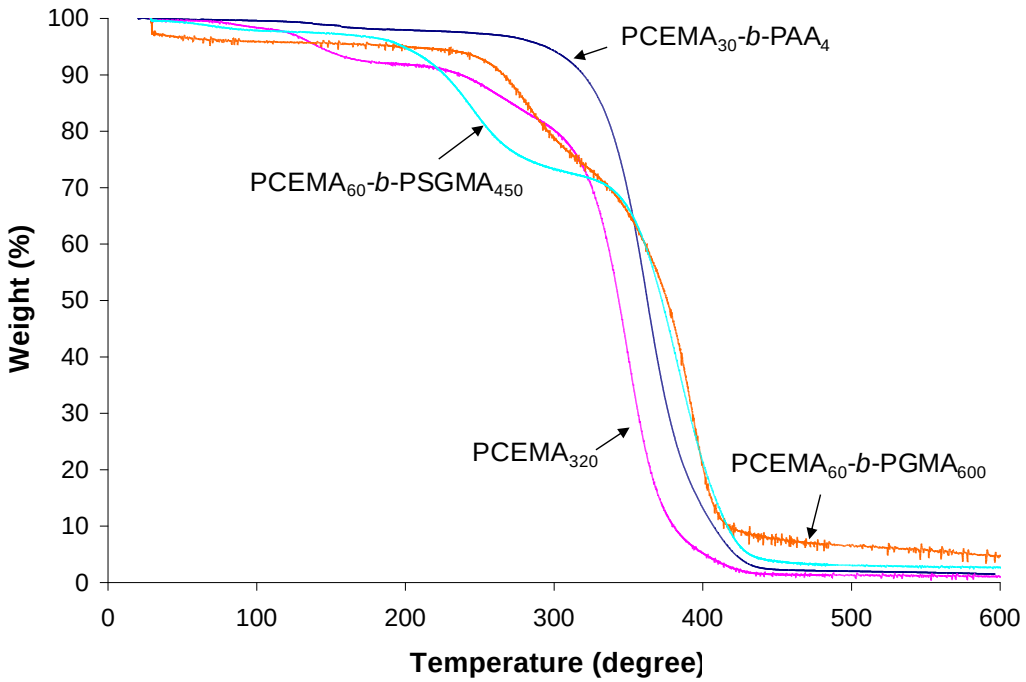

Figure 5.3. TGA plots of the block copolymers.

5.3.2 Synthesis of Fe_3O_4 nanoparticles

Iron oxide nanoparticles could retain different crystal structures, corresponding to their differing magnetic properties. Magnetite (Fe_3O_4) and maghemite (γ-Fe_2O_3) are popular forms of iron oxide, because they are ferromagnetic.[15] The saturation magnetization of magnetite is near 94 emu/g, while that of maghemite is near 72 emu/g. Wustite is a paramagnetic material which has a much lower saturation magnetization (near 15 emu/g) than ferromagnetic materials.[16] Gheisari *et al*. reported that wustite forms ferromagnetic nanoparticles, which have a saturation magnetization value of 11 emu/g at room

temperature.[17] These iron oxide nanoparticles were synthesized by thermally decomposing their $Fe(Oleate)_3$ precursor. This method was first reported by Hyeon *et al.*, who initially believed that Fe_3O_4 nanoparticles were obtained.[13] More recently, however, Hyeon and coworkers have determined that the nanoparticles that they obtained were actually a mixture of Fe_3O_4 and Fe_2O_3 phases.[18] The ratios between Fe_3O_4 and Fe_2O_3 varied, depending on the preparation conditions. This procedure and similar methods were applied successfully by other researchers to prepare Fe_3O_4 nanoparticles having different sizes and shapes. However, iron oxide nanoparticles produced by some groups with similar methods have shown different crystal structures. For example, Bronstein *et al.* obtained wustite nanoparticles by thermally decomposing $Fe(Oleate)_3$ at different temperatures ranging from 318 to 380 °C.[19] The formation of wustite after a similar process was also observed by Bodnarchuk and coworkers.[20]

We obtained both wustite (Fe_xO, x ranges from 0.84 to 0.97) and Fe_3O_4 using the thermal decomposition of $Fe(Oleate)_3$. The TEM images (Figure 5.4) showed that the nanoparticles were very uniform in size. The properties and preparation conditions of our nanoparticles are listed in Table 5.2. Our X-ray diffraction or XRD results (Figure 5.5) showed that the crystal structure of the obtained nanoparticles was affected by some unknown impurities in $Fe(Oleate)_3$. After $Fe(Oleate)_3$ was synthesized, it was purified under vacuum for 24 hours, in order to remove hexane. If the complex was vacuum dried at 25 °C, the decomposition of this precursor yielded wustite nanoparticles. The structure of the nanocrystal was confirmed by XRD (Figure 5.5 a). However, if the $Fe(Oleate)_3$ complex was vacuum dried at 70 °C for 3 hours, the structure of the nanoparticles

obtained from this precursor was verified to be that of Fe_3O_4 containing some wustite (Figure 5.5 b). Bronstein *et al.* studied the structure of $Fe(Oleate)_3$ obtained under different vacuum drying temperatures by IR spectroscopy. They claimed that there were oleic acid dimers present in the complex if it was dried at 30 °C and this dimer disappeared after the complex was vacuum dried at 70 °C. Also, they proposed that one water molecule was bridging two Fe atoms in the molecule of the $Fe(Oleate)_3$ complex if the complex was only vacuum dried at or below 30 °C.[19] We suspected that there was a trace amount of impurities in $Fe(Oleate)_3$, which was introduced by the solvent and the reactant during the synthesis of $Fe(Oleate)_3$, and that these impurities might not be volatile enough to be removed by vacuum drying at low temperature. Those impurities released a reducing reagent after they were annealed at high temperatures, such as 320 °C, leading to the formation of wustite.

Table 5.2. Summary of the preparation and properties of Fe_3O_4 nanoparticles.

Sample Batch	Purification procedure of $Fe(Oleate)_3$	Annealing procedure	Crystal structure	Average size
1	vacuum for 24 hours at 25 °C	Anneal at 317 °C for 3 hours	wustite	16.2 ± 1.7 nm
2	vacuum for 3 hours at 70 °C	Anneal at 317 °C for 1 hour	Fe_3O_4 with wustite content	10.7 ± 0.8 nm
3	vacuum for 3 hours at 70 °C	Add $(CH_3)_3NO$ into Batch 2 and anneal at 180 °C for 1 hour	γ-Fe_2O_3	12.0 ± 0.9 nm

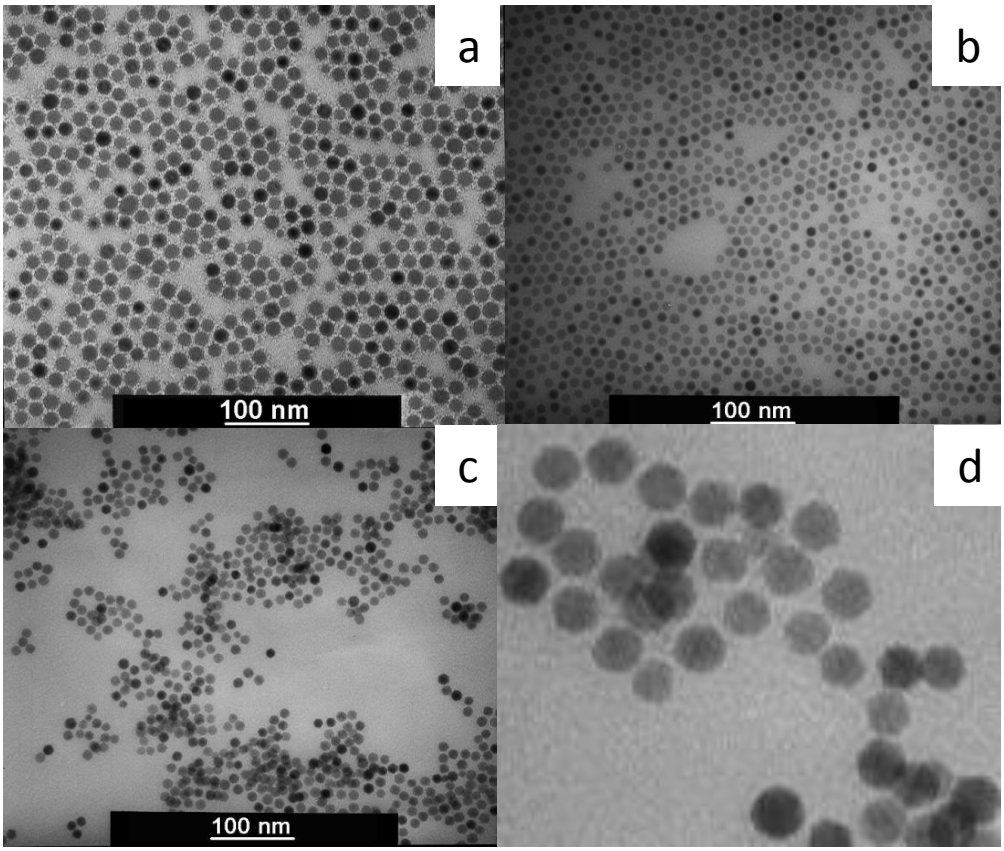

Figure 5.4. TEM images of the iron oxide nanoparticles. (a) Batch 1, wustite, sample was stained with RuO_4, (b) Batch 2, magnetite (Fe_3O_4) with wustite present, (c) Batch 3, maghemite (γ-Fe_2O_3), and (d) Batch 3, with maghemite enlarged.

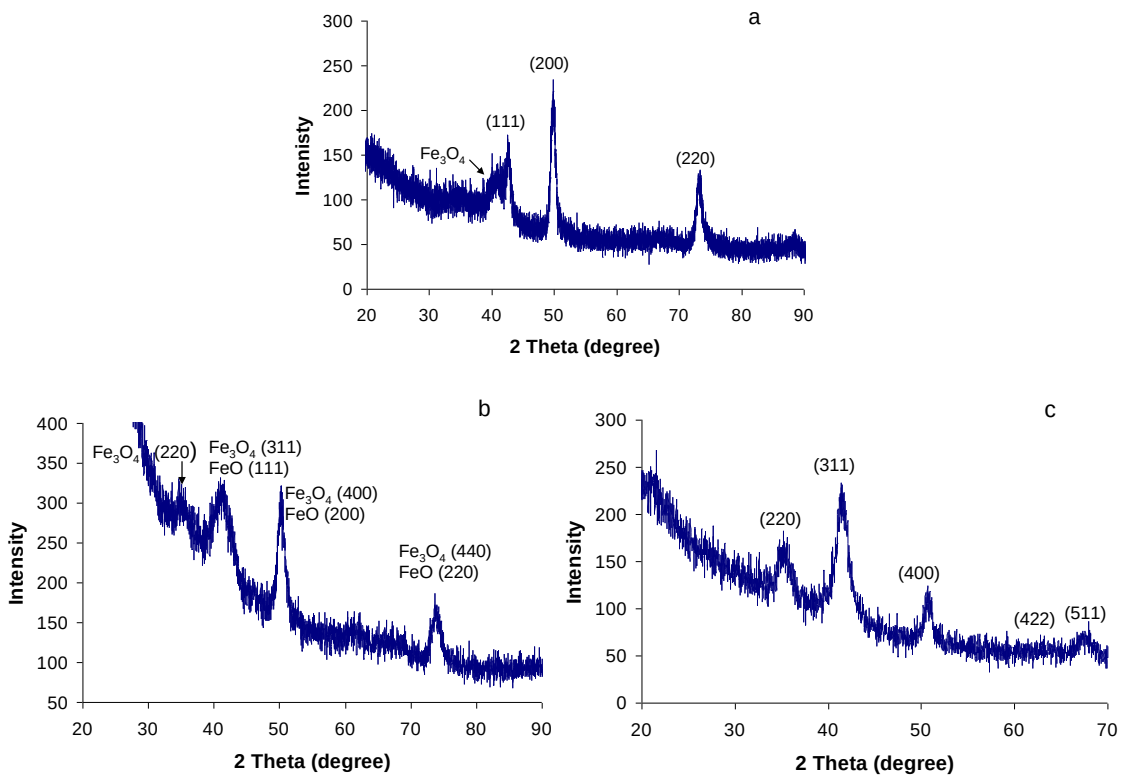

Figure 5.5. XRD pattern of iron oxide nanoparticles. (a) Batch 1, wustite nanoparticle, (b) Batch 2, precursor of γ-Fe_2O_3 nanoparticles, Fe_3O_4 with some wustite present, and (c) Batch 3, Fe_2O_3 nanoparticles.

Wustite is paramagnetic, with a saturation magnetization of 15 emu/g. We performed an optimization study of the emulsion process with this nanoparticle (Batch 1). However, for the desired application, the magnetization of the nanoparticles should be higher. The magnetization values of the Fe_3O_4 nanoparticles obtained using Hyeon's procedure were reported to be 30 - 40 emu/g.[21] These values are higher than those of wustite, but still much lower than the literature values of bulk Fe_3O_4 (92 emu/g) or γ-Fe_2O_3 (72 emu/g).

To the Fe_3O_4/wustite nanoparticle (Batch 2), trimethyl amine oxide, a mild oxidization reagent, was added. This reagent was used to oxidize Fe nanoparticles into γ-Fe_2O_3 nanoparticles by Hyeon and coworkers.[22] The color of the nanoparticle dispersion turned from black to red brown after oxidization. From the XRD pattern (Figure 5.5 c), it was difficult to distinguish between the magnetite and maghemite nanoparticles.[13] However, since an excess amount of oxidation reagent was used (3.0 : 1.0 mole ratio of oxidizing agent to Fe), the obtained nanoparticles should have much greater γ-Fe_2O_3 content than the original Fe_3O_4/wustite nanoparticles. Apparently, the magnetic response of the nanoparticles was greatly improved after the oxidation process. We studied the composition of the Fe_2O_3 nanoparticles obtained by TGA (Figure 5.8). The γ-Fe_2O_3 nanoparticles had an organic content of 15 %.

5.3.3 Ligand exchange

The iron oxide nanoparticles that we have prepared were covered by an oleic acid layer. The loading of these nanoparticles into the cores of emulsion spheres involves a mixing process, in which the nanoparticles were mixed with the PCEMA homopolymer and the PCEMA blocks of the surfactants. The systematic study described in Section 5.3.5.1 will show that the wustite nanoparticles that were covered with oleic acid could not be stabilized by the surfactant after the emulsion process. In order to prepare more stable emulsion droplets, the surface of the nanoparticles must be covered by a PCEMA layer, so that the nanoparticles and the polymer chains are compatible.

In Chapter 3, the preparation of cobalt nanoparticles in the presence of $PCEMA_{30}$-*b*-PAA_4 surfactant was discussed. However, we cannot prepare iron oxide particles with this ligand directly from the thermal decomposition of $Fe(Oleate)_3$. The formation of superparamagnetic iron oxide particles is only possible when the thermal annealing temperature is as high as 300 °C.[18] At this temperature, however, the PCEMA and PAA chains are not stable (Figure 5.3). Thus, we needed to use a two step procedure to prepare PCEMA chains covered iron oxide particles.

The ligand exchange processes of the wustite and maghemite nanoparticles were done following a dialysis method.[23] We calculated the amount of PCEMA-*b*-PAA required by assuming that the thickness of the PCEMA layer is three times the root-mean-square end-to-end distance of the PCEMA-*b*-PAA chains, or 3.8 nm.[24] The density of the layer was estimated as the density of PCEMA, or 1.25 g/mL.[25] As the radius of the nanoparticle is 6.0 nm, the weight ratio between γ-Fe_2O_3 core and PCEMA-*b*-PAA was calculated as 1 : 0.8. The iron oxide particles were mixed with PCEMA-*b*-PAA at a mass ratio of 1.0 : 2.0 (2.5 times that required). The mixture was charged into a 3500 g/mol cut-off dialysis membrane and was dialyzed against chloroform. We analyzed the chloroform outside the dialysis tube by ^1H NMR. After changing the chloroform solvent six times in three days, the chloroform did not contain any detectable oleic acid. Following this treatment, the iron oxide particles could be precipitated from chloroform/ether (1.0 : 1.2 v/v). This indicated that the iron oxide particle was sufficiently covered by PCEMA blocks, since the nanoparticles before ligand exchange were dispersible in both solvents. Our solubility test showed that the PCEMA-*b*-PAA block copolymer was soluble in a mixed solvent of

chloroform/ether (1.0 : 1.2 v/v). The excess PCEMA-*b*-PAA was removed from the nanoparticles by precipitating the mixture in chloroform/ether (1.0 : 1.2 v/v). The particles were then dispersed into 1.0 mL of chloroform. After four cycles of re-dispersion and precipitation, the sample was dried for further use.

To confirm that the PCEMA-*b*-PAA was successfully adsorbed onto the nanoparticles, we analyzed the particles with FT-IR. Figure 5.6 shows the FT-IR spectrum of the γ-Fe_2O_3 nanoparticles before and after ligand exchange. Originally, the nanoparticles were covered by oleic acid, and the peak at 1621 cm^{-1} was assigned as the C=O stretching of oleic acid that was bound with iron oxide, while the C=O stretching of the free oleic acid should occur at 1720 cm^{-1}. This peak would shift to between 1650 and 1550 cm^{-1} when oleic acid was interacting with metal or metal oxide nanoparticles in the form of oleate.[26, 27] Yan *et al* claimed that the complete disappearance of the peak at 1720 cm^{-1} indicated that the oleic acid was completely adsorbed onto the iron oxide surface.[28] After the ligand exchange process, a strong C=O stretching peak was observed at 1716 cm^{-1}, while the C=C stretching and C-C aromatic stretching peaks were observed at 1640 cm^{-1}. By comparing with the spectra of PCEMA-*b*-PAA, these peaks should correspond to the PCEMA-*b*-PAA ligand that was attached to the iron oxide particles after the ligand exchange process. Further evidence of successful ligand exchange is that the particles were not dispersible in ether, which is a poor solvent for PCEMA, while the original oleic acid-stabilized particles were readily dispersed into ether. Similar results were observed with the wustite nanoparticles before and after the ligand exchange process.

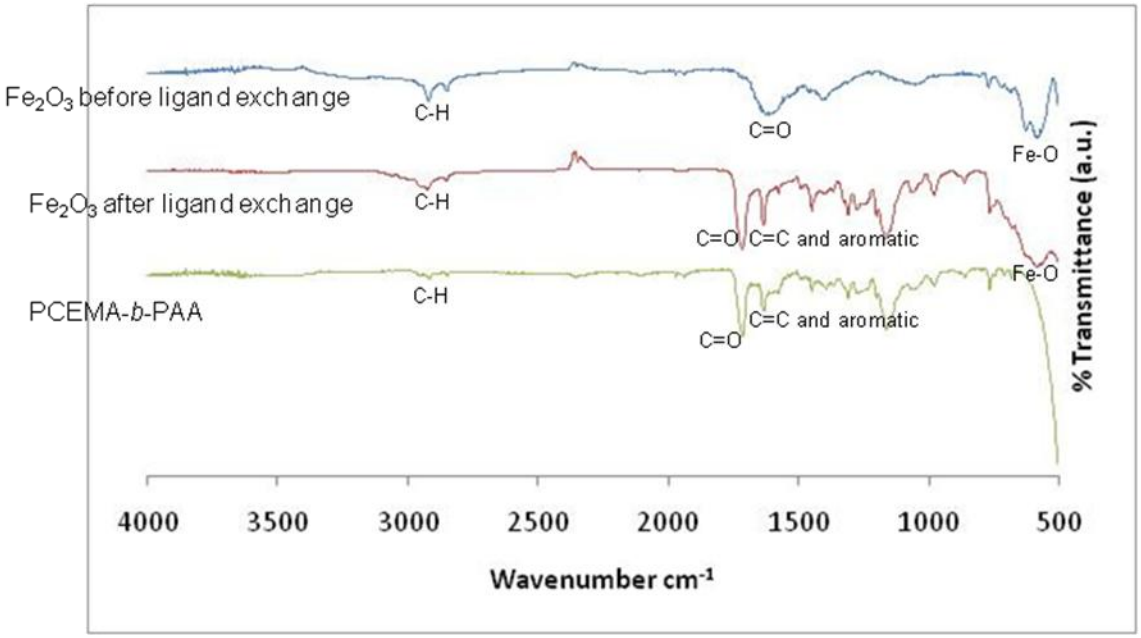

Figure 5.6. FT-IR spectra of the iron oxide nanoparticles before and after the ligand exchange treatment with PCEMA-*b*-PAA.

In order to analyze the mass of the PCEMA-*b*-PAA ligand in the γ-Fe_2O_3 nanoparticle sample, the IR spectra of a series PCEMA-*b*-PAA samples with different PCEMA-*b*-PAA-to-KBr mass ratios were studied. A calibration curve (Figure 5.7) was plotted, based on the mass of the PCEMA-*b*-PAA copolymer in 100 mg of KBr, and the absorbance intensity of the peak at 1716 cm^{-1}. This peak intensity for a mixture of 9.4 mg of ligand exchanged γ-Fe_2O_3 particles and 100 mg of KBr were measured as 1.63. Thus, the weight of PCEMA-*b*-PAA in 9.4 mg of the γ-Fe_2O_3 nanoparticle sample was calculated as 2.6 mg, or the weight fraction of the polymer was 28 %.

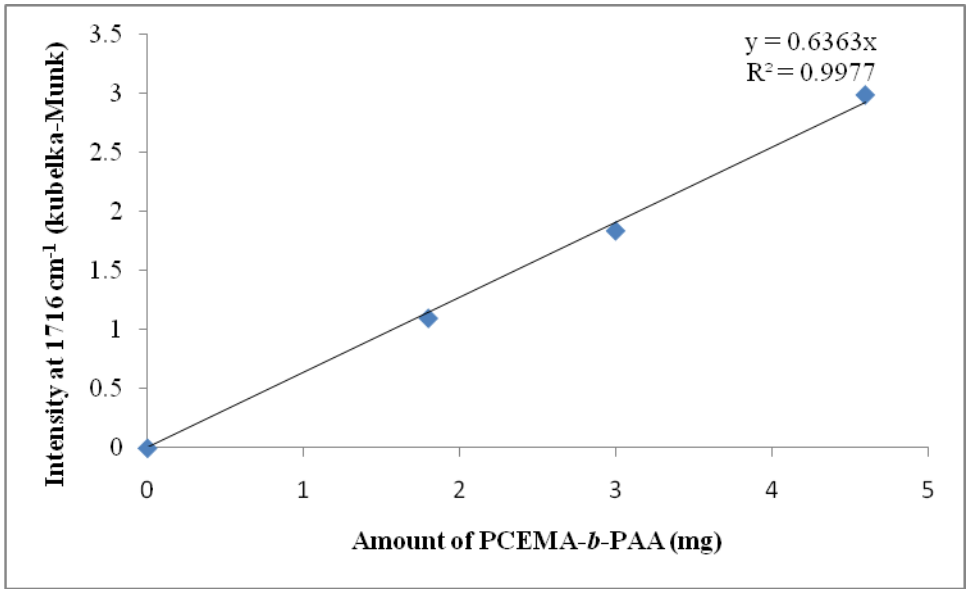

Figure 5.7. Calibration curve of IR intensity of C=O stretch peak from the PCEMA-*b*-PAA ligand at 1716 cm^{-1}.

The composition of the ligand exchanged nanoparticles was studied using TGA. From the TGA curve of the ligand exchanged Fe_2O_3 particles (Figure 5.8), and also considering that the residue from PCEMA-*b*-PAA is about 2 %, the Fe_2O_3 content was measured as 64 %. Thus, the organic content had a weight fraction of approximately 35 %. The weight fraction of the organic layer increased after the ligand exchange. This behaviour suggested that the ligand exchange was successful, since the molecular weight of the polymer ligand is much greater than the molecular weight of oleic acid. The weight fraction of PCEMA-*b*-PAA in the organic content that had decomposed in the range of 250 to 400 °C, which was assigned to be the ligands, was calculated as 80 %. This indicated that the majority of the ligand was exchanged into the block copolymer. The weights of the nanoparticles decreased when the temperature exceeded 650 °C. According to the TGA data of this polymer, the decomposition of the polymers should be

complete below this temperature. We therefore suspected that this weight loss resulted from the reduction of Fe(III) to Fe(II), due to the presence of trace amounts of reducing reagents, such as H_2 or CO, which were released from the decomposed organic content.[29] The weight of the nanoparticles increased a little when the temperature was above 750 °C. A possible reason for this behaviour was that after the reduction of the Fe(III) into Fe(II), some of the Fe(II) was then oxidized by oxygen into Fe(III) once the reducing reagent had reacted completely.

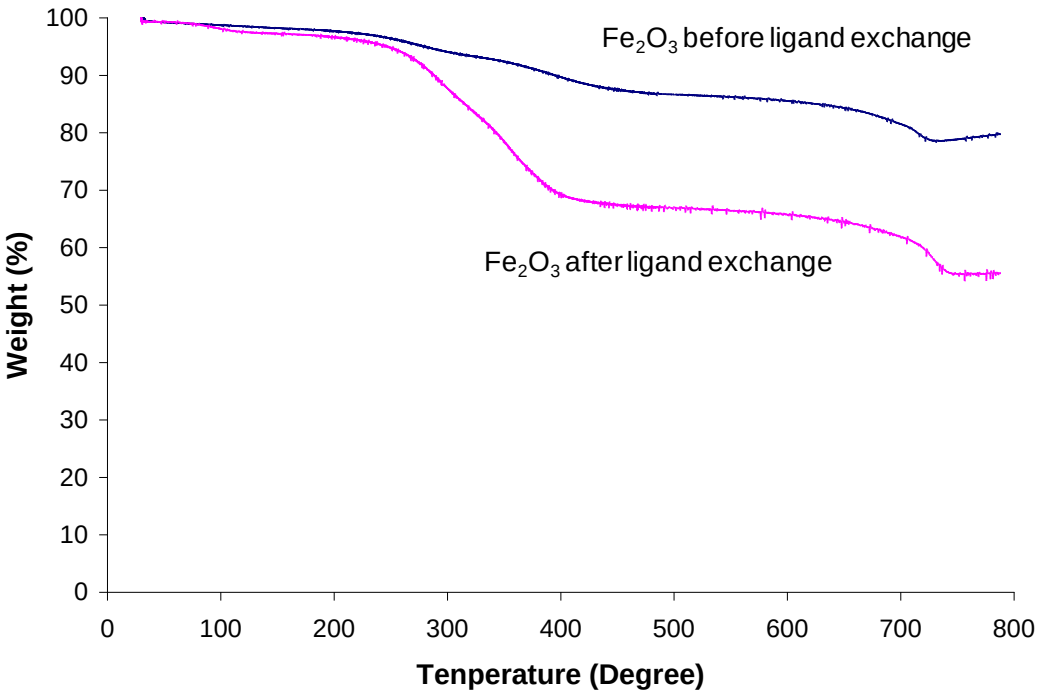

Figure 5.8. TGA curves of the γ-Fe_2O_3 nanoparticles before and after ligand exchange.

Based on the TGA and IR results, and the diameters of the γ-Fe_2O_3 particles, the number of PCEMA-*b*-PAA chains per particle was calculated as 150. Assuming that the density

of the ligand layer was 1.25 g/mL, which is the density of PCEMA-*b*-PAA, the thickness of the ligand layer was calculated as 3.0 nm. This value is a little greater than the root-mean-square end-to-end distance of $PCEMA_{30}$-*b*-PAA_4 (which is calculated to be 1.2 nm as random coil) and is less than its fully stretched length (calculated as 6.8 nm).

5.3.4 Preparation of emulsion spheres with chain segregated surfaces

We studied the chain segregation on the surface of emulsion droplets by using $PCEMA_{55}$-*b*-$PSGMA_{460}$ and $PCEMA_{65}$-*b*-$PGMA_{650}$ as surfactants; and $PCEMA_{320}$ only in the oil phase. In this case, we did not load these spheres with iron oxide, so that we could observe the chain segregation more clearly. The chain segregation is very clear when the concentration of $MgSO_4$ was 0.17 mg/mL. As shown in the TEM image (Figure 5.9), the dark domains on the surface of the emulsion sphere represented the PSGMA domains, which were selectively stained with uranyl acetate, as the electron densities of the PSGMA chains were much higher than those of the unstained PGMA chains.[30] The shells of the spheres were not smooth. The AFM image of the sample (Figure 5.10) also confirmed the bumpiness of the surface of the spheres.

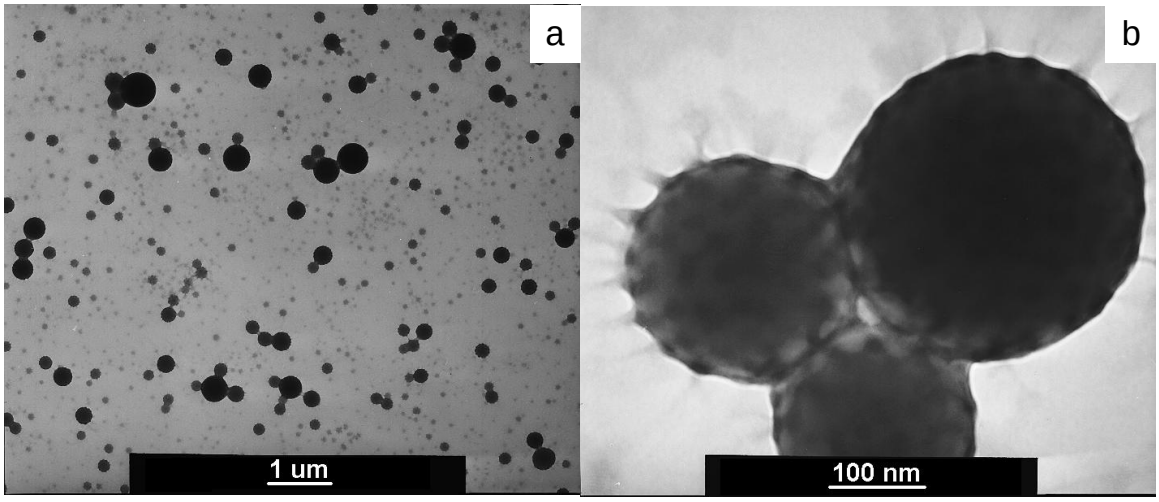

Figure 5.9. TEM images of emulsion spheres without iron oxide loading, shown at (a) low magnification, and (b) High magnification. The sample was stained with uranyl acetate.

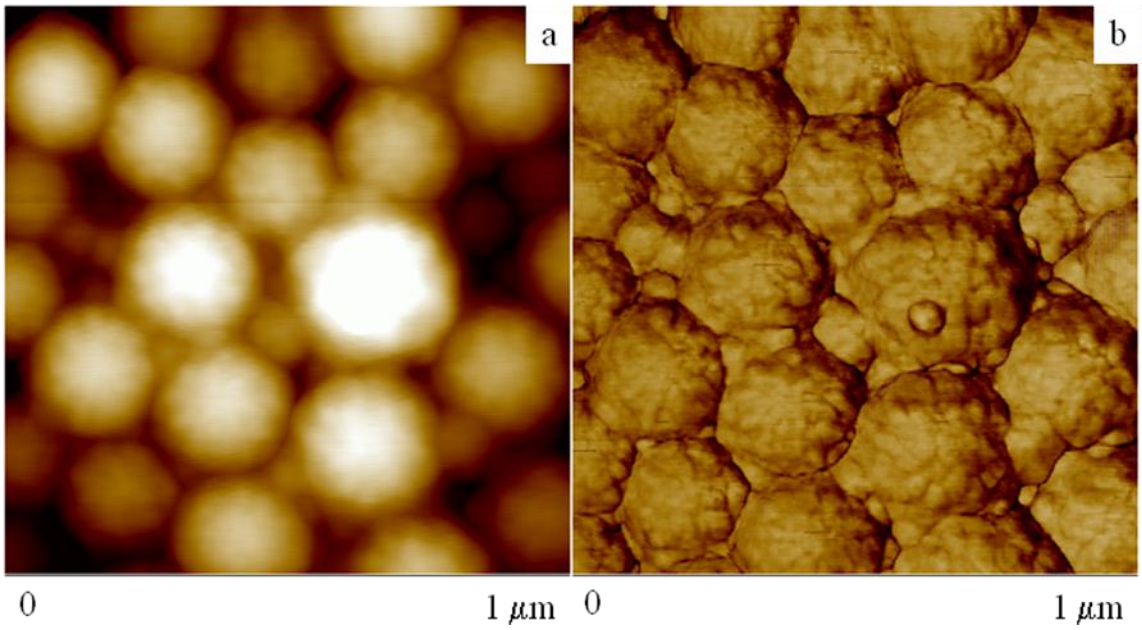

Figure 5.10. AFM images of the emulsion spheres prepared without iron oxide loading. The images shown above include the (a) height image, and (b) phase image.

Generally, the polymeric surfactants stabilized the oil droplets by anchoring their hydrophobic PCEMA blocks into the oil phase, while stretching their hydrophilic chains into the water phase. The anchoring of the surfactants is a rapid process, so that the polymeric surfactants become randomly distributed on the water-oil interface initially. We have previously discussed the incompatibility between different polymer chains, because the mixing entropy is much less than that of small molecules, and the enthalpy of mixing different polymer chains is unfavorable.[31] Due to the incompatibility between the PSGMA and PGMA chains, the two types of polymer chains tend to segregate in order to reduce the total free energy of the system. Since the chloroform in the core phase allowed the polymers to retain some mobility, shuffling of the chain positions on the surface of a droplet, and thus surface chain segregation, was possible with time.

As a polyelectrolyte, PSGMA is negatively charged after becoming ionized in water. The PSGMA chains may repel each other, due to the repulsion between their negative charges. At low ionic strength, the segregation of PSGMA chains from PGMA chains is not favored. The presence of a salt in the water phase could provide electrostatic screening between the negative charges. Zheng *et al.* have discussed the effect of the presence of ions on the segregation between PSGMA and PGMA chains in a similar water-in-oil emulsion process.[11] If the water phase contains enough salt to provide some electrostatic screening effect between the negative charges, the phase segregation between PSGMA and PGMA chains could be observed.

Zheng *et al.* used Cu^{2+} to bridge the two negative charges, so that the chain segregation was enhanced,[11] in a similar manner as was accomplished using Mg^{2+} in this system. In Section 5.3.5.3, we will show that the chain segregations between the two polymer chains could be adjusted by varying the type and concentration of the ions used.

5.3.5 Optimization of the emulsion process and the factors affecting the preparation of magnetic emulsion spheres

In this study, the emulsion process was conducted by adding an oil phase containing iron oxide particles and PCEMA homopolymers into the aqueous phase, under vigorous stirring. In order to optimize the emulsion process, we attempted to adjust the coverage of the iron oxide particles, the weight content of PCEMA homopolymer in the oil phase, the pH value, and the ionic concentration of the water phase. The iron oxide particles used in this study were wustite particles. These were used, since at that stage they were the only kinds of particles available. However, the optimized conditions also worked well with γ-Fe_2O_3 particles. The nature of the nanoparticle core did not affect the emulsion process significantly. The volume of the water phase was 12.0 mL for all of the batches. The polymeric surfactants that were used in 12.0 mL water phase were 5.0 g of $PCEMA_{55}$-*b*-$PGMA_{460}$ and 5.0 g of $PCEMA_{55}$-*b*-$PSGMA_{460}$. The water phase that was used in the emulsion process was pre-saturated with $CHCl_3$, so that the $CHCl_3$ of the oil phase could not dissolve into the water phase once the two phases were mixed. The air present in the emulsion apparatus was also pre-saturated with 0.15 mL of $CHCl_3$. These saturation treatments allowed the volume of the oil phase to be maintained as a constant

before the solvent removal step. Therefore the concentration, viscosity and interfacial tension of the oil phase should not have changed during the droplet broken process. Table 5.3 summarizes the nine batches of emulsion spheres prepared using the different procedures.

Table 5.3. Properties of emulsion spheres prepared under different conditions

Batch	Oil phase			Water phase		Remark
	Wustite particle	$PCEMA_{320}$	$CHCl_3$	pH	Ion	
1 (optimized method)	25.0 mg (ligand exchange)	16.0 mg	0.50 mL	7.0	0.17 mg/mL $MgSO_4$	Completely dispersed
2	25.0 mg (without ligand exchange)	16.0 mg	0.50 mL	7.0	0.17 mg/mL $MgSO_4$	Precipitate
3	25.0 mg (ligand exchange)	0 mg	0.50 mL	7.0	0.17 mg/mL $MgSO_4$	Precipitate
4	25.0 mg (ligand exchange)	16.0 mg	0.50 mL	5.0	0.17 mg/mL $MgSO_4$	Precipitate
5	25.0 mg (ligand exchange)	16.0 mg	0.50 mL	6.0	0.17 mg/mL $MgSO_4$	Some precipitate
6	25.0 mg (ligand exchange)	16.0 mg	0.50 mL	7.0	0.08 mg/mL $MgSO_4$	Completely dispersed
7	25.0 mg (ligand exchange)	16.0 mg	0.50 mL	7.0	0.33 mg/mL $MgSO_4$	Completely dispersed
8	25.0 mg (ligand exchange)	16.0 mg	0.50 mL	7.0	0.67 mg/mL $MgSO_4$	Completely dispersed
9	25.0 mg (ligand exchange)	16.0 mg	0.50 mL	7.0	2.0 mg/mL NaCl	Completely dispersed

5.3.5.1. Oil phase

Our goal was to load the iron oxide particles into the emulsion spheres stabilized with block copolymers containing PCEMA chains as hydrophobic ends. Therefore, the compatibility between the oleic acid ligands, which cover the iron oxide particles and the PCEMA chains, needed to be considered. In a simple solubility test, 2.0 mg of $PCEMA_{320}$ was dissolved in 0.5 mL of chloroform. To this solution, 2.0 mL of oleic acid was added, and the polymer precipitated out of solution immediately. This indicated that oleic acid was not compatible with PCEMA. As a preliminary test (Batch 2), a batch of magnetic emulsion spheres was prepared using iron oxide particles covered with oleic acid, while the other parameters were maintained according to the optimized procedure. Apparently, the resulting emulsion contained many precipitates, and the TEM image (Figure 5.11) indicated that the spheres were not properly stabilized. Therefore, we tried to replace oleic acid with PCEMA-*b*-PAA. This surfactant would stabilize the iron oxide particles with the carboxylic groups and also contact the PCEMA chains of the surfactant with its own PCEMA chains.

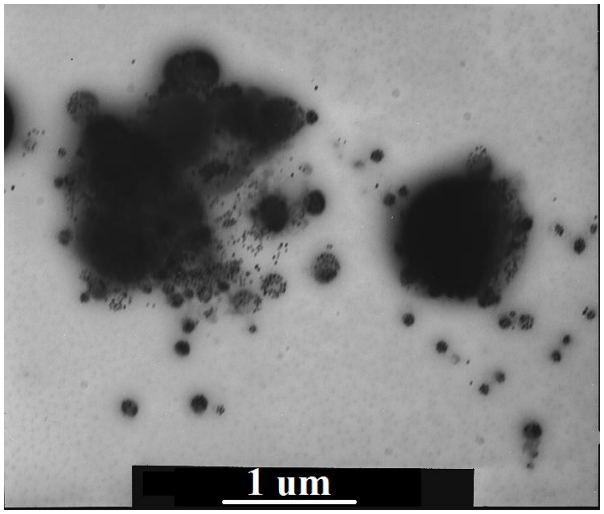

Figure 5.11. TEM image of a sample of Batch 2.

The magnetic properties of emulsion spheres are related to the total content of the iron oxide particles.[32] We also tried to prepare magnetic emulsion spheres with different iron oxide particle content. The emulsion could not be stabilized if the iron oxide particle weight fraction was 100 % (Batch 3). A possible reason for this may be that even though the iron oxide particles were partially covered by PCEMA chains, the PCEMA blocks of the surfactants were not compatible enough with the nanoparticles when there was no PCEMA homopolymer present in the oil phase. The anchoring of surfactants on the surfaces of the oil droplets containing only iron oxide particles was not as favored as it was on the oil droplets containing PCEMA homopolymer. Thus, the oil phase must contain a reasonable amount of PCEMA homopolymer. We attempted to reduce the PCEMA content to 30 wt. %, which led to a noticeable amount of precipitate in the resulting spheres. Thus, in the optimized procedure, we maintained the weight fraction of PCEMA at 39 wt. %.

5.3.5.2 pH value of the aqueous phase

$PCEMA_{55}$-*b*-$PSGMA_{460}$ was used as a surfactant to stabilize the emulsion droplets. The PSGMA block, containing carboxylic groups, becomes a polyelectrolyte if the carboxyl groups are deprotonated. The solubility of this block in water is therefore related to the pH value. Even though a literature pK_a value of PSGMA is not available, a controlled study showed that the PSGMA homopolymer was not soluble in water when the pH value of the solvent is 4.0. The polymer became soluble when the pH value was adjusted above 5.0 with NaOH. Thus, the pH value of the continuous phase is critical for the stabilization of emulsion spheres.

By varying the pH value of the water phase, we prepared emulsion spheres following an identical procedure, using both PGMA and PSGMA as surfactants. When the pH of the water phase was adjusted to 5.0 (Batch 4), the formation of a black precipitate was observed. This indicated that the emulsion droplets were not properly stabilized. At this pH value, even though the polymer had dissolved, it was not sufficiently soluble to stabilize the magnetic particles. We found that in order to stabilize the droplets, the pH value of the water phase had to be adjusted to 7.0 to allow increases of the degree of PSGMA ionization.

5.3.5.3 Ionic strength effect

As discussed in Section 5.3.4, without the loading of iron oxide particles, bumpiness was induced by using $MgSO_4$. This surface bumpiness was verified by TEM images of the PSGMA patches. In this study, we used Mg^{2+} and Na^{+} to adjust the segregation patterns of the chains on the surfaces of the emulsion spheres. Mg^{2+} was chosen because it could provide a bridging effect between carboxylic groups, and it was soluble when the pH value was near 7.0. As shown by TEM images obtained using selective staining of the PSGMA domains by uranyl acetate, the bumpiness of the PSGMA patches can be tuned by varying the types of cations present, as well as the concentration of $MgSO_4$.

When the concentration of the $MgSO_4$ was 0.08 mg/mL or the ratio between Mg^{2+} and the COOH groups was 1.0 : 3.0 (Batch 6, Figure 5.12 a), no significant chain segregation or formation of dark dots on the shell of the spheres was observed. This could be explained if the screening effect provided by the cation was not sufficient to overcome the repulsion between the carboxylic groups. Therefore, chain segregation was not induced in this case. As the concentration of $MgSO_4$ was increased to 0.33 mg/mL, or the ratio between Mg^{2+} and COOH group became 1.3 : 1.0 (Batch 7, Figure 5.12 b), the surface became very bumpy. At this stage, the chain segregation was induced by the screening effect of the cations, while the repulsive interactions between the negative charges were retained, and the chain segregation led to the formation of PSGMA patches. The repulsion between the PSGMA chains restricted the shrinkage of the PSGMA domain area when the volume of the sphere was being reduced, as a consequence the solvent removal step. In order to

maintain the surface area of the PSGMA patches during the volume reduction, the formation of PSGMA bumpiness occurred. As the concentration of $MgSO_4$ was further increased to 0.67 mg/mL, and the ratio between Mg^{2+} and the COOH groups became 2.6 : 1.0 (Batch 8, Figure 5.12 c), the screening effect was so strong that the close packing of PSGMA chains became more favored than when the concentration of $MgSO_4$ was 0.33 mg/mL. The bumpiness became less intense, since the surface area of PSGMA could undergo shrinkage to a greater extent under these conditions. If Na^+ was used (Batch 9, Figure 5.12 d), the cation provided only a screening effect without any bridging effect. As the bridging effect was not present, the bumpiness was not observed, since the PSGMA chains could shrink with increased chain mobility.

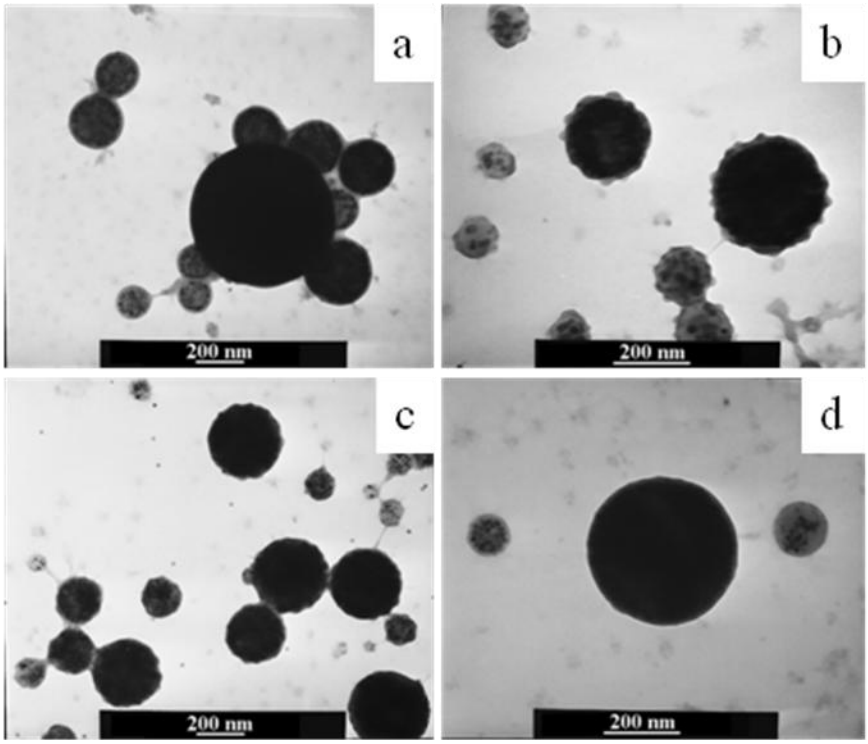

Figure 5.12. TEM images of the magnetic emulsion spheres which were prepared under different ion concentrations: (a) Batch 6, prepared with 0.08 mg/mL of $MgSO_4$, (b) Batch 7, prepared with 0.33 mg/mL of $MgSO_4$, (c) Batch 8, prepared with 0.67 mg/mL of

$MgSO_4$, and (d) Batch 9, prepared with 2.0 mg/mL of NaCl. Samples were exposed to uranyl acetate to selectively stain PSGMA chains.

5.3.5 Preparation of the magnetic spheres

We chose the following procedure as the optimized conditions to prepare magnetic spheres. The aqueous phase contained 12.0 mL of water, 5.0 mg of $PCEMA_{65}$-*b*-$PGMA_{650}$, 5.0 mg of $PCEMA_{55}$-*b*-$PSGMA_{460}$, and 0.17 mg/mL of $MgSO_4$. The pH value of the aqueous phase was adjusted to 7.0. In the oil phase, 16.0 mg of the $PCEMA_{320}$ homopolymer and 22.0 mg of Fe_2O_3 particles that were treated with a ligand exchange process, were dispersed into 0.50 mL of chloroform. The emulsion process was conducted under 1200 rpm stirring at 25 °C. The obtained emulsion (Figure 5.13) was completely dispersed in water.

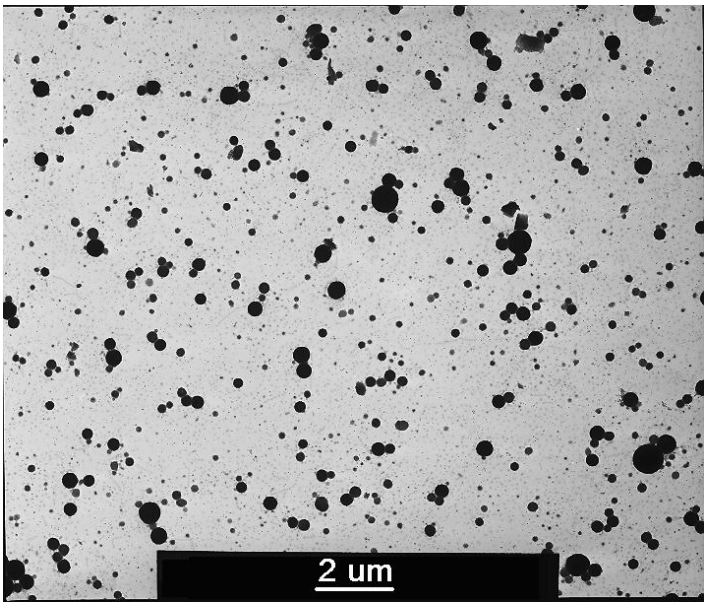

Figure 5.13. TEM image of emulsion spheres obtained using the optimized procedure (Batch 1).

5.3.5.1 Average size of the emulsion spheres before purification

We used both wustite nanoparticles and γ-Fe_2O_3 nanoparticles to prepare emulsion spheres following the optimized procedure. The sizes and the size distributions of the obtained spheres showed little variation. The spheres obtained immediately after the emulsion process were polydispersed in size. As summarized in Table 5.3, from the TEM images, the diameter of the spheres prepared with wustite particles was 280 ± 92 nm, while these values for the spheres made from γ-Fe_2O_3 particles were 294 ± 91 nm. These values were obtained by measuring more than 100 spheres in an image with a magnification of 10,000. We ignored the spheres with diameters of less than 50 nm, which may be the micelles formed by excess amount of surfactant. The encapsulation of single, or a small number of, magnetic nanoparticles in micelles was reported previously.[33] In this study, only emulsion spheres were of interest, because the smaller micelles could not be magnetically captured very quickly. We also analyzed the diameter of the spheres by dynamic light scattering (DLS). The hydrodynamic diameter was measured as 880 nm, which was greater than the result obtained from the TEM measurements. The polydispersity index (PDI) obtained from DLS measurements was 0.14, indicating that the sample was polydisperse. In such a polydisperse sample, larger particles contributed more to the D_h value than the smaller particles.[34] Another possible reason for this behaviour was that the spheres were slightly aggregated.

Table 5.4. Diameter of the emulsion spheres containing wustite and γ-Fe_2O_3 particles.

Emulsion spheres	Diameter obtained from TEM image	DLS data	
		D_h	PDI
With wustite	280 ± 92 nm	880 nm	0.14
With Fe_2O_3	294 ± 91 nm	860 nm	0.14

Since the emulsion spheres obtained using γ-Fe_2O_3 nanoparticles retained much better magnetic properties, in the later sections, the focus will be on the emulsion spheres prepared using γ-Fe_2O_3 nanoparticles. However, the purification procedure, and all of the characterization steps, could also be performed with the spheres prepared using wustite nanoparticles with very good reproducibility.

5.3.5.2 Chain segregation

The PSGMA and PGMA chains on the surface of the emulsion spheres could undergo chain segregation when the concentration of $MgSO_4$ was tuned properly. In this optimized procedure, the concentration of $MgSO_4$ was 0.17 mg/mL. The driving force of the chain segregation was discussed in Section 5.3.4. In this case, we believe that the polymer chains were segregated for the same reason. To study the segregation between the PSGMA chains and the PGMA chains, the sample was stained with uranyl acetate, and observed by TEM (Figure 5.14). The patches formed on the surface of the spheres were not very clear since the core of the sphere was loaded with γ-Fe_2O_3 nanoparticles which have high electron density. The chain segregation was confirmed by an AFM

image (Figure 5.15). As a result of the chain segregation, the surfaces of the sphere were bumpy. These circular bumps could be identified in the height image. In the phase image, the different polymer domains induced different phase angel shifts, leading to the isolated patches distributed on the surfaces of the spheres.

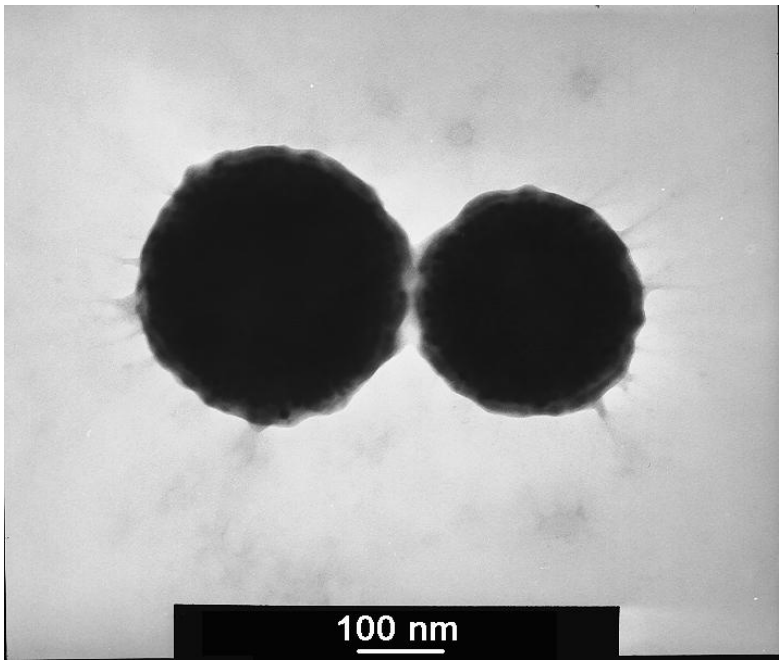

Figure 5.14. High magnification TEM image of the magnetic emulsion spheres obtained with the optimized method. Sample was stained with uranyl acetate.

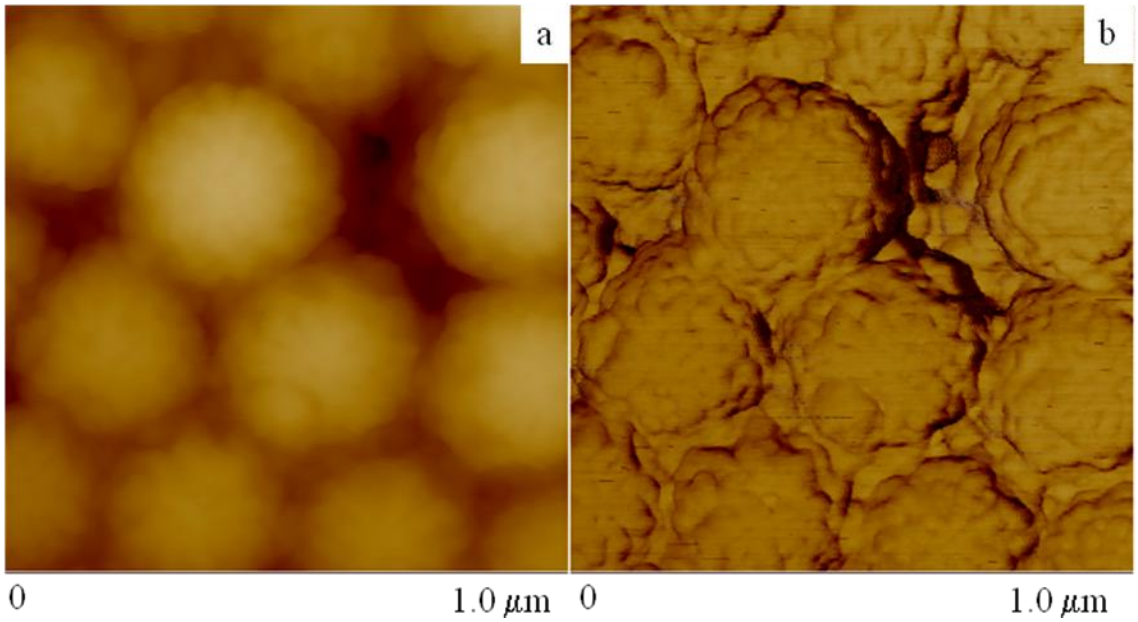

Figure 5.15. AFM phase images of the emulsion spheres obtained using the optimized procedure: (a) height image, and (b) phase image.

5.3.5.3 Crosslinking of the PCEMA chains

After the solvent evaporation step, the obtained emulsion spheres contained a solid core phase, in which the PCEMA blocks from the surfactants were entangled with the PCEMA homopolymer chains. However, the surfactants were not covalently connected with the spheres. In order to fractionate the emulsion spheres, we rinsed the non-crosslinked spheres by magnetic decantation several times. Magnetic decantation involved the dispersion of the emulsion spheres into water, and subsequent magnetic capture of these spheres with a 0.47 T magnet, followed by removal of the water by decantation. The spheres obtained after this process formed aggregates, indicating that some surfactant chains were removed. Moreover, the spheres were intended to be used to immobilize

biomolecules *via* chemical reactions. The structures of the spheres should be chemically locked before all of these treatments are done.

We photo-crosslinked the PCEMA chains to allow the permanent attachment of the surfactants to the spheres.[35] After the emulsion process, the spheres were exposed to a 500 W UV beam. Since the γ-Fe_2O_3 particles have strong absorbance in the UV range, in order to obtain the crosslinking density of PCEMA chains by spectrophotometry, the spheres were treated with HCl to remove the γ-Fe_2O_3 particles. Since PSGMA chains are not soluble under acidic conditions, the spheres were dispersed in a mixture of methanol and THF before HCl treatment. After the removal of Fe(III) ions by dialysis, the polymer residue was analyzed with UV spectroscopy. Before crosslinking, concentration of the polymer in methanol dispersion was measured as 0.091 mg per g of methanol, and the UV absorbance at 282 nm was measured as 0.498. After crosslinking, the concentration of the polymer in methanol dispersion was measured as 0.075 mg/g of methanol, and the UV absorbance was measured as 0.203. The crosslinking density was calculated as 49 %.

5.3.5.4 Purification of the emulsion spheres

The original emulsion spheres obtained immediately after the emulsion process were a polydisperse system. Such a sample contained some micrometer scale spheres, which would readily aggregate and form precipitates. Also, such a sample contained many small spheres and micelles with diameters less than 100 nm, which could not be captured

quickly using a magnet. Therefore, we purified the sample to obtain the spheres within the optimized diameter range, which is near 300 nm.

The emulsion spheres were purified by centrifugation and magnetic decantation, which actually served as a fractionation step. In the centrifugation step, the larger particles were removed by precipitation. In the magnetic decantation step, the micelles and smaller spheres were decanted with the supernatant. The spheres were dispersible in water after a few repetitions of magnetic decantation, indicating that they were properly crosslinked. The TEM image of the purified spheres is shown in Figure 5.16. The average diameter of the spheres was 300 ± 62 nm from the TEM image. A DLS study of this sample revealed that the hydrodynamic diameter of the spheres was 705 nm, with a PDI of 0.09. The D_h value decreased after purification, since the larger spheres were removed. The PDI value also decreased, since the size distribution of the spheres became narrower after purification. The uniform size distribution of the purified emulsion spheres was also verified from the AFM image (Figure 5.17).

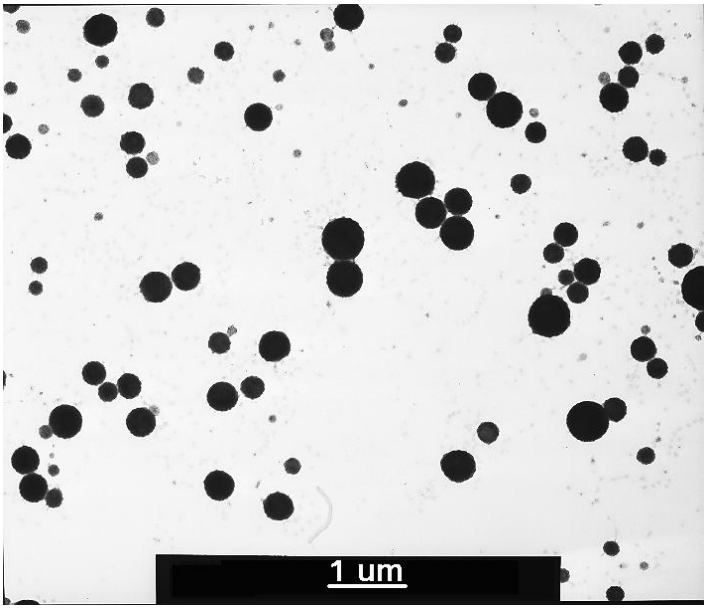

Figure 5.16. TEM image of the purified magnetic emulsion spheres obtained with the optimized procedure.

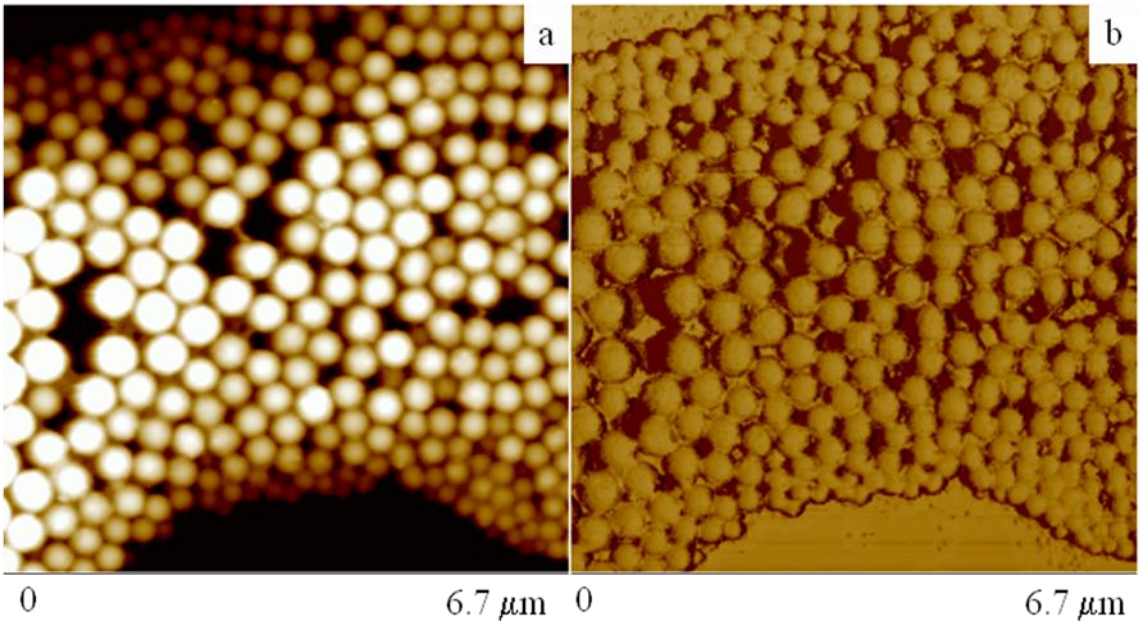

Figure 5.17. AFM images of the purified magnetic emulsion spheres obtained with the optimized procedure: (a) height image, and (b) phase image.

In order to analyze the yield of the preparation process, we dried 1.00 mL of the original emulsion dispersion before purification. The mass of the residue was 3.4 mg. The total volume of the obtained emulsion dispersion was measured as 8.2 mL. Thus, 31 mg of emulsion spheres was obtained after the emulsion process. Liu *et al.* discussed the formation of the emulsion after water-in-oil process using a similar strategy.[10] They suggested that the weight content of the surfactant in the spheres was negligible. The theoretical weight of the product was therefore approximately 38 mg, and the yield of the emulsion process was calculated as 82 %. The weight loss occurred mainly during the oil phase addition step. Since the oil phase was prepared in a glass vial, in order to transfer the oil phase into the flask that used for emulsion process, a syringe was used. A control test showed that after the process of withdrawing 0.50 mL of chloroform into a syringe and transferring it into a pre-weighted vial, approximately 10 % of the weight of the solvent was lost. Another source of weight loss was that some of the dispersion was splashed out of the flask during the oil phase removal step as the mixture was vigorously stirred. After purifying 1.00 mL of this emulsion sample, 2.5 mg of the emulsion spheres was collected. The yield of the purification procedure was calculated as 74 %, and the overall yield was thus 61%.

5.3.5.5 Composition of the emulsion spheres

The composition of the emulsion spheres was studied using TGA (Figure 5.18). Below 450 °C, a 60 % mass loss was observed, which can be assigned to the loss of the organic molecules. The TGA of PCEMA showed that the decomposition of $PCEMA_{320}$ and

PCEMA-*b*-PAA left 3.4 and 3.2 % of remaining residue, respectively. We could assume that the remaining residue of the organic content should be less than 3.4 % of their mass. The remaining residue of the sphere had a weight fraction of 40 %. Therefore, the γ-Fe_2O_3 content should be at least 38 % of the mass of the emulsion spheres. The mass fraction of the γ-Fe_2O_3 core in the γ-Fe_2O_3 particle was measured as 65 %. The oil phase of the emulsion contained 22 mg of γ-Fe_2O_3 particles, and 16 mg of PCEMA. Therefore, the theoretical mass fraction of the γ-Fe_2O_3 should be 38 % of the emulsion sphere. This matches the results from the TGA experiment.

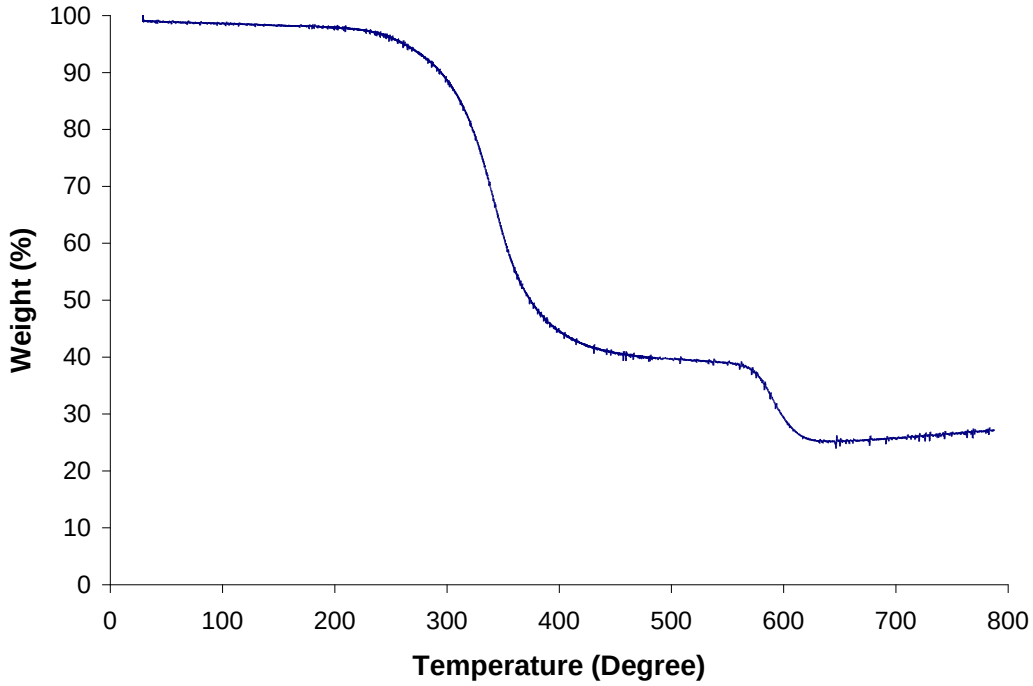

Figure 5.18. TGA curve of the magnetic emulsion spheres after purification.

5.5.5.6 Magnetic properties

The purified emulsion spheres could be captured by a magnetic field. As shown in Figure 5.19, the spheres were completely dispersed into water without the presence of a magnetic field. Once they were placed beside a magnet (0.47 T), the spheres were captured to the side of the glass vial within 1 min. The magnetization curve of the spheres (Figure 5.20) revealed that the spheres are superparamagnetic. The saturation magnetization of the spheres was analyzed to be 19.6 emu/g. Considering the weight content of γ-Fe_2O_3 obtained from the TGA data, which was 38 %, the saturation magnetization of the γ-Fe_2O_3 nanoparticle was calculated to be 52 emu/g. This value is lower than the literature value obtained with bulk γ-Fe_2O_3 (72 emu/g).

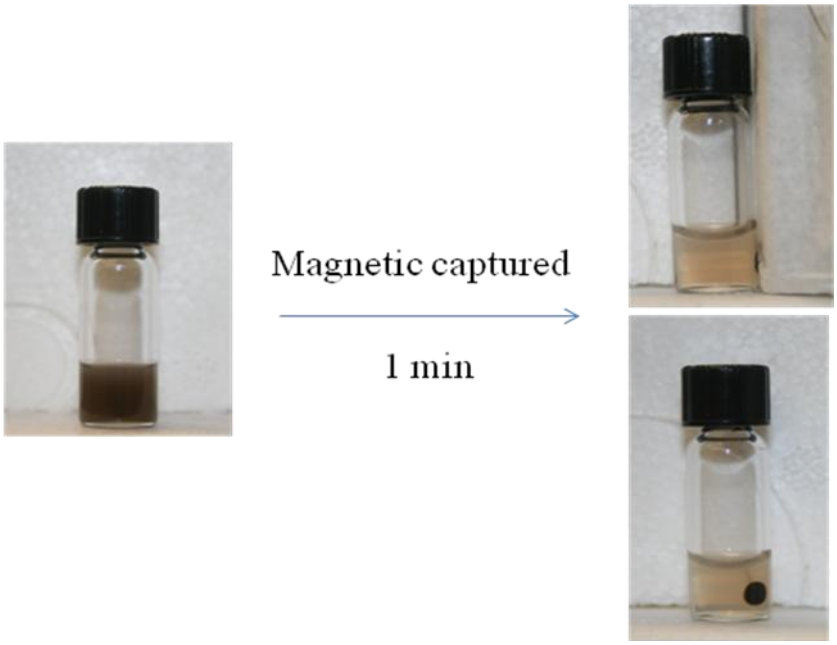

Figure 5.19. Response of the emulsion spheres to the presence of a magnetic field.

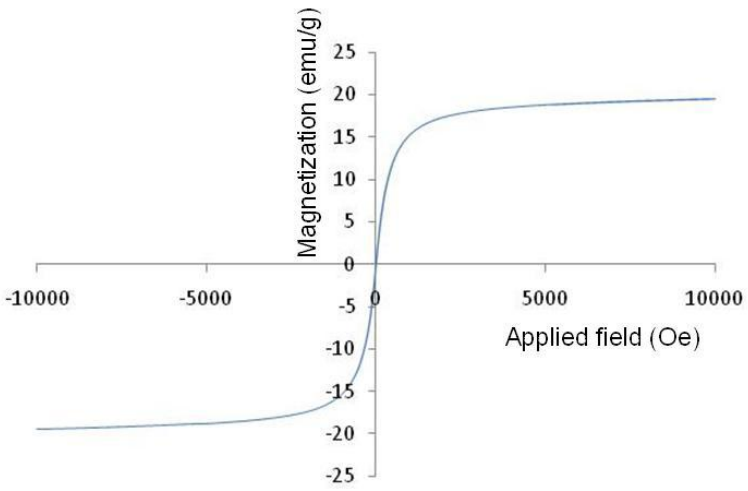

Figure 5.20. Magnetization curve of the magnetic emulsion sphere.

5.3.7 Immobilization of biomolecules

Magnetic beads could be used to capture antibodies from a biological sample, such as urine or blood, if the antigen of the antibody of interest was immobilized onto the beads. Subsequent magnetic capture of the beads would then allow the antibody to be isolated from the sample. Such a preconcentration method is useful for clinical diagnostic applications. The following study was designed to demonstrate that the magnetic spheres that we have prepared could be used for this preconcentration purpose. In this study, a biomolecule was first immobilized onto the magnetic spheres or beads. Subsequently, the modified beads were used to capture the antibody of the biomolecule in solution.

The magnetic emulsion spheres used in this study contained PSGMA chains on their surfaces. The carboxylic groups of the PSGMA chains could be used to immobilize biomolecules, such as proteins. In this study, we used bovine serum albumin (BSA) as a model protein to bind with our spheres. The binding reaction was done in PBS buffer (at pH 7.4) to maintain the bioactivity of BSA molecules. In the presence of EDCI and NHS, the reaction between the carboxylic groups of PSGMA and the amine group from the protein was conducted overnight, producing the BSA-bound spheres (bead-BSA).[36] The excess amount of BSA was washed off by PBS buffer using magnetic decantation.

To quantitatively study the BSA-binding capacity of our spheres, a micro BCA assay was used. This assay was based on a copper colorimetry method that has been applied to analyze proteins for decades.[14] The bead-BSA sample was incubated with BCA reagent at 60 °C. At the same time, a series of BSA standard solutions, and a sample of magnetic spheres without BSA bound to them were treated with BCA reagent following the same procedure. After one hour, the magnetic bead-BSA sample was magnetically captured, and the supernatant was collected. The samples were analyzed by UV spectroscopy, and the results are summarized in Table 5.5. The contribution of the background was then removed from the absorbance obtained with the standard solution, and a calibration curve was plotted. The spheres without BSA attached did not produce significantly different absorbance results when compared to the background control sample. This indicated that the color change of the supernatant was only induced by the BSA that was immobilized onto the spheres. Since the UV absorbance of the BSA-bead sample was too strong (with an absorbance of 2.388), the supernatant of this sample was diluted three-fold. The signal

generated by BSA was obtained by deducting the absorbance measured with 1/3 dilution of the background control. The amount of immobilized BSA was determined by comparing its absorbance with the data in the calibration curve (Figure 5.21), and was calculated as 49 μg. The mass of the bead was measured as 2.2 mg. Therefore, the BSA binding-capacity was calculated as 22 μg of BSA per mg of bead. Commercial Seradyn spheres retain a better capacity, of 100 μg of human serum albumin (molecular weight of 67 kDa) per mg of bead.[37] These Seradyn spheres are covered by a layer of carboxylic groups. Since the outer layer of our beads contained a mixture of PGMA and PSGMA chains, and the PGMA chains were longer than the PSGMA chains, it was reasonable to expect that the capacity of the Seradyn beads would be higher than that of our beads. Commercial Dynal beads have a capacity of 5 - 20 μg of antibody per mg of bead, which is similar to the capacity of our beads.[38]

Table 5.5. Results of BSA immobilization.

Sample	After BCA assay, Abs at 562 nm
Sphere without BSA binding	0.192
BSA standard 0 μg/mL (background control)	0.189
1/3 dilution of BSA standard 0 μg/mL	0.152
BSA standard 5 μg/mL	0.423
BSA standard 10 μg/mL	0.658
BSA standard 20 μg/mL	1.134
1/3 dilution of sphere with BSA binding (Bead-BSA)	0.924

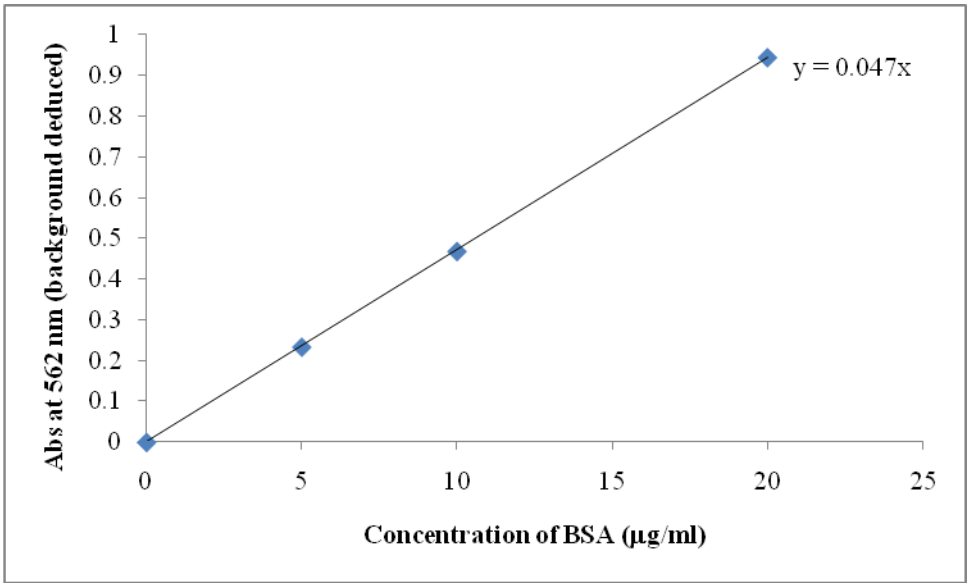

Figure 5.21. Calibration curve of BCA assay prepared with standard BSA solution.

5.3.8 Antibody capturing

The antibody of BSA (anti-BSA) used in this research was conjugated with FITC, a fluorescence dye. The bead-BSA sample (2.2 mg) was incubated with 20 µg of anti-BSA-FITC conjugates in PBS buffer. Since the γ-Fe_2O_3 particles absorb at the emission wavelength (518 nm), the fluorescence intensity of the captured anti-BSA sample could not be observed directly. To analyze the amount of anti-BSA that was captured, we collected the supernatant of the reaction mixture after magnetically capturing the beads. The mixing of the beads that did not contain BSA with the antibody did not cause a significant decrease of the fluorescence intensity of the supernatant. This indicated that the fluorescence intensity decrease observed in the reaction supernatant was only caused by the capturing of antibody with the immobilized BSA. The fluorescence intensity of the supernatant decreased by 75 % after the antibody was captured. The results are

summarized in Table 5.6. The capacity of antibody capturing was calculated as 7 μg of antibody per mg of bead.

Ideally, 22 μg of BSA (molecular weight of 67 kDa) should be able to capture approximately 30 μg of anti-BSA (molecular weight of 150 kDa) when it is dispersed into water, where the movement and orientation of the protein is not restricted. However, when the proteins were immobilized onto the beads, the orientation of the protein was restricted, so that not all of the protein could effectively come into contact with the antibody. This may lead to a low capture efficiency of the anti-BSA. Another possible reason was that the antibody that we used may have been partially denatured. Thus, even if the antibody-capturing capacity of the sphere was higher than 7 μg of antibody per mg of bead, the FITC on the denatured antibody, which was not able to be captured by the antigen, would still generate fluorescence signal in the supernatant after the capturing step.

Table 5.6. Result of anti-BSA capturing.

Sample	Fluorescence intensity at 518 nm
0 μg/mL of anti-BSA-FITC	1500
20 μg/mL of anti-BSA-FITC	18500
Supernatant of the mixture of bead and anti-BSA-FITC	18400
Supernatant of the mixture of bead-BSA and anti-BSA-FITC	6100

The reaction between the magnetic spheres and BSA was based on the reaction between carboxylic acid and amine groups. Since amine groups are common in proteins, the beads

could be readily used to immobilize proteins. The retained bioactivity allowed the immobilized protein to capture its antibody. Therefore, the emulsion spheres could be used to pre-concentrate antibodies for diagnostic applications.

5.4 Conclusions

In this chapter, the preparation of magnetic emulsion spheres bearing segregated surface chains was discussed. Using $PCEMA_{65}$-*b*-$PGMA_{650}$ and $PCEMA_{55}$-*b*-$PSGMA_{460}$ as surfactants in the aqueous phase, and ligand exchanged γ-Fe_2O_3 nanoparticles, $PCEMA_{320}$ homopolymer and chloroform as the oil phase, an oil-in-water emulsion was prepared successfully. Chain segregation between PGMA and PSGMA chains on the surface was tunable, and affected the bumpiness of the surfaces of the spheres. The parameters affecting the emulsion spheres were discussed. Following the optimized procedure, a batch of magnetic emulsion spheres was prepared and characterized. These magnetic emulsion spheres could be used to immobilize biomolecules such as BSA, while the bioactivity of the protein was retained. The BSA-immobilized beads could be further used to capture anti-BSA. This magnetic sphere has potential use in clinical diagnostic applications.

References

1. David Wild *The Immunoassay Handbook 2nd Ed.* Nature Publishing Group, New York, 2001.

2. Denizot, B.; Tanguy, G.; Hindre, F.; Rump, E.; Le Jeune, J. J.; P. Jallet, P.; *J. Colloid InterfaceSci.* **1999**, *209*, 66.

3. Roullier, V.; Grasset, F.; Boulmedais, F.; Artzner, F.; Cador, O.; Marchi-Artzner, V. *Chem. Mater.* **2008**, *20*, 6657.

4. Sutor, J. J. U.S. Patent 5,648,124, 1997.

5. Wang, C. H. J.; Shah, D. O. U.S. Patent 5,395,688, 1995.

6. Omer-Mizrahi, M.; Margel, S. *J. Colloid Interface Sci.* **2009**, *329*, 228.

7. Ugelstad, J.; Ellingsen, T.; Berge, A.; Helgee, O. B. U.S. Patent 4,654,267, 1987.

8. Isojima, T. Su, K. S.; Vander Sande, J. B.; Hatton, T. A. *Langmuir* **2009**, *25*, 8292.

9. Hurak, D. *J. Polym. Sci. Part A Polym. Chem.* **2001**, 39, 3703.

10. Liu, G.; Yang, H.; Zhou, J. *Biomacromolecules* **2005**, *6*, 1280.

11. Zheng, R.; Liu, G.; Yan, X. *J. Am. Chem. Soc.* **2005**, *127*, 15358.

12. Yan, X.; Liu, G.; Haeussler, M., Tang, B. Z. *Chem. Mater.* **2005**, *17*, 6053.

13. Park. J.; An, K.; Hwang, Y.; Park, J.; Noh, H.; Kim, J.; Park, J.; Hwang, N.; Hyeon, T. *Nat. Mater.* **2004**, *3*, 891.

14. Smith, P. K.; Krohn, R. I.; Hermanson, G. T.; Mallia, A. K.; Gartner, F. H.; Provenzano, M. D.; Fujimoto, E. K.; Geoke, N. M.; Olson, B. J.; Klenk, D. C. *Anal. Biochem.* **1985**, *1502*, 76.

15. Jeong, U.; Teng, X.; Wang, Y.; Yang, H.; Xia, Y. *Adv. Mater.* **2007**, *19*, 33.

16. Cornell, R. M.; Schwertman, U. *The Iron Oxides, Wiley-VCH,* Weinheim, 2003.

17. Gheisari, M.; Mozaffari, M.; Acet, M.; Amighian, J. *J. Magn. Magn. Mater.* **2008**, *320*, 2618.

18. Kwon, S. G.; Piao, Y.; Park, J.; Angappane, S.; Jo, Y.; Hwang, N.; Park, J.; Hyeon, T. *J. Am. Chem. Soc.* **2007**, *129*, 12571.

19. Bronstein, L. M.; Huang, X.; Returm, J.; Schmucker, A.; Pink, M.; Stein, B. D.; Dragnea, B. *Chem. Mater.* **2007**, *19*, 3624.

20. Bodnarchuk, M. I.; Kovalenko, M. V.; Groiss, H.; Resel, R.; Reissner, M.; Hesser, G.; Lechner, R. T.; Steiner, W.; Schaffler, F.; Heiss, W. *Small* **2009**, *5*, 2247.

21. Kim, D.; Lee, N.; Park, M.; Kim, B. H.; An, K.; Hyeon, T. *J. Am. Chem. Soc.* **2009**, *131*, 454.

22. Hyeon, T.; Lee, S. S.; Park, J.; Chung, Y.; Na, H. B. *J. Am. Chem. Soc.* **2001**, *123*, 12798.

23. Wang, X.; Dykstra, T. E.; Salvador, M. R.; Manners, I.; Scholes, G. D.; Winnik, M. A. *J. Am. Chem. Soc.* **2004**, *126*, 7784.

24. Milner, S. T. *Science*, **1991**, *251*, 905.

25. Zhou, J.; Li, Z.; Liu, G. Macromolecules **2002**, *35*, 3690.

26. Zhang, L.; He, R.; Gu, H. *Appl. Surf. Sci.* **2006**, *253*, 2611.

27. Park. J.; An, K.; Hwang, Y.; Park, J.; Noh, H.; Kim, J.; Park, J.; Hwang, N.; Hyeon, T. *Nat. Mater.* **2004**, *3*, 891.

28. Yan, F.; Li, J.; Zhang, J.; Liu, F.; Yang, W. *J. Nanopart. Res.* **2009**, *11*, 289.

29. Ayyappan, S.; Gnanaprakash, G.; Panneerselvam, G.; Antony, M. P.; Philip, J. *J. Phys. Chem. C* **2008**, *112*, 18376.

30. Zhou, Z.; Liu, G.; Han, D. *ACS Nano* **2009,** *3***,** 165**.**

31. Bates, F. S.; Fredrickson, G. H. *Phys. Today* **1999**, *52*, 32.

32. Zheng, W.; Gao, F.; Gu, H. J. Magn. Magn. Mater. **2005**, 288, 403.

33. Bronstein, L. M.; Kostylev, M.; Shtykova, E.; Vlahu, T.; Huang, X.; Stein, B. D.; Bykov, A.; Remmes, N. B.; Baxter, D. V.; Svergun, D. I. *Langmuir* **2008**, *24*, 12618.

34. Pecora, R. Ed. *Dynamic Light Scattering; Application of photon Correlation Spectroscopy* Plenum: New York, 1985.

35. Hess, P. H.; Parker, P. H. *J. Appl. Polym. Sci.* **1966,** *10*, 1915.

36. Qiu, X.; Liu, G. *Polymer* **2004**, *45*, 7203.

37. Seradyn operation manual from website:
http://www.seradyn.com/technical/pdf/MGCMTN.pdf

38. Dynal beads operation manual from website:
http://tools.invitrogen.com/content/sfs/manuals/143%2011D_Rev000.pdf

Chapter 6

Conclusions and comments on possible future research

6.1 Brief conclusion

In this thesis, hybrid materials of block copolymers and magnetic nanoparticles were prepared for either fundamental research or application considerations.

This study began with a morphological analysis of nanoaggregates formed by PGMA-*b*-PCEMA-*b*-P*t*BA triblock copolymers which had different molecular compositions. Different morphologies of the nanoaggregates were obtained from different preparation procedures. More importantly, after the P*t*BA core block was sculptured into PAA, the triblock copolymer cylindrical aggregates could have been used as a template for nanoparticle growth, which is a common method for the preparation of polymer/nanoparticle hybrid materials. The swelling of the cylindrical aggregates in water/DN mixtures resulted in expansions of the PtBA core and thereafter the size of PAA cavity after PtBA hydrolysis. This could enhance the capacity of the aggregates for implanted nanoparticle uptake. This study indicated that the morphology and size of the

polymer template could be modified to improve and change the nanoparticle growth patterns. These modifications could be accomplished by changing the morphology of the nanoaggregates using the typical micelle formation techniques, or by further treating the obtained nanoaggregates. The latter case could be understood as the template of nanoparticle growth was obtained by treating a previously prepared polymer template.

It was also demonstrated that polymer/nanoparticle hybrid materials could be obtained by an alternative method. This was done by using cobalt particle self-assembly, induced by dipolar interactions, as a template to build polymers onto. The use of polymer templates allows nanoparticles to grow in the template in a particular way, based on the morphology of the polymer template. Meanwhile, using nanoparticles as templates allows the polymers to follow the arrangement of the nanoparticles. The cobalt nanowires were prepared by coating a diblock copolymer layer onto the existing cobalt nanoparticle chains in the presence of a block selective solvent. The results demonstrated that the coating of the polymer layer onto the cobalt chains did not change the distance between the cobalt nanoparticles. This indicated that the coating process was a physical absorption, while the structure of the cobalt chain template remained unchanged. The following photo-crosslinking of the polymer coating locked the dipolar structure of the nanoparticles in place. This procedure should provide a general method for permanently locking dipolar structures formed by magnetic nanocrystals of various compositions, sizes and shapes. The magnetic nanowires that we have prepared may have potential applications in the development of complex nano-devices that can respond to a magnetic field.

Magnetic emulsion spheres were prepared for clinical diagnostic applications, in which the spheres could be used to pre-concentrate antibodies or antigens in a complex sample mixture. The oil-in-water emulsion process was a mixing step, in which the magnetic γ-Fe_2O_3 nanoparticles were loaded into the core of emulsion droplet in the presence of surfactant. This one-pot recipe provided a facile method to prepare polymer/nanoparticle hybrid materials without further consideration of the morphology. Moreover, surface chain segregation could be introduced onto the surface of the emulsion spheres by using two types of diblock copolymer surfactants bearing different hydrophilic segments. This has lead to the formation of bumpy surfaces on the spheres. The magnetic emulsion spheres prepared could be easily captured by an external magnetic field. The beads could also be used to covalently immobilize a protein sample (such as BSA) without affecting its bioactivity. The immobilized protein could then be used to capture its antibody from a biological sample. These properties allow the emulsion spheres that we have prepared to be useful in immunoassays.

The preparation of polymer/nanoparticle composite materials required the nanoparticles to be covered by a block copolymer layer. The one-pot synthesis of cobalt nanoparticles with a block copolymer layer was therefore studied as a preliminary research project. The cobalt nanoparticles were synthesized by thermally decomposing $Co_2(CO)_8$ in the presence of PEG-*b*-PAA as a polymeric multi-dentate ligand. The factors affecting the size and size distribution of the cobalt nanoparticles were studied. In order to control the

size of the nanoparticles, a double injection procedure was used. Dipolar structures were obtained with the cobalt nanoparticles. This study provided a method to synthesize nanoparticle templates for the preparation of cobalt nanowire. The γ-Fe_2O_3 nanoparticles were synthesized by thermally decomposing $Fe(Oleate)_3$. The obtained nanoparticles were covered with oleic acid, a small molecular ligand. In order to introduce a polymer layer onto the surface of the nanoparticle, a ligand exchange process was used, where the polymer was exchanged with the oleic acid. This procedure yielded γ-Fe_2O_3 nanoparticles with sufficient polymer coverage.

6.2 Future research

6.2.1 Facile preparation of γ-Fe_2O_3 nanoparticles using PCEMA-*b*-PAA ligands

The synthesis of PCEMA-covered Co nanoparticles was conducted using a one-pot synthesis method, in which the formation of the Co nanoparticles was performed in the presence of PCEMA-*b*-PAA surfactant. However, in order to prepare PCEMA covered γ-Fe_2O_3 nanoparticle for the emulsion project, a two-step procedure was used. After the preparation of γ-Fe_2O_3 nanoparticles covered with oleic acid, a ligand exchange process was applied to introduce PCEMA-*b*-PAA onto the surface of the nanoparticles. The ligand exchange process required a large excess of the ligand with respect to the nanoparticle (with a 2:1 weight ratio of the ligands to the nanoparticles) compared with the one-pot recipe (with a 3:1 weight ratio of the ligands to the cobalt nanoparticles). In

order to use a smaller amount of diblock copolymer ligand, it should be better to prepare γ-Fe_2O_3 nanoparticles using PCEMA-*b*-PAA as the surfacant with a similar one-pot method. However, to prepare uniform particles, the thermal annealing of the nanoparticles should be done above 300 °C.[Based on the results of our TGA analysis, PCEMA-*b*-PAA was not stable at this temperature. Moreover, most of the solvents with high boiling points are non-polar, so that PCEMA is not soluble in those solvents. We have attempted to prepare the Fe_3O_4 nanoparticles in the presence of PCEMA-*b*-PAA using a one-pot recipe. However, due to the two reasons mentioned above, this preparation was not successful.

Here I wish to propose a facile method for the preparation of γ-Fe_2O_3 particles that are covered by a PCEMA-*b*-PAA diblock copolymer ligand. Hyeon *et al.* and Alivisatos *et al.* have prepared γ-Fe_2O_3 nanoparticles using similar two step procedures.[2,3] The γ-Fe_2O_3 nanoparticles were produced by controlled oxidation of Fe nanoparticles. The Fe nanoparticles were prepared by thermally decomposing $Fe(CO)_5$ precursor at a temperature lower than 180 °C. In Chapter 4 and the Appendix, it was shown that cobalt nanoparticles were prepared by thermally decomposing $Co_2(CO)_8$ at 180 °C in the presence of PCEMA-*b*-PAA. Therefore, it should also be possible to prepare Fe nanoparticles by the thermal decomposition of $Fe(CO)_5$ in the presence of the same surfactant. We have demonstrated that the Fe_3O_4/wustite nanoparticles were oxidized to yield γ-Fe_2O_3 nanoparticles by trimethylamine oxide. After the formation of the Fe nanoparticles, which would be covered by PCEMA, we could use the same reagent to

convert Fe particles into γ-Fe_2O_3 particles. The sample could then be purified to remove the low boiling point solvent. Hyeon reported the formation of γ-Fe_2O_3 phase from amorphous Fe_2O_3 phase under 280 °C. Therefore, if the sample is mixed with a high boiling point solvent, such as octyl ether (with a boiling point of 280 °C), γ-Fe_2O_3 nanoparticles covered by PCEMA-*b*-PAA would be produced after a reasonable annealing process. In this recipe, the amount of PCEMA-*b*-PAA used (40 mg of polymer per 100 mg of nanoparticle) should be one fifth of that which was used in the ligand exchange process (200 mg of polymer per 100 mg of nanoparticles). It should be possible to tune the size of the nanoparticles during the formation of the Fe nanoparticles. Also, this method could be used in large scale synthesis, such as at a gram scale. If the obtained nanoparticles are anisotropic in shape, or the sizes of the particles are large enough to initiate dipolar interactions, we could use a similar recipe to that discussed in Chapter 4 to coat block copolymers onto this γ-Fe_2O_3 template. Since γ-Fe_2O_3 is stable in air, the composite materials formed from these nanoparticles should have a wide variety of potential applications.

6.2.2 Demonstration of the binding selectivity of the emulsion spheres with biomolecules

The emulsion spheres discussed in Chapter 5 contained segregated polymer chains on their surfaces. We found that the chain segregation could be adjusted by varying the type of ions that were present, and also their concentration. Therefore the size of the PSGMA patches containing carboxylic groups could also be tuned. The PSGMA patches have

fewer repeat units than the PGMA chains which surround them. The PGMA and PSGMA chains should stretch out towards the disperse phase (water), due to the formation of a polymer brush by the surface polymer chains. Therefore, there is a possibility that the PSGMA patches form holes in the PGMA plateaus. Any sample that will bind on the PSGMA chains must firstly penetrate through the channel of PGMA chains. The size of the PGMA channel provides selectivity for the capture and immobilization of biomolecules.

If emulsion spheres with this conformation could be prepared (it could be prepared by using NaCl or high $MgSO_4$ concentrations, according to the systematic study of emulsions in Chapter 5), a simple experiment could be conducted to demonstrate the selectivity of these spheres. BSA has a hydrodynamic diameter of approximately 7 nm when the pH value is 7.[4] If the diameter of the PSGMA patches is much lower than this value, such as 5 nm, the ability of these spheres to bind to BSA should decrease dramatically when compared to the binding ability of the spheres reported in Chapter 5. A series of emulsion spheres with different chain segregation patterns should be prepared accordingly, and the binding capacity of BSA with the different spheres could be compared. These results would show whether the binding selectivities of the spheres could be tuned by varying the chain segregation patterns.

A more advanced study could show that the non-specific binding interactions were overcome, during the antigen immobilization and the antibody capture processes, by the

shielding effect of the PGMA chains. There are two possible types of non-specific binding sources. The first type involves the binding between antibodies and the undesired sites on the sphere, rather than the desired antigens. These sites include carboxylic groups of PSGMA chains, and hydrophobic core, if the anti-antibody is sufficiently small. The second type of binding occurs between the pre-immobilized antigens on the sphere and the impurities in the sample containing the antibodies. We will demonstrate that our spheres could display reductions of non-specific binding caused by both of these sources.

While analyzing the non-specific interactions of a sandwich-type immunoassay, Jenkins *et al.* sandwiched an antibody by the pre-immobilized antigen on the solid phase, and an enzyme conjugate which could generate signal for detection.[5] The non-specific binding between the enzyme conjugate and the pre-immobilized antigen was demonstrated by incubating the solid phase, on which antigens were immobilized, and the enzyme conjugated without involving antibody samples. The results revealed that this kind of non-specific binding accounted for 80% of the total background signal caused by all types of non-specific binding. A similar process could be applied to demonstrate the reduction of nonspecific binding between the antibodies and the spheres. Without the antigens attached, the spheres would be incubated with radioactively labeled antibodies. The radioactive signals generated from the spheres incorporating the PGMA shielding effect which were incubated with the antibodies would be compared with the signals generated from similar spheres which were not incubated with antibodies. If non-specific interactions occur, the signals from the two types of spheres should show significant differences. We could also prepare emulsion spheres which are covered by PSGMA

chains only, and repeat this incubation. Without PGMA chains, the non-specific binding would be more extensive, so that the signals from the samples with or without incubation will show greater differences.

A possible method to determine the extent of the non-specific binding between the immobilized antigens on the spheres and impurities in the samples is based on a competitive process. Datta *et al.* evaluated the interference of non-specific binding of impurities in an analyte sample by spiking hemolysate, bilirubin and triglyceride into a serum sample containing the antigen analyte.[6] The concentration of the antigen was tested separately using samples that were spiked with interference molecules, and those which were not spiked. A *t*-test was then performed on the results from the spiked samples and their unspiked controls, to determine the significance of these nonspecific interactions. A similar method could be used to demonstrate the reduction of non-specific binding, by preparing a series of samples containing analyte mixed with different interference molecules. The control test would observe binding between samples of pure analytes (lacking interference molecules) and the spheres, and would compare the results obtained for the spheres bearing chain-segregated surfaces with those obtained for the spheres which had surfaces composed of PSGMA. Similar tests would then be carried out using the samples which contained the intereference molecules. The concentration of the analyte in the interference samples would be analyzed for the two types of spheres. The results obtained from the PSGMA surface spheres would be compared by a *t*-test in order to determine the significance of the non-specific interactions both types of spheres. The effect of the interference molecules should be more significant for the spheres which

lacked chain-segregation. If the results obtained from the surface-chains segregated spheres show reduced significance from a *t*-test, we may determine the extent of the reduction of non-specific binding between the spheres and the samples.

References

1. Kwon, S. G.; Piao, Y.; Park, J.; Angappane, S.; Jo, Y.; Hwang, N.; Park, J.; Hyeon, T. *J. Am. Chem. Soc.* **2007**, *129*, 12571.

2. Hyeon, T.; Lee, S. S.; Park, J.; Chung, Y.; Na, H. B. *J. Am. Chem. Soc.* **2001**, *123*, 12798.

3. Casula, M. F.; Jun, Y. W.; Zaziski, D. J.; Chan, E. M.; Corrias, A.; Alivisatos, A. P. *J. Am. Chem. Soc.* **2006**, *128*, 1675.

4. Kun, R.; Szekeres, M.; Dekany, I. J. *Therm. Anal. Calorim.* **2009**, *96*, 1009.

5. Jenkins, S. H., Heineman, W. R.; Hasall, H. B. *Anal. Biochem.* **1988**, *168*, 292.

6. Datta, P.; Dasgupta, A. *J. Clin. Lab. Anal.* **2003**, *17*, 174.

Appendix 1

Synthesis of cobalt nanoparticles in the presence of poly(ethylene glycol)-*b*-poly(acrylic acid) surfactant

A-1 Brief introduction

For the past few decades, novel synthesis methods have been developed to produce monodisperse magnetic nanoparticles (NPs) made of materials such as iron oxide, cobalt, and nickel, for example.[1] The nanometer scale of magnetic NPs allow these particles to exhibit superparamagnetic properties, such as being captured by a magnetic field and then re-dispersing after the removal of the magnetic field. These kinds of magnetic nanoparticles have been used in immunoassays, [2] site-specific drug delivery systems,[3] for data storage[4], and as catalysts.[5] Small molecular surfactants, such as trioctylphosphine oxide (TOPO), oleic acid, and amines, were developed to produce magnetic nanoparticles with well-controlled size distributions.[6] In addition to spherical particles, magnetic nanocrystals with various morphologies, such as rods, cubes and disks, have also been prepared in the presence of low molecular weight surfactants.[7]

These magnetic NPs could be modified by introducing a polymer layer onto their surfaces. Many interesting properties could be provided by the addition of the versatile functional groups on polymer chains. Furthermore, polymer coated magnetic NPs could be used to form hybrid with block copolymers in order to construct more complex morphologies.[8] There are many procedures available to introduce a polymer coating onto magnetic NPs. Small molecular surfactants could be replaced by polymer surfactants via a ligand exchange process.[9] Polymerization could be initiated by the functional groups on the NPs in order to grow polymer layers.[10,11] This has been discussed in the literature review section (chapter 1) of this thesis.

Cobalt nanoparticles are of great interest, because of their high saturation magnetization, which allows them to have strong magnetic response. There are two methods available to synthesize cobalt nanoparticles. The first method involves the reduction of Co^{2+} using a reductant in the presence of a surfactant and co-surfactant.[12] Meanwhile, the second method involves the high temperature decomposition of a Co(0) precursor, such as $Co_2(CO)_8$, in the presence of a surfactant (for example, oleic acid) and a co-surfactant (such as TOPO).[13] The surfactants were used to regulate the growth of these nanoparticles, and to render colloidal stability of the final Co nanoparticles. TOPO, which binds reversibly to Co, was used mainly to narrow the particle size distribution. In both of the two procedures, cobalt was first generated as a monomer by either a reduction reaction, or thermolysis of $Co_2(CO)_8$. The monomers formed nuclei, or seeds, which were stabilized by the surfactant when the concentration of the monomers became

supersaturated. These nuclei grow by absorbing the monomers while surfactants adhered to and detached from the surface of the nuclei as it reached equilibrium.

Our group reported a one-pot synthesis of cobalt NPs using polystyrene-*b*-poly(acrylic acid) (PS-*b*-PAA),[14] which is a polydentate polymeric surfactant stabilizing the crystal core with acrylic acid. The synthesis followed the reduction procedure. Compared with the small molecular surfactants or monodentate surfactants, the polydentate surfactants were absorbed much more strongly onto the cobalt crystal. It was reported that the cobalt particles covered by the polydentate PS-*b*-PAA surfactant remained dispersible in THF after being rinsed five times with THF, while the TOP-stabilized cobalt particles precipitated from solution after being rinsed only onc with THF. Random copolymers,[14] block copolymers,[15] and end-functionalized copolymers[16] have also been used as surfactants.

Pyun *et al*. synthesized mono size dispersed cobalt particles in the presence of the end-functionized polystyrene surfactants.[16,17] The polymeric surfactant they were using was, in fact, a monodentate functional group attached on a polymer chain. The synthesis of this nanoparticle followed a thermal decomposition recipe. However, there are very few reports of the preparation of cobalt nanoparticles using polydentate polymeric surfactant via the thermal decomposition procedure.

In this section, I will discuss the preparation of cobalt nanoparticles by the thermal decomposition method using poly(ethylene glycol)-*b*-poly(acrylic acid) as the surfactant. This work was done as a preliminary study for the cobalt wire project, which is discussed in Chapter 4. Poly(ethylene glycol) (PEG) was chosen, because it is commercially available, and it is also dispersible in many solvents. Some parameters affecting the size and size distribution of the cobalt particles were studied. These parameters include the concentration of the monomer, the ratio between carboxylic group and the monomer, and the injection technique of the precursor.

A-2 Experimental

Preparation of PEG-*b*-P*t*BA via ATRP. The PEG_{113} macro-initiator, containing a bromine endgroup, was provided by Dr. Yu Fu. In a typical polymerization, 1.0 g (0.2 mmol) of PEG_{113} macro-initiator was charged into a 50 ml flask. The flask was sealed by septa and vacuum dried at 120 °C for 12 hours. After the flask was recharged with nitrogen and cooled down, 143.5 mg (1 mmol) of CuBr and 22.4 mg (0.1 mmol) of $CuBr_2$ was added into the flask with nitrogen purging. The flask was then vacuum-thawed three times. 2 mL of freshly distilled toluene and 0.58 mL (4 mmol) of freshly vacuum-distilled *t*BA were transferred into the flask by syringes. After the mixture was fully dissolved, 0.22 mL (1 mmol) of PMDETA was added to start the reaction. The mixture was stirred at 80 °C for 16 hours until a 60% conversion rate of the monomer was achieved. The reaction was terminated by removing the heat, and the addition of THF.

The polymer solution was pushed through an alumina column in order to remove the catalysts. Finally, the polymer was precipitated from ether.

Hydrolysis of P*t*BA into PAA. The P*t*BA block was hydrolyzed into PAA in the presence of TFA. A typical hydrolysis reaction involves dissolving 250 mg (0.033 mmol, or 12 units of *t*BA) of the PEG-*b*-P*t*BA copolymer into 2.8 mL of CH_2Cl_2. Finally, 51 μL (2 mmol, or a five-fold excess with respect to the *t*BA units) of triethylsilane and 1.2 mL of TFA were added into the flask to start the reaction. This mixture was stirred for 2 hours before 10 mL of ether was added to precipitate it. The precipitate was redissolved into dichloromethane and precipitated with ether three more times.

Distillation of dichlorobenzene (DCB). In order to remove trace amounts of water and other impurities, DCB (200 mL) was washed with H_2SO_4 (98%, 30 mL). The DCB phase was then washed with 50 ml of water six times. The obtained DCB was dried by mixing with $CaCl_2$ overnight. The resulting DCB was then stirred with CaH_2 at 60 °C for 24 hours, before it was distilled under vacuum.

Preparation of the $Co_2(CO)_8$ solution. In a glovebox, 500 mg of $Co_2(CO)_8$ was transferred into a 25 mL round bottom flask under a nitrogen environment. The flask was sealed inside the glovebox immediately. After the flask was removed from the glovebox, 5 mL of the freshly distilled DCB was transferred into the flask by syringe. The mixture

was vortexed for 10 min in order to allow the $Co_2(CO)_8$ to become dissolved. The concentration of the solution is 100 mg/mL.

Preparation of the Co nanoparticles by single injection. In a typical preparation, PEG_{114}-*b*-PAA_8 (27.5 mg, 0.0049 mmol of the polymer, or 0.039 mmol of AA group) and TOPO (4.5 mg, 0.012 mmol) were added into a 50 mL three-necked round bottom flask as the surfactants. After the flask was purged with a vacuum and refilled with nitrogen three times, 3 mL of freshly distilled DCB was added with a syringe. The surfactant solution was heated to 180 °C by an oil bath. At this temperature, 1 mL of the $Co_2(CO)_8$ solution (100 mg/mL) was injected rapidly. After the mixture was stirred for 5 min, the reaction flask was removed from the oil bath.

Preparation of the Co nanoparticles by double injection. The preparation of the nanoparticles followed the size-focusing method. A second injection of $Co_2(CO)_8$ solution was applied in order to decrease the size distribution of the Co particles, as well as to increase the sizes of the particles. In a typical preparation, PEG_{114}-*b*-PAA_8 (27.5 mg, 0.0049 mmol of the polymer and thus 0.039 mmol of the AA groups) and TOPO (4.5 mg, 0.012 mmol) were added into a 50 ml three-necked round bottom flask as the surfactants. After the mixture was evacuated with a vacuum and refilled with nitrogen three times, 3 mL of freshly distilled DCB was added through a syringe. The surfactant solution was heated to 180 °C by an oil bath. At this temperature, 1 mL of the $Co_2(CO)_8$ solution (100 mg/mL) was injected rapidly. After the mixture was stirred for 2 min, another 1 mL of

the $Co_2(CO)_8$ solution was quickly injected. After the reaction mixture was stirred for 10 min, the reaction flask was removed from the oil bath.

Polymer Characterization. GPC analysis was carried out at 25 °C on a Waters 515 system, equipped with three columns (Waters Styragel HR5E, Waters Styragel HR4E and μStyragel 500 Å), and a differential refractometer (Waters 2410). THF was used as the eluant for the GPC analysis, and the system was calibrated using monodisperse PS standards. ^{1}H NMR spectra were recorded on a Bruker Avance 300 MHz spectrometer, using D_2O as the solvent.

Size measurement. The TEM images of the Co particles were scanned into tiff files. SimplePCI software was used to measure the diameters of the particles. Microsoft Excel was used to calculate the average size and the size standard deviation (STD).

A-3 Results and discussion

A-3.1 Polymer characterization

The precursors of the polymeric surfactants, PEG-*b*-P*t*BA were synthesized via atom transfer radical polymerization (ATRP) and were initiated by the PEG_{113} macro-initiator. During the polymerization, about 0.1 mL of the reaction mixture was removed from the flask by syringe, and was analyzed by ^{1}H NMR. The conversion of the *t*BA monomer

was then calculated based on ^{1}H NMR results. The polymerization was stopped when the conversion of the *t*BA monomer exceeded 60 %.

We prepared two batches of block copolymers having different *t*BA units. The composition of the block copolymers was characterized in the PEG-*b*-P*t*BA form. PEG_{113} was a commercial product with a narrow polydispersity and precisely characterized molecular weight. The number of *t*BA units was calculated based on ^{1}H NMR data, in which the integral from PEG was compared with that of *t*BA. The polydispersity of the block copolymer was obtained by GPC results. The data are summarized in Table A-1. The P*t*BA block of the obtained polymer was then converted into PAA following in the presence of TFA. Successful conversion was confirmed by the ^{1}H NMR, as the peak representing P*t*BA at 1.4 ppm disappeared.

Table A-1 Molecular characterization of PEG-*b*-P*t*BA block copolymers

Polymer batches	Number of *t*BA units	Polydispersity (PDI)	Composition of the copolymer
Polymer 1	12	1.27	PEG_{113}-PAA_{12}
Polymer 2	7	1.24	PEG_{113}-PAA_{7}

A-3.2 Preparation of cobalt nanoparticles

In this research, the cobalt particles were synthesized using a thermal decomposition method. The precursor, $Co_2(CO)_8$, was dispersed into DCB at a high concentration (100 mg/mL). This dispersion was injected into a preheated solvent containing dissolved

surfactant. The decomposition of $Co_2(CO)_8$ occurred simultaneously as it was mixed with the preheated solvent to generate the cobalt monomer. The formation of cobalt nanoparticles follows the LeMar mechanism. The nuclei are formed in the presence of surfactant when the concentration of the Co(0) monomer is supersaturated. The surfactant attaches and detaches from the nuclei to allow them to grow.

Dr. Mentanegro conducted a preliminary study of this process.[18] In this study, the decomposition of $Co_2(CO)_8$ was done in the presence of PEG_{113}-*b*-PAA_8. Under these surfactant conditions, the resulting cobalt particles had poorly defined shapes, and had a diameter of 9.1 ± 4.0 nm. The ratio between the diameter (d) and the spread (σ), or σ/d, was 44%, indicating a broad size distribution of the nanoparticles. However, if the decomposition of $Co_2(CO)_8$ was done in the presence of PEG_{113}-*b*-PAA_8 and TOPO, the obtained cobalt particles were spherical, with a σ/d value of less than 20%, indicating a narrower size distribution. A possible explanation of this result is that the equilibrium of the attachment and detachment of the surfactant onto and from the nuclei governs the growth of the nanoparticles. Polydentate polymeric surfactants bind much more strongly onto the surfaces of cobalt particles than monodentate surfactants, such as TOPO. Thus, the attachment-detachment equilibrium was not well established with the presence of only the PEG_{113}-*b*-PAA_8 surfactant. During the growth of the nanoparticles, the addition of TOPO is required. Puntes *et al.* and Shukla *et al.* reported that the presence of TOPO during the preparation of cobalt nanoparticles induced monodipersity of their products.[19,20] Pyun *et al.* prepared cobalt particles using end-functionalized polystyrene without any small-molecule surfactants present.[17] However, this polystyrene surfactant

had only one binding site, at its functionalized end, which allowed the attachment-detachment equilibrium to be established. The prepared cobalt particles were listed in Table A-2.

Table A-2. Summary of the cobalt particles.

Batch	Polymer	[COOH] / [TOPO]	1st Injection of $Co_2(CO)_8$			2nd injection	Size and size distribution (nm)
			[COOH]	[Co]	[Co]/ [COOH]	[Co]/ [COOH]	
1	PEG_{113}-*b*-PAA_{12}	3.0	0.0099 M	0.03 M	3.0	—	9.0 ± 1.7 (19 %)
2	PEG_{113}-*b*-PAA_{12}	3.0	0.0099 M	0.08 M	8.0	—	12.2 ± 2.0 (17 %)
3	PEG_{113}-*b*-PAA_7	3.0	0.0099 M	0.03 M	3.2	—	6.5 ± 1.1 (16 %)
4	PEG_{113}-*b*-PAA_7	3.0	0.0099 M	0.08 M	8.0	—	10.8 ± 1.8 (16 %)
5	PEG_{113}-*b*-PAA_7	3.5	0.0099 M	0.08 M	8.0	—	10.2 ± 1.5 (15 %)
8	PEG_{113}-*b*-PAA_7	3.4	0.0099 M	0.15 M	15	—	17.0 ± 2,3 (13 %)
9	PEG_{113}-*b*-PAA_7	3.4	0.0079 M	0.23 M	30	—	17.6 ± 2.5 (14 %)
11	PEG_{113}-*b*-PAA_7	3.4	0.011 M	0.097 M	8.9	18	13.4 ± 2.3 (17 %)
12*	PEG_{113}-*b*-PAA_7	3.4	0.0099 M	0.15 M	15	30	17.4 ± 2.9 (16 %)
13	PEG_{113}-*b*-PAA_7	3.4	0.0099 M	0.15 M	15	30	21.6 ± 3.9 (18 %)

* This is the obtained by stopping reaction 3 min after the second injection of precursor.

A-4 Factors affecting the size and size distribution of the cobalt particles

In the literature review section, we discussed that the formation of nanoparticles consists of two stages, the nucleation and growth stages. Without consideration of the effect of surfactant, LaMer showed that the rate of nuclei formation per unit volume is:[52, 55 21,22]

$$\rho(t) = Dc^2 \frac{32\pi^2 a^3 \gamma}{3kT\ln(c/c_0)} \exp\left(-\frac{256\pi^3 a^6 \gamma^3}{27(kT)^3[\ln(c/c_0)]^2}\right) \qquad \text{(A-1)}$$

where c is the concentration of monomers of the nanoparticle present in the system at time t, c_0 is the solubility of a bulk nanoparticle, a is the effective radius of a monomer unit in a nanoparticle, D is the diffusion coefficient of the monomer, γ is the effective interfacial tension between a nuclei or nanoparticle and its surrounding medium, and kT is the thermal energy. At a given temperature T, $\rho(t)$ is determined strongly by c and γ.

The growth of inorganic crystals has been traditionally assumed to be diffusion controlled. The diffusion-controlled growth rate for a nanoparticle of radius r is:[423]

$$\frac{dr}{dt} = \frac{K_D}{r}\left(\frac{1}{r^*} - \frac{1}{r}\right) \qquad \text{(A-2)}$$

and K_D is :

$$K_D = \frac{2\gamma D a^6 c_0}{kT} \qquad \text{(A-3)}$$

Equation (A-2) suggests that $dr/dt > 0$ only if $r > r^*$ or the particles grow with time only if their radius is larger than r^*. Therefore, r^* is called the critical radius, which increases as the monomer concentration decreases.

A-4.1 Effect of number of dentate

Polymers 1 and 2 were used to prepare cobalt particles under similar conditions. The concentration of the Co monomer was adjusted to 0.15 M, and the concentrations of the carboxylic acid groups and TOPO were also kept at this concentration. By comparing Batches 1 and 3 (Figure A-1 parts (a) and (c)), particles prepared using Polymer 1 had larger average diameters than the particles prepared using Polymer 2. Similarly, the nanoparticles of Batch 2 has greater diameters than those of Batch 4 (Figure A-1 parts (b) and (d)). From Equation (A-1), the number of nuclei is related to the interfacial tension when the concentration of the monomer is constant. In Batch 1, if the concentration of the COOH group is same as in Batch 3, concentration of Polymer 1 in Batch 1 should be much less than the concentration of Polymer 2 in Batch 3. As the surfactant content decreased, the extent of binding decreased between PEG-*b*-PAA and the monomers and nanocrystals of Co. The effective interfacial tension (γ) between Co and the solvent should increase. An examination of the exponent of Equation (A-1) suggests that an increase of γ leads to a decrease of $\rho(t)$. As the concentration of the monomer is constant, the diameter of the nanoparticle would increase.

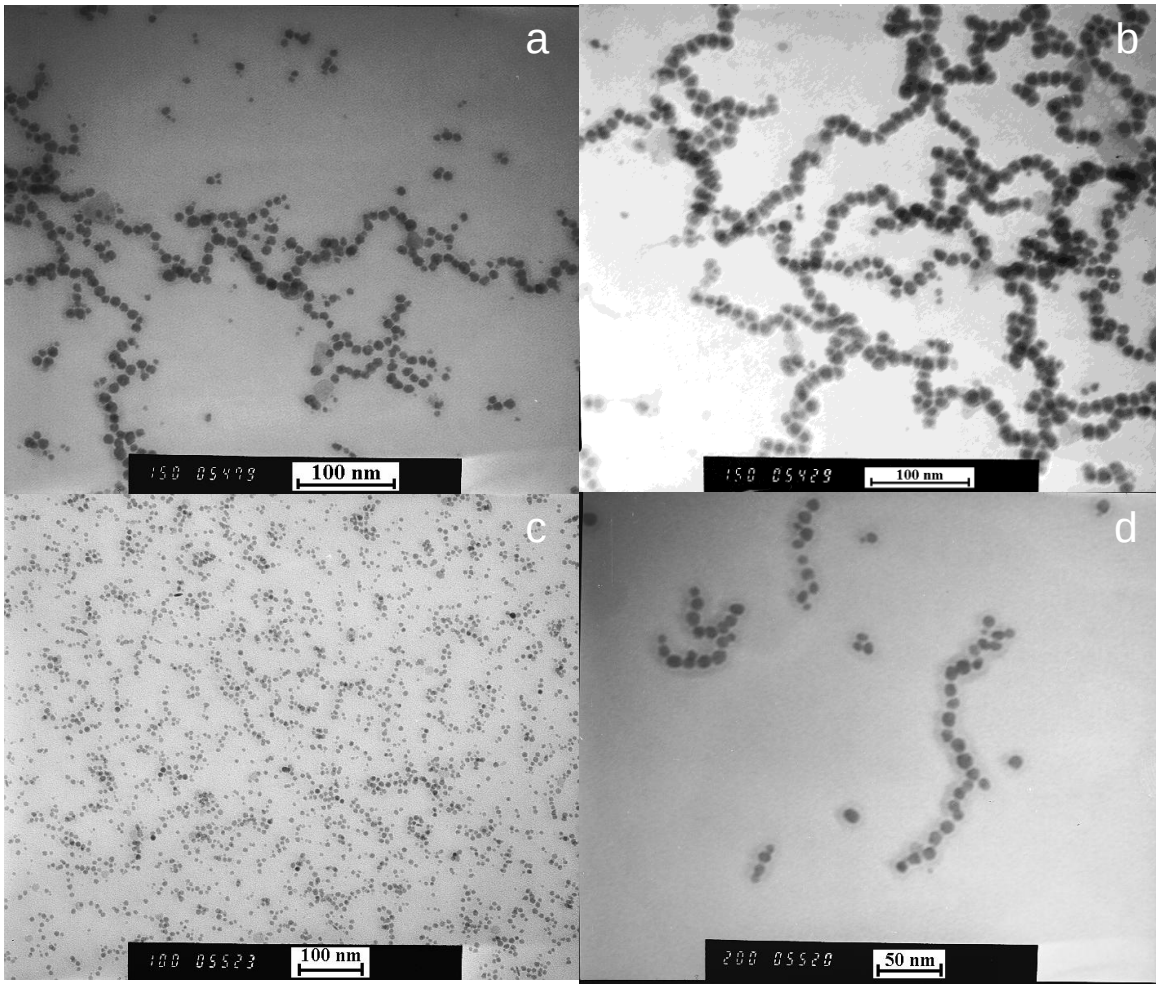

Figure A-1. TEM images of cobalt particles prepared in the presence of Polymers 1 and 2: (a) Batch 1, prepared with Polymer 1 as the surfactant, [Co]/[COOH] is 3.0, (b) Batch 2, prepared with Polymer 1 as the surfactant, [Co]/[COOH] is 8.0, (c) Batch 3, prepared with Polymer 2 as the surfactant, [Co]/[COOH] is 3.0, and (d) Batch 4, prepared with Polymer 1 as the surfactant, [Co]/[COOH] is 8.0.

The size distribution of the particles was also under consideration. By comparing Batch 1 with Batch 3, and Batch 2 with Batch 4, it became apparent that the particles prepared with shorter PAA chains had narrower size distributions. A possible explanation for this trend relies on the fact that during the growth stage of the nanoparticles, the polymeric surfactants bind to the nanoparticles by anchoring their PAA segments onto the surfaces

of the particles. Due to the steric effect and the orientation of PAA chains, it was not necessary for all of the carboxylic acid groups to interact with the cobalt. For example, Polymer 2 could anchor onto the surface of a cobalt nanoparticle using between 1 and 7 of its carboxylic groups, which means that there would be 7 different ways that the polymer could potentially bind to the nanoparticle. The difference in the stabilization effects between all of these possibilities would probably result in different attachment-detachment equilibriums of the surfactants and different coverage of the nanoparticles by polymer chains. Thus, a broadening effect of size distribution may be generated. Since Polymer 1 has more PAA groups, and thus more potential binding modes, the broadening effect of Polymer 1 should be somewhat greater than that of Polymer 2.

A-4.2 Effect of the mole ratio between Co monomer and surfactant

At relatively low monomer concentrations, the average size of the cobalt particles could be tuned by varying the ratio between monomer and the carboxylic acid groups (when the COOH/TOPO ratio was kept constant). In preparing Batches 1 and 2, the amount of surfactant present was held constant. The ratio between the concentration of the monomer and the concentration of the carboxylic acid groups was changed from 3.0 : 1.0 to 8.0 : 1.0. The average sizes of the particles increased from 9.0 to 12.2 nm. Similarly in Batches 3 and 4, the diameters of the nanoparticles increased from 6.5 to 10.8 nm when [Co]/[COOH] increased from 3.0 to 8.0, respectively. However, at higher concentrations (Batches 8 and 9, Fig. A-3), increasing the ratio between the monomer and the COOH group did not result in significant increases of average sizes of the particles.

Applying Equation (A-1), a possible explanation is proposed. With increasing [Co], the value of [Co]/[COOH] decreases. This leads to an increase of interfacial tension γ caused by the decrease of surfactant content. If the concentration of the monomer is very low, the γ increase effect may dominate over the effect of increasing concentration *c*. Therefore, the number of nuclei decreased, resulting in an increase of the size of the nanoparticles. If the concentration of the monomer is very high, the effect of the monomer concentration should have a higher impact on $\rho(t)$, which would somehow cancel the impact of the increase of γ. Therefore, when the nanoparticles are prepared at high monomer concentrations, the sizes of the nanoparticles do not increase significantly.

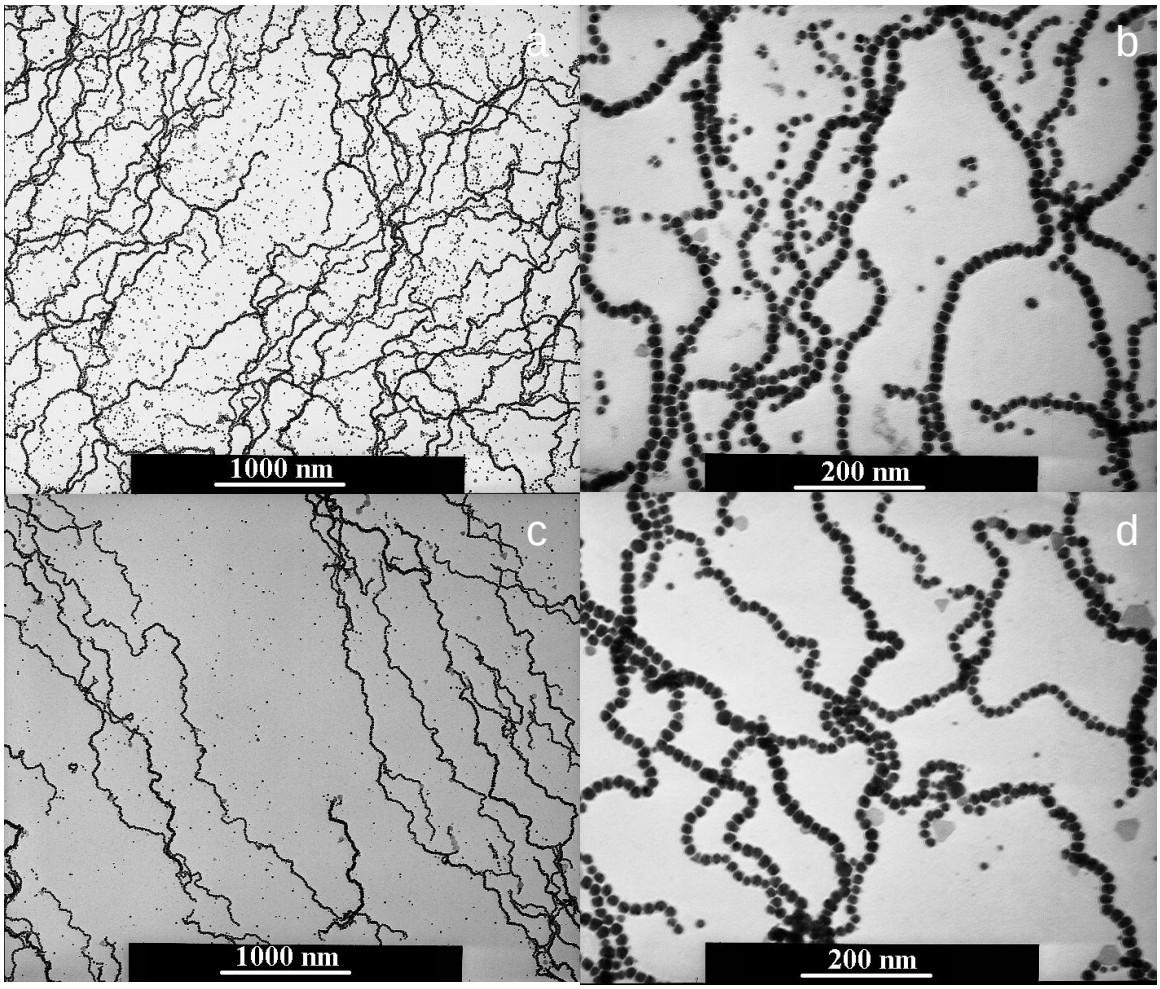

Figure A-2. TEM images of the cobalt particles prepared at high monomer concentrations using Polymer 2 as surfactant: (a) and (b) Batch 8, [Co]/[COOH] is 15 (c) and (d) Batch 9, [Co]/[COOH] is 30.

A-4.3 Double injection

As mentioned above, at low concentrations, the cobalt particle diameter could be adjusted by varying the ratio between the monomer and surfactant. Under this regime, cobalt nanoparticles with narrow size distributions and with average diameters greater than 17 nm could not be prepared. Meanwhile, under the high concentration regime, the average

sizes of the cobalt particles could reach as high as approximately 18 nm. However, the sizes of the particles could not be readily tuned by simply increasing the monomer/surfactant ratio. In order to overcome this problem and prepare cobalt nanoparticles with narrow size distributions, and average diameters greater than 18 nm, the double injection method was used.

The double injection method was first proposed by Alivisatos and coworkers.[23] As predicted by Howard Reiss, at any given monomer concentration, a specific diameter (peak diameter) corresponding to a maximum growth rate exists.[24] By analyzing Equation (A-3), dr/dt gives a maximum value when $r = 2r^*$. In a regime where the particle diameter is greater than the peak diameter, smaller particles grow faster than larger particles. This is called a size-focusing regime. Meanwhile, under a regime where the particle diameter is smaller than the peak diameter, smaller particles grow more slowly than larger particles. This is called a size-defocusing regime. The value of the peak diameter is related to the concentration of monomer. At a high monomer concentration, the peak diameter becomes smaller. Thus, more particles are located in the focusing regime. This will lead to narrower size distributions. As shown in Table 2, particles prepared with high monomer concentrations (Batches 8 and 9) have narrower size distributions than the particles prepared at low monomer concentration. If one imagines a system in which the growth of cobalt particles is almost in equilibrium, the sudden addition of more of the monomer perturbs the system as the concentration of the monomer increases. As a result of this increase in the monomer concentration, the peak diameter shifts to a smaller value. Since the size distribution of the particles remains

unchanged at the moment of secondary injection, this sudden injection of monomer will expand the focusing regime. Therefore, more particles will be located within the focusing regime, so that the sizes of the particles will increase and the size distribution of the particles will become narrower.

In this thesis, we attempted to use this method to increase the diameters of the cobalt particles in a more controlled manner. We first injected a portion of the precursor into a preheated solvent. After 5 min of incubation, a second batch of the precursor was added. In the high monomer concentration regime, Batch 8 had a diameter of 17.0 nm, and represented the Batch 8 represented the stage between the first and second injection, which was represented by Batch 13. In fact, 3 min after the second injection (Figure A-3 (a)), the average diameter of the particle was 17.4 nm. As mentioned by Puntes *et al.*, the growth process of cobalt particles could be as long as 30 min under certain conditions.[17] However, 10 min after the second injection (in which same amount of precursor as the first injection was added), the average size of the cobalt particles increased to 21.6 nm (Figure A-3 (b)). Comparing Batches 8 and 13, the average sizes of the particles increased by a factor of 1.27 and the average volume of the particles increased by a factor of 2.05. Similarly, from Batches 5 and 11 (Figure 4 (d) and (c)), the [Co]/[COOH] ratio was increased from 8.0 to 18, respectively (by a factor of 2.25). The diameters of the nanoparticles of Batch 5 and 11 were 10.2 and 13.4 nm, respectively, and thus the ratio between these two batches of samples is 1.31:1 (Batch 5:Batch 11). The volume ratio between them is 1.31^3 or 2.26. Thus, at relatively high monomer concentrations, the sizes of the cobalt particles could be precisely tuned using this double injection recipe.

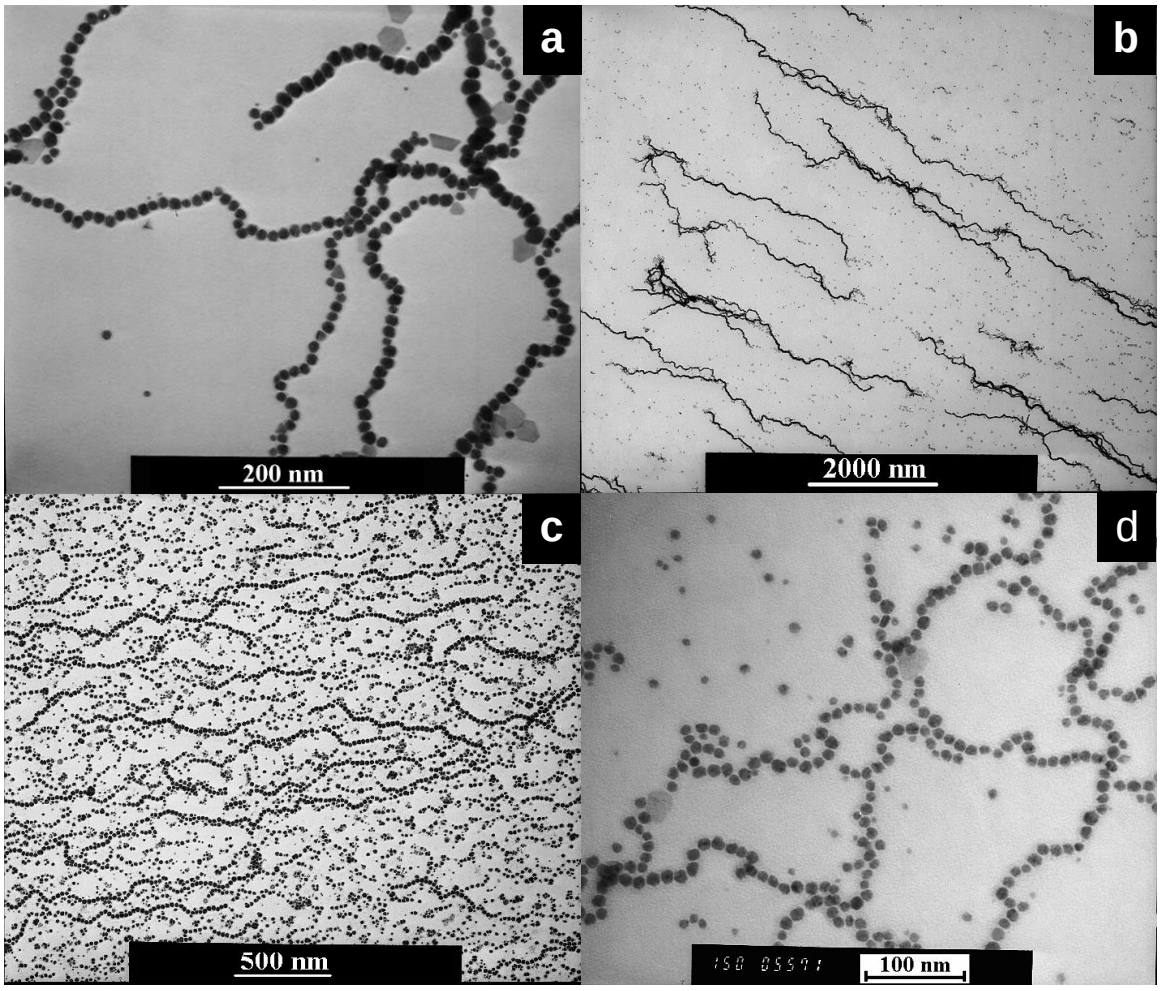

Figure A-3. TEM images of the cobalt particles prepared using the double injection method using Polymer 2 as the surfactant: (a) Batch 12, 3 min after the second injection, [Co]/[COOH] is 30, (b) Batch 13, 10 min after the second injection, [Co]/[COOH] is 30, (c) Batch 11, 10 min after the second injection, [Co]/[COOH] is 18, and (d) Batch 5, single injection, [Co]/[COOH] is 8.0.

A possible explanation for this precise size control is that before and after the second injection, the number of nuclei is almost constant. This may be true because the Ostwald ripening will be very strong if the existing nanoparticles have a sufficiently large size. Therefore, the newly generated nuclei would shrink, and were eventually eliminated in

the end. The second batch of the monomer was completely absorbed by the existing nano particles that were generated after the first injection.

A-5 Dipolar chains

The cobalt particles could form dipolar chains when the dipolar constant was greater than 2.[25] We measured the thickness of the PEG layer from the TEM images shown in Figure A-2 parts (b) and (d). However, since the PEG layer could not be stained, this value may not be very accurate. The measurements from the TEM images suggested that the PEG layer of the cobalt nanoparticles had an average thickness of 4.2 ± 0.5 nm. If, these values were correct, in order to have a dipolar constant greater than 2, the average radii of the cobalt particles should be greater than 4.5 nm. In other words, the critical diameter of the cobalt particle should be 9.0 nm. Based on this calculation, all of the samples, except Batch 3 (Figure 1 (c)) can form dipolar structures. The dipolar structures of those samples were confirmed with the TEM images.

A-6 Conclusions

Cobalt nanoparticles were prepared in the presence of a PEG-*b*-PAA block copolymer. Factors influencing the sizes and size distributions of these cobalt nanoparticles were studied. At low monomer concentration regimes, the average size of the cobalt particles could be adjusted by varying the molar ratio between the monomer and the polymeric

surfactant. At high monomer concentration regimes, cobalt nanoparticles with narrow size distributions were obtained. In order to control the size of the cobalt particles at high monomer concentration, a double injection method was applied. The obtained cobalt particles could form dipolar structures when their diameter was above a critical value. This research provided a good understanding of the preparation of cobalt particles with polydentate polymeric surfactants. A similar strategy was used in the preparation of permanently locked cobalt wires, which is discussed in Chapter 4.

References

1. Pyun, J. *Polymer Reviews* **2007**, *47*, 231.

2. Kaplan, L. A.; Pesce, A. J., *Clinical Chemistry - Theory, Analysis, and Correlation*. CV Mosby Co.: St. Louise, 1989.

3. Dobson, J. *Nanomedicine (London, United Kingdom)* **2006**, *1*, 31.

4. Thurn-Albrecht, T.; Schotter, J.; Kastle, C. A.; Emley, N.; Shibauchi, T.; Krusin-Elbaum, L.; Guarini, K.; Black, C. T.; Tuominen, M. T.; Russell, T. P. *Science* **2000**, *290*, 2126.

5. Reiss, G.; Huetten, A. *Nature Mater.* **2005**, *4*, 725.

6. Puntes, V. F.; Krishnan, K. M.; Alivisatos, A. P. *Science*, **2001**, *291*, 2115.

7. Xia, Y.; Xiong, Y.; Lim, B.; Skrabalak, S. E. *Angew. Chem. Int. Ed.* **2008**, *47*, 2.

8. Balazs, A. C.; Emrick, T.; Russell, T. P. *Science* **2006**, *314*, 1107.

9. Wang, X.; Dykstra, T. E.; Salvador, M. R.; Manners, I.; Scholes, G. D.; Winnik, M. A. *J. Am. Chem. Soc.* **2004**, *126*, 7784.

10. Wang, Y.; Teng, X.; Wang, J. S.; Yang, H. *Nano Lett.* **2003**, *3*, 789.

11. Matsuno, R.; Yamamoto, K.; Otsuka, H.; Takahara, A. *Chem. Mater.* **2003**, *15*, 3.

12. Sun, S. H.; Murray, C. B. *J. Appl. Phys.* **1999**, *85*, 4325.

13. Zhou, Z.; Liu, G.; Han, D.; *ACS Nano* **2009**, *3*, 165.

14. Liu. G.; Yan, X.; Lu, Z.; Curda, S. A.; Lal, J. *Chem. Mater.* **2005**, *17*, 4985.

15. Thomas, J. R. *J. Appl. Phys.* **1966**, *37*, 2914.

16. Korth, B. D.; Keng, P.; Shim, I.; Bowles, S. E.; Tang, C.; Kowalewski, T.; Nebesny, K. W.; Pyun, J. *J. Am. Chem. Soc.* **2006**, *128*, 6562.

17. Keng, P. Y.; Shim, I.; Korth, B. D.; Douglas, J. F.; Pyun, J. *ACS Nano* **2007**, *1*, 279.

18. Martinez-Castro, M.; Zhou, Z.; Liu, G. *Polymer*, accepted.

19. Puntes, V. F.; Krishnan, K. M.; Alivisatos, A. P. *Appl. Phys. Lett.* **2001**, *78*, 2187.

20. Shukla, N.; Svedberg, E. B.; Ell, J.; Roy, A. J. *Mater. Lett.* **2006**, *60*, 1950.

21. LaMer, V. K. *Industrial And Engineering Chemistry* **1952**, *44*, 1270.

22. Park, J.; Privman, V.; Matijevic, E. *J. Phys. Chem. B* **2001**, *105*, 11630.

23. Peng, X.; Wickham, J.; Alivisatos, A. P. *J. Am. Chem. Soc.* **1998**, *120*, 5343.

24. Riess, H. *J. Chem. Phys.* **1951**, *19*, 482.

25. Benkoski, J. J.; Jones, R. L.; Douglas, J. F.; Karim, A. *Langmuir* **2007**, *23*, 3530.